UNIVERSITÀ DEGLI STUDI DI CATANIA
Dottorato di Ricerca in Fisica- XXV ciclo

Giuseppe Castro

STUDY OF INNOVATIVE PLASMA HEATING METHODS AND APPLICATIONS TO HIGH CURRENT ION SOURCES

PhD Thesis

Tutors:
Prof. Francesca Rizzo
Dott. Santo Gammino
Dott. David Mascali

PhD coordinator:
Prof. Francesco Riggi

ANNO ACCADEMICO 2011/2012

Contents

Introduction

The use of plasmas in various areas of scientific research has been growing in recent years. Since 1970, moreover, their contribution has been crucial in the field of accelerator physics, and consequently contributed to the impulse that this gave to nuclear and Particle Physics in the last thirty years. The Electron Cyclotron Resonance Ion Sources and the Microwave Discharge Ion Sources are currently the best devices worldwide able to feed effectively high energy accelerators such as Linacs, Cyclotrons, Synchrotrons or Colliders. The plasma is excited by microwaves typically in the range 2.45-28 GHz; microwaves are coupled to a cylindrical chamber working as resonant cavity, where the plasma is produced, by a suitable system of waveguides, and are absorbed therein during the interaction with gases or vapors fluxedd at low pressure (10^{-6} - 10^{-3} mbar). In presence of the magnetostatic field, the electromagnetic wave absorption is particularly efficient at the so-called "Electron Cyclotron Resonance". From the high density and high temperature plasma ($n_e \sim 10^{10} - 10^{12} cm^{-3}, T_e \sim 0.1 - 100 keV$) part of the ion content is extracted, which finally constitutes the ion beam to be sent to the accelerators. Most of the parameters of the extracted beam, such as the intensity, the emittance and the shape in the real space depend in a decisive way on the characteristics of the plasma which from which the beam is extracted. The further development of ECR-type ion sources is however intrinsically limited by physical properties of the plasmas. The electromagnetic energy can not be transferred to the plasma electrons over a certain density threshold, named cutoff density, (in other words, the layer in which the ECR resonance occurs becomes inaccessible). Normally, in plasmas sustained by microwaves, the density increases with RF power but it stabilizes below a limit value situated just slightly below the critical density. In the field of controlled nuclear fusion and magnetic confinement, this topic has a crucial importance since it limits the satisfaction of the Lawson criterion. But also in the ion sources field this topic is of fundamental importance,

because the extracted currents are directly proportional to the plasma density: the presence of the cutoff limitation, therefore, limits the performance of the sources.
The studies we performed during the PhD course, carried out on a MDIS, have shown that it is possible to excite waves in magnetized plasmas having an electrostatic nature (Electrostatic Bernstein Waves) which are not reflected at the density cutoff. An electrostatic wave is a rarefaction-compression wave whose electric field is parallel to the wave propagation direction. In particular, Electron Bernstein Waves (EBW) can be strongly absorbed by the plasma at cyclotron harmonics. Due to their electrostatic nature, EBW must be generated within the plasma from electromagnetic waves, through a conversion mechanism which takes from an electromagnetic wave to electrostatic oscillations (conversion mechanisms are typically called XB or OXB mechanisms). We operated in different experimental conditions: by varying the operating frequency (by means of a TWT), it is possible to operate exclusively in EBW heating mode, to have the simultaneous presence of ECR heating and EBW heating or, opportunely moving the permanent magnets, totally inhibited the generation of electrostatic waves. EBW generation and absorption in a plasma is highlighted by the three experimental evidences: 1) exceeding of the electromagnetic density cutoff 2) generation of high-energy electrons, 3) detection of non-linear decay of the spectrum of the incident electromagnetic radiation in a plurality of ancillary frequencies (the "broadening" of the incident electromagnetic radiation is often referred as "parametric decay"). All these three signatures have been measured above a critical threshold of the RF power (further sign of non-linear interaction). The study of the high energy electrons population has been carried out by means of the bremsstrahlung radiation emitted by the electrons when colliding with the plasma ions or with the chamber walls. The detection of X radiation at energies domains of tens of keV is absolutely relevant by a scientific point of view, and it represents one of the clue of this thesis work. In facts, generally MDIS plasmas are not capable to emit in the X-ray domain (the maximum energy of the electrons is typically 100-200 eV in ECR heating regime). When satisfying conditions for modal conversion, the formation of a plasma "vortex" was moreover observed. Drifting electrons are characterized by an electron speed of the order of $1 \cdot 10^6 m/s$ due to absorption of electrostatic waves at cyclotron harmonics (measurements say). At the moment we are able to demonstrate only that an electronic azimuthal flow exists, but some experimental data and the ongoing studies would suggest that an ion motion is excited too.

The arguments up to now introduced were organized in five different chapters: In the first chapter we introduce the general features of plasmas, as the collisional effects, the diffusion and the different theoretical approaches to model magnetized plasmas in linear machines. The second chapter is devoted to problems related to wave propagation in magnetized plasmas. To a first part dedicated essentially to the propagation of electromagnetic waves, the study of the generation and absorption of the Bernstein waves in plasmas will follow. In the third chapter an overview of the different ion sources is given, together with the main peculiarities of the microwave discharge and ECR ion sources. Furthermore the basic parameters that characterize the particle beams are defined. The fourth chapter introduces the experimental apparatus used for measurements and provides an overview of the analysis methods used to derive the plasma parameters. Chapter 5 shows the analysis of the experimental data in terms of profiles density, X spectroscopy and spectral analysis of electromagnetic radiation interacting with plasmas. The space resolved analysis of the plasma resistivity curves provided information on the density profiles and electron temperature, highlighting a substantial increase in the regions of magnetic field favorable to the occurrence of the modal conversion. Thanks to the systematic study of the X-ray spectra it was moreover possible to identify the threshold of the conversion process ($\sim$ 80 W for the specific set-up), characteristic of all the non-linear processes that occur beyond certain values of RF power. Finally, the conclusion chapter of the thesis is aimed to identify the possible applications of the know-how developed in this thesis; in particular the gained know-how has potential applications in the design and construction of the injector of the European Spallation Source facility and for the project DAEδALUS (Decay At rest Experiment for δ CP studies At the Laboratory for Underground Science). The obtained results are of particular importance also in a far future perspective, since conceptually new ion sources could be realized starting from the new mechanism of plasma heating hereby investigated.

Chapter 1

Fundamental of plasma physics

The plasma physics is one of the fundamental branch of modern science. It finds a great number of applications in several fields of nature, from astrophysics to nuclear physics, to the applications to the nuclear fusion and to the industrial applications. Plasma constitutes over the 98% of the matter of the universe. Thus, the study of plasma physics can provide a fundamental step forward in the comprehension of the nature. In the next pages only the aspects directly linked to the activities carried out during the PhD course will be treated with some details. A more detailed and generalized treatment can be found in the references [1] and [2].

1.1 Plasma parameters

The fundamental parameters characterizing the plasmas generated in an Electron Cyclotron Resonance Ion Source are the electron density n_e (measured in cm^{-3} or m^{-3}), the temperature T of each species (usually measured in eV or keV), the ion confinement time t_c and the external magnetic field B.
All the main characteristics of the plasma and of the extracted beam depend on these four parameters. Several ancillary parameters can be derived from these and they will be introduced little by little in the following. The Debye length represents the scalelength over which mobile charge carriers (e.g. electrons) screen out electric fields in ionized gas:

$$\lambda_d = \sqrt{\frac{\epsilon_0 T_e}{n_e e^2}} \tag{1.1.1}$$

A ionized gas can be defined a plasma only if its characteristic dimension λ is much larger than Debye length, i.e. $\lambda \gg \lambda_d$. As a consequence of the screening of the electric fields, for scalelengths larger than debye length, the plasma is quasi-neutral, i.e. the ion density n_i is ever equal to the electron density n_i.

1.2 Collision in plasmas

Plasma collisionality plays a crucial role in several processes. It regulates the confinement times in magnetically confined plasmas, it thermalizes the electrons in low temperature discharges and it determines the ionization rates in a plasma used as source of ions. In order to discuss about the main collision phenomena occurring in ECR plasmas, it is convenient to introduce two physical quantities: the *mean free path* λ_{mfp} and the *collision frequency* ν. These parameters depends on the cross section of the process σ [2]:

$$\lambda_{mfp} = \frac{1}{n\sigma} \tag{1.2.1}$$

$$\nu = n\overline{\sigma v} \tag{1.2.2}$$

where $\overline{\sigma v}$ is the product between the cross section and the particle velocity averaged over the velocity distribution function (generally a Maxwellian one). The collision time τ is the reciprocal of the collision frequency $\tau = 1/\nu$. The collisions occurring in plasma can be divided in two groups according to the number of colliding particles: **multiple collisions** are characteristics of plasmas, because they occur thanks to the long range Coulomb interaction. The **binary collisions** are similar to the collisions in gaseous systems; however, in this case, non-elastic and ionizing collisions occur because of the high energy content of the plasma particles, especially of electrons.

1.2.1 Spitzer collisions

The Spitzer collisions represent the multiple interactions of a single particle with many other particles, and the net effect is to give a large-angle scattering. These cumulative small-angle scatterings, finally resulting in a 90° deflection, play a role only in highly ionized and low pressure plasmas,

where internal electromagnetic interactions are predominant. These collisions must be extended over the whole distance where the Coulomb forces are effective, i.e. the Debye shielding length. It can be demonstrated that the effective cross-section for 90° deflection by means of multiple collisions is [2]:

$$\sigma = \left(\frac{z_1 z_2 e^2}{\epsilon_0 m v^2}\right)^2 \ln \frac{\lambda_d}{b_{min}} \tag{1.2.3}$$

where z_1 and z_2 are the charges of the two particles, e is the electron charge, m is the mass of the colliding particle and the term $\ln \dfrac{\lambda_d}{b_{min}} = \ln \Lambda$ is the so called Coulomb logarithm. This equation is similar to the cross-section for single Coulomb scattering (Rutherford formula), but the multiple scattering probability exceeds single scattering by the factor $8 \ln \Lambda$, so the 90° scattering due to a single collision is much less probable than multiple deflections. Starting from equation (1.2.3) it is possible to calculate the collision frequencies for the different particle constituting the plasma:

$$\nu_{90^\circ}^{ee} = 5 \cdot 10^{-6} n_e \frac{\ln \Lambda}{T_e^{\frac{3}{2}}} \tag{1.2.4}$$

$$\nu_{90^\circ}^{ei} \cong 5 \cdot 10^{-6} z n_e \frac{\ln \Lambda}{T_e^{\frac{3}{2}}} \tag{1.2.5}$$

$$\nu_{90^\circ}^{ii} \cong z^4 \sqrt{\frac{m_e}{m_i} \left(\frac{t_e}{t_i}\right)^3} \nu_{90^\circ}^{ee} \tag{1.2.6}$$

where n_e is in cm^{-3} and T_e in eV. Each frequency is usually called characteristic Spitzer collision frequency[1].
The first consequence of the previous equations is that $\nu_{90^\circ}^{ii} \gg \nu_{90^\circ}^{ee} \sim \nu_{90^\circ}^{ei}$, i.e. the ions are much more collisional than electrons. In a MDIS plasma characterized by a density of $1 \cdot 10^{11} cm^{-3}$ and $T_e = 10$ eV, ν_{ee} lies between 10^5 and $10^6 Hz$. Because the cyclotron frequency usually ranges between 2.5 and 20 GHz, Spitzer collisions does not prevent the electron gyromotion around the force lines of the magnetic field. For this reason, ECR plasmas can be considered **collisionless or quasi-collisionless**, and this remains true in most cases even when inelastic and elastic collisions are added to the Spitzer collisions. To investigate the plasma thermalization via collisions

[1]The correct term should be 90° scattering. We talk about the collision frequency for sake of simplicity.

the energy transfer frequency must be analyzed. The energy transfer depends on the masses of the colliding particles; particles of the same species (for example e-e or i-i) transfer about an half of the initial one, whereas in $e-i$ or $i-e$ collisions the transfer of energy equal to $\frac{m_e}{m_i}$. Applying these considerations to the equations (1.2.4-1.2.6) we can easily notice that $\tau_m^{ei} = \tau_m^{ie} \sim \frac{m_e}{m_i}\tau_{90^\circ}^{ei}$, $\tau_m^{ee} \sim \tau_{90^\circ}^{ee}$ and $\tau_m^{ii} \sim \tau_{90^\circ}^{ii}$ being τ_m as the characteristic time for the energy transfer. Hence, the thermalization via collisions is much easier among particles of the same species than among electrons and ions. In addition, as the ion lifetime in ECRIS is shorter than the time required for ion heating through collisions, the ions remain cold, whereas the electrons increase their energy because of the interaction with the external electromagnetic field. This result is of primary importance for ECRIS, as one of the most important quality parameters, the emittance, increases with the ion temperature. Thermalization of electrons can be explained by means of the collisions only for low electron energy (few eV). For larger energies τ_m^{ee} becomes larger than the plasma lifetime and the thermalization can be explained only taking into account stochastic processes due to the interaction of the electrons with the electromagnetic wave.(see section 2.2).

1.2.2 Binary collisions

The binary collisions in plasmas can be divided into two groups: the electron-neutral collisions (elastic and inelastic), and the ionizing collisions. The former plays an important role especially in case of high pressure plasmas with a low degree of ionization and a low electron temperature[2] [2]. As featured in figure , these collisions provide the thermalization playing the same role of the Spitzer collisions in case of highly ionized and low pressure plasmas. At electron temperatures comparable or higher than the neutral ionizing potential, the ionizing collisions becomes the most important collision. Even if multi-ionizing collisions might occur, the process having the larger cross section is the single ionization[3], also called **step-by-step ionization**. The time needed for the transition from charge state z_1 to charge state z_2 by means of single ionization takes a time, on average, is [2]:

$$\tau_{z_1 z_2} = \frac{1}{n_e \sigma_{z_1 z_2} v} \tag{1.2.7}$$

[2] $P \sim 10^{-3} - 10^{-4} mbar, T_e \leq 15eV$.

[3] The cross section to expel two electrons is one order of magnitude lower than single ionization, to expel three electrons is two order of magnitude lower, and so on.

Averaging over a Maxwellian distribution, we find:

$$\tau_{z_1 z_2} = \frac{1}{n_e S(T_e)} \tag{1.2.8}$$

where $S(T_e)$ is the reaction rate coefficient which depends only on the temperature of the electron distribution function. Only if the ion confinement time t_c is longer than the time required for the given ionization, transition $z_1 \rightarrow z_1$ takes place. From the condition $t_c > \tau_{z_1 z_2}$ we obtain:

$$n_e \tau_c \geq \frac{1}{S(T_e)} \tag{1.2.9}$$

Equation (1.2.9) can be rewritten by substituting the $S(T_e)$ parameter, obtaining:

$$\zeta n_e \tau_c \geq 5 \cdot 10^5 \left(T_e^{opt}\right)^{\frac{3}{2}} \tag{1.2.10}$$

where $\zeta = \sum_j q_j$ is the number of subshells in the atom outer shells and $T_e^{opt} \sim 5W_{thr}$ is the optimal temperature to have ionization, about equal to five time the ionization threshold energy W_{thr}. The product $n_e \tau_c$ is called **quality factor** for ion sources and, together with the electron temperature, it determines the performances of the ion source. This means that it is possible to improve the performances of an existing source by opportunely increasing these three fundamental parameters. In figure 1.2.1 the function $n_e \tau_c = f(t_e^{opt})$ together with the main ions obtainable in such conditions. The increase of the quality factor and of electron temperature through the development of new plasma heating methodic represents the main frontier of the research and one of the main goals of the PhD activity.

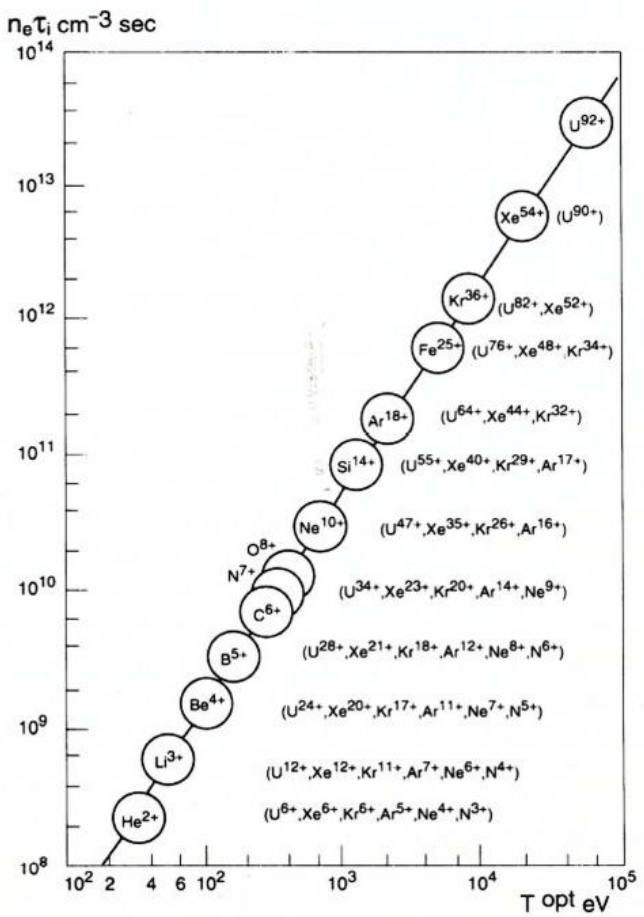

Figure 1.2.1: Golovanivsky's diagram shows the criteria for the production of highly charged ions. The ions enclosed by circles are completely stripped; some combinations of electron temperature, electron density and ion confinement time allow to produce completely stripped ions; inside brackets uncompletely stripped ions are shown: they can be produced with the corresponding plasma parameter of ions enclosed in circles [2]

.

1.2.3 Cold, warm and hot electrons in plasmas

Equations (1.2.4-1.2.6) show the strong dependance of the collision frequency on the electron temperature. As the electron temperature increases, the Spitzer collision probability decreases significantly. A complete thermalization of the electrons is therefore impossible, and three different electron populations, usually named *cold, warm and hot electrons*, are present at any time within the plasma. The characteristics range of energy of each population depends on the type of ion source used. For example in ECRIS the cold population is characterized by temperatures in the range of 1-100 eV, the warm in the range of 100 eV-100 keV, and the hot above 100 keV [2]. On the contrary, in a MDIS the characteristic energy of each population is much lower. As it will be shown in chapter 5, we reveal a cold electrons population having energy of 1-10 eV, warm electrons of several tens or hundreds of eV and a hot population with energies larger than 1 keV. In general the most important population is the warm component. In facts it has an energy large enough to ionize the atoms up to high charge states and, at the same time, a sufficient collision frequency. Only a small part of the cold electrons induce ionization in MDIS, and in ECRIS their energy is too low to ionize inner shells of atoms, even if their collision frequency is the highest. Finally, the hot electrons have a too low cross section for the ionization process, although they have high energies. Further they are detrimental for ECRIS, because they increase the aging of insulators and, in the case of third generation ECRIS, they can heat the helium cryostat, making the operations of the source difficult. The ideal working configuration for obtaining the best performances from an ECRIS is that one which maximizes the warm component while minimizing the hot component. On the contrary, in MDIS sources, the possibility to produce a large amount of hot electrons might be very interesting for different applications and it need to be further investigated. MDIS sources, in facts, are usually able to produce only monocharged ions[4], and the generation of hotter electrons could enable the production of multiply charged ions. In the experimental and conclusions chapters these arguments and the related consequences for ECRIS and MDIS will be further explored.

[4]Their characteristic electron temperature and ion lifetime, is too low to allow the production of 2-3 times charged ions.

1.2.4 Recombination effects

The charge state of plasma ions may decrease because of some electron-ion recombination process. The recombination mechanisms can be divided in three different group: the *radiative recombination*, the *dielectronic recombination* and the *charge exchange recombination*. The process having the larger cross section, and therefore the larger probability to take place, is the charge exchange (C.E.)recombination [84]. Highly charged ions, colliding with lower charged ions or with neutrals, capture some electrons from the electronic cloud of the other particles, decreasing their charge state. Because of its own nature, the recombination rate depends on the background pressure: the higher is the number of the neutral or lowly charged ions, the higher is the probability of charge exchange collisions increase with the number of particle of plasma. For high performance ion sources the charge exchange collision time must be longer than the ionization time for a given charge state, i.e. $\tau_{exch} > \tau_{z_1 z_2}$. This implies that:

$$\frac{n_0}{n_e} \leq 7 \cdot 10^3 \zeta \frac{A}{z} \left(T_e^{opt}\right)^{\frac{3}{2}} \tag{1.2.11}$$

where n_0 is the density of neutrals, and A is the atomic mass number.

1.2.5 Remarks about collisions

The relative ratios of various neutral and ion species in ECR ion sources are determined by the dynamic balance between their generation and loss rates. According to the previous sections, the main processes which take to generation of an ion of charge state i and particle density n_i are the step by step ionization by electron collisions and the C.E recombination with higher ionized ions. The main processes which take to the losses of n_i are the C.E recombination with lower ionized ions or neutrals, the further ionization of the ion by means of electron impact and finally the losses due to diffusion and recombination on the plasma chamber walls[5]. The number of particles per unit volume created or destroyed by means of the different processes can be evaluated by means of the reaction rate coefficient Q, defined as:

$$Q) \int_0^\infty \sigma f(v) v dv \tag{1.2.12}$$

Where σ is the cross section of the process, and $f(v)$ is the electron distribution function. Q represents the number of reaction occurring per unit

[5]Ion extraction is implicitly included in the losses due to diffusion; in facts ions are extracted from the source only after they diffuse out from plasma.

of interacting particles density per second. For practical uses, assuming a Maxwellian distribution, Q can be written as [84]:

$$Q = 6.7 \cdot 10^7 T_e^{-\frac{3}{2}} \int_0^\infty E\sigma e^{\frac{E}{T_e}} dE \tag{1.2.13}$$

Here T_e and E are expressed in eV and σ in cm^2. By definition of Q, it follows that the number of reactions occurring in a cm^3 per second is given by $P = Nn_eQ$, where N and n_e are the reaction particles densities. If the cross sections of the different processes are known, it is hence possible to write a set of N balance equations depending on some free parameters: the electron density n_e, the confinement time τ_i, the electron temperature T_e:

$$\begin{aligned} &\frac{\partial n_i}{\partial t} = \sum_{j=0}^{i-1} n_e n_j Q_{j\to i}^{EI} + \sum_{j=0}^{i-1} \sum_{\nu=i+1}^{z_{max}} n_j n_\nu Q_{j,\nu\to i}^{CE} - \\ &\sum_{j=0}^{i-1} \sum_{\nu=1}^{i-1} n_j n_i Q_{i\to i-\nu}^{CE} - \sum_{j=i+1}^{z_{max}} n_e n_j Q_{i\to j}^{EI} - \frac{n_i}{\tau_i} = 0 \qquad i = 1, 2, ..., z_{max} \end{aligned} \tag{1.2.14}$$

where z_{max} is the highest charge number limited by the electron energy. To close the equation system, it is then necessary to add the quasi-neutrality condition:

$$n_e = \sum_{i=1}^{z_{max}} q_i n_i \tag{1.2.15}$$

where q_i represents the charge state of the ion having particle density n_i. The number of neutral particles per unit volume n_0 can be related to the background pressure as:

$$P = n_0 T_i \tag{1.2.16}$$

T_i being the ion temperature expressed in eV.
This model can be applied either to calculate the charge state distributions in an ECRIS [6] or the mass spectrum and the ionization degree in a MDIS [7]. In figure 1.2.2 the relative abundance of the Argon charge states as a function of $j_e\tau_i$. The main charge state increases for larger ion lifetime.

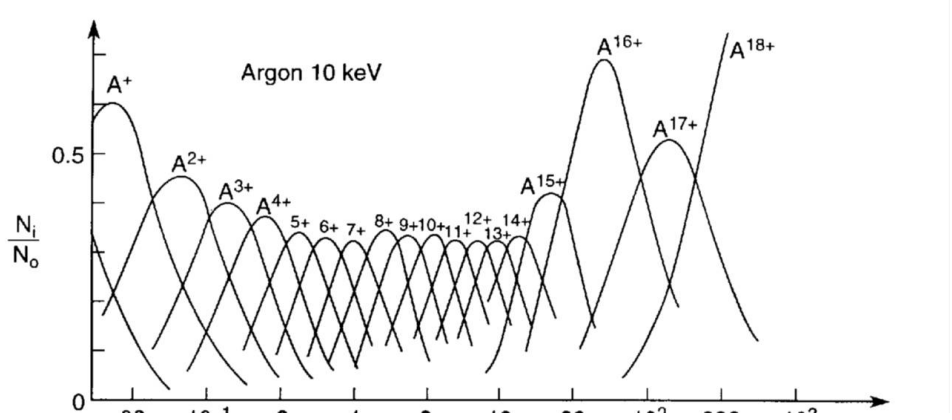

Figure 1.2.2: Relative abundance of the Argon charge states as a function of the confinement time (multiplied for the current density j_e), for an electron temperature $T_e = 10$ keV.

1.3 Theoretical approach to the plasma physics

The plasma is constituted by an enormous number of charged particle. A proton source operating at pressure of about $1 \cdot 10^{-5} mbar$ and one liter volume, for example, contains about 10^{15} ions and electrons. It is practically impossible to solve the motion equation of all the particles or to take into account all the possible collisions between a so large number of particles. In a few words the theoretical approach to the plasma physics needs some approximations.

1.3.1 The single particle approach

The most simple approach to the study of the plasmas is based on the single particle dynamics. Many properties of plasmas, from the confinement to the energy absorption during the-wave particle interaction, and also many aspects of the electromagnetic field propagation can be described in terms of the single particle approach. This approach is based on the solution of the motion equation only for a small number of particles, called test particles ($\approx 10^5$), representative of all the particle constituting the plasma. The simplest equations describing the propagation of electrons and ions in a

plasma are respectively [3]:

$$m_e \frac{d\vec{v}}{dt} = e\vec{E} + F_{coll} + e\vec{v} \times \vec{B}_0 \tag{1.3.1}$$

$$m_i \frac{d\vec{v}}{dt} = F_{coll} \tag{1.3.2}$$

this equation takes into account the effects on the single particle motion, in a non relativistic approximation, of the wave electric field, of the magnetostatic field and of the collisions. In the ion case, the interactions with the electric and magnetic field can be neglected because of their high collisionality. The motion of ionized and neutral atoms is totally similar, in first approximation, to the Brownian motion. As in case of plasmas produced in ECR ion sources the electrons easily reach energies of the order of some hundreds of keV, or also MeV, the relativistic effects must be taken into account, and the complete single particle equation of motion becomes:

$$\frac{d\vec{v}}{dt} = \frac{q}{m_0\gamma}\left[\vec{E} + \vec{v} \times \vec{B}.\frac{\vec{v}\cdot\vec{E}}{c^2}\vec{v}\right] \tag{1.3.3}$$

where $\vec{E}$ is the electric field of the wave, and $\vec{B}$ is the sum of the wave magnetic field and of the magnetostatic field used for the plasma confinement.

1.3.2 The kinetic approach

The most detailed approach to the plasma dynamics is the kinetic theory, which is based on non-equilibrium thermodynamics. An exhaustive approach requires to know all the particle positions and velocities, the fields in which these particles are located and also the reciprocal interaction, or the correlations between pair or groups of particles. This treatment requires the introduction of the distribution function $f(\vec{r}, \vec{v}, t)$. The meaning of the distribution function is that the number of particles per m^3 at position $\vec{r}$ and time t with velocity components between v_x and $v_x + dv_x$, v_y and $v_y + dv_y$, v_z and $v_z + dv_z$ is $f(x, y, z, v_x, v_y, v_z, t)dv_x dv_y dv_z$.
As a consequence $f(\vec{r}, \vec{v}, t)$ is normalized so that:

$$\int_{-\infty}^{+\infty} f(\vec{r}, \vec{v}, t)d\vec{v} = N \tag{1.3.4}$$

where N is the total number of particle constituting the plasma.
In presence of conservative forces the **Liouville theorem** is valid, i.e. *the*

volume occupied by the system in the phase space is constant for different times. This means that, in the phase space, the system evolves like an incompressible fluid. In the particular case of the distribution function, the conservation of the volume in the phase space is equivalent to the conservation of the particles number, being the volume of the plasma constant. The time evolution of the system can be determined by making the total derivative with respect to time of equation (1.3.4):

$$\frac{df(\vec{r},\vec{v},t)}{dt} = \frac{\partial f}{\partial t} + \vec{v}\cdot\vec{\nabla}_r f + \vec{a}\cdot\vec{\nabla}_v f = 0 \tag{1.3.5}$$

The fact that df/dt is a constant in the absence of collisions means that particles follows the contour of constant f in the phase space [1]. In absence of collision and by considering the acceleration as due exclusively to electromagnetic forces, the previous equation can be finally rewritten as:

$$\frac{\partial f}{\partial t} + \vec{v}\cdot\vec{\nabla}_r f + \frac{q}{m}\left(\vec{E}+\vec{v}\times\vec{B}\right)\cdot\vec{\nabla}_v f = 0 \tag{1.3.6}$$

This equation is called *Vlasov equation*. When collisions can not be neglected, the total derivative of the distribution function is not zero, but equal to the time rate of change of f due to the collisions $(\partial f/\partial t)_c$. The equation which takes into account the collisions is named *Boltzmann equation*, and it is easily obtained from (1.3.6) by adding the collisional term:

$$\frac{\partial f}{\partial t} + \vec{v}\cdot\vec{\nabla}_r f + \frac{q}{m}\left(\vec{E}+\vec{v}\times\vec{B}\right)\cdot\vec{\nabla}_v f = \left(\frac{\partial f}{\partial t}\right)_c \tag{1.3.7}$$

Theoretically these equations should be solved for each plasma particle, subjected, point by point, to a well defined field depending on the position of the other particles. Fortunately the problem can be simplified by using the *mean field approximation* and by assuming the particle unrelated. In this approximation, the interaction between a particle and the other ones occurs only by means of the mean field created by all the particle of the plasma. The equation (1.3.6) describes the stationary plasma states, the plasma waves, the instabilities and other short time effects of plasma dynamics in terms of the distribution function $f(\vec{r},\vec{v},t)$.

1.3.3 The Magneto-Hydro-Dynamics (MHD) Approach

Although the plasma looks like a gas, it behaves more like a fluid, and the fluid mechanics is usually a powerful method to describe it. By means of the

MHD the plasma dynamics can be described without a precise knowledge of all the particle positions and velocities, but in terms of macroscopic parameters like temperature, density, pressure, etc. In this sense the fluid approach is simpler than the Vlasov one, and the collisions can be included by considering the momentum exchange between electrons and ions. However all the microstructures due to particle effects cannot be taken into account by means of this approach. Collisionless absorption of electromagnetic waves, and other aspects concerning instabilities due to velocity-distribution inhomogeneities, remain out from the fluidodynamics possibilities. MHD equations can be obtained by making the momenta of equation (1.3.6)[1]. This approach produces a system of n equation in $n+1$ unknowns, in facts each time a higher moment of the Vlasov or Boltzmann equation is calculated in an attempt to obtain a complete set of transport equations, a new macroscopic variable appears. It is then necessary to introduce an acceptable simplifying assumption on the highest momentum closing the equations system.
In collisionless approximation, the first three moments are obtained by multiplying the Vlasov equation by m, mv, and $mv^2/2$, and integrating over all the velocity space. The results are respectively:

1. the equation of conservations of mass (continuity equation);

$$\frac{\partial n}{\partial t} + \vec{\nabla} \cdot (n\vec{u}) \tag{1.3.8}$$

   where $\vec{u}$ is the fluid velocity.

2. the equation of conservations of momentum (fluid equation of motion);

$$mn\left[\frac{\partial u}{\partial t} + (\vec{u} \cdot \vec{\nabla})\vec{u}\right] = qn\left(\vec{E} + \vec{u} \times \vec{B}\right) - \vec{\nabla} \cdot \bar{\bar{P}} \tag{1.3.9}$$

   $\bar{\bar{P}}$ represents the stress tensor, whose components $P_{ij} = mn\overline{v_i v_j}$ specify both the direction of motion and the component of the momentum involved. When the distribution function is an isotropic Maxellian, $\bar{\bar{P}}$ can be written as:

$$\bar{\bar{P}} = \begin{pmatrix} p & 0 & 0 \\ 0 & p & 0 \\ 0 & 0 & p \end{pmatrix} \tag{1.3.10}$$

   In such a case $\vec{\nabla} \cdot \bar{\bar{P}} = \vec{\nabla} p$.

3. the equation of conservation of energy (state equation);

$$\frac{d}{dt}\left(\frac{P}{P^{\gamma}}\right) = 0 \tag{1.3.11}$$

Here γ is the ratio of specific heats of plasma. The equation (1.3.11) is valid under condition where the heat flow is small. Note that P/P^{γ} is related to the entropy per unit mass of a fluid element.
The simplest closed system is known as the **cold plasma approximation**, and it contains only the continuity and fluid equations. In order to close the system the kinetic pressure P is taken to be zero. A zero kinetic pressure implies a zero plasma temperature, ($T \propto P$) and therefore a zero thermal velocity of plasma particles. Even if this could seem a too simplified model, there exist many conditions in which thermal velocity can be neglected. For this reason the cold plasma approximation will be used in chapter 2 to find the dispersion relation of electromagnetic waves propagating in the plasmas.
The **warm plasma approximation** considers also the third momentum of Vlasov equation, i.e. the state equation, neglecting the heat flux tensor as in equation (1.3.11).
The complete set of MHD equations is obtained by adding the Maxwell equations to the (1.3.8), (1.3.9) and (1.3.11):

$$\begin{cases} \vec{\nabla} \times \vec{E} = -\frac{\partial \vec{B}}{\partial t} \\ \vec{\nabla} \times \vec{B} = \mu_0 \left(n_i q_i \vec{v}_i + n_e q_e \vec{v}_e\right) + \mu_0 \epsilon_0 \frac{\partial \vec{E}}{\partial t} \\ \frac{\partial n_j}{\partial t} + \vec{\nabla} \cdot (n_j \vec{v}_j) \qquad j = i, e \\ m_j n_j \left[\frac{\partial \vec{v}_j}{\partial t} + (\vec{v}_j \cdot \vec{\nabla})\vec{v}_j\right] = q_j n_j \left(\vec{E} + \vec{v}_j \times \vec{B}\right) - \vec{\nabla} p_j \qquad j = i, e \\ p_j = C_j n_j^{\gamma_j} \qquad j = i, e \end{cases} \tag{1.3.12}$$

The set of Equations (1.3.12) need to be solved either for the electron fluid and for the ion fluid. The divergence equations present in the set of Maxwell equations can be neglected because they can be recovered by making the divergence of curl equation.
The solution of the set of 16 scalar equation in the 16 unknowns n_i, n_e, p_i, p_e, $\vec{v}_i$, $\vec{v}_e$, $\vec{E}$ and $\vec{B}$ gives a self-consistent set of fields and motions in the

fluid approximation.
If we take into account the plasma quasi-neutrality (i.e. $n_e \simeq n_i$), and we neglect the ratio m_e/m_i, we can consider only large scale and low-frequency phenomena. We finally consider that the system remain isotropic at all times. These hypothesis enable us to add the set of equation for ions and electrons, obtaining the **Single fluid MHD equations** [1]:

$$\vec{\nabla} \times \vec{E} = -\frac{\partial \vec{B}}{\partial t} \tag{1.3.13}$$

$$\vec{\nabla} \times \vec{B} = \mu_0 \vec{j} \tag{1.3.14}$$

$$\frac{\partial \rho}{\partial t} + \vec{\nabla} \cdot (\rho \vec{v}) \tag{1.3.15}$$

$$\rho \frac{\partial \vec{v}}{\partial t} = \vec{j} \times \vec{B} - \vec{\nabla} p \tag{1.3.16}$$

$$\vec{E} + \vec{v} \times \vec{B} = \eta \vec{j} \tag{1.3.17}$$

where the (1.3.13) and (1.3.14) are the Maxwell equations, 1.3.15 is the mass continuity equation, the (1.3.16) is the momentum transport equation, the (1.3.17) is the Ohm's law.

1.3.4 Some applications of MHD equations

Several physical concepts are easily gleaned from the MHD equations. For a steady state, from equations (1.3.16) and (1.3.14), it follows that:

$$\vec{\nabla} p = \mu_0^{-1} \left(\vec{\nabla} \times \vec{B} \right) \times \vec{B} \tag{1.3.18}$$

By simplifying the previous equation:

$$\vec{\nabla} \left(p + \frac{B^2}{2\mu_0} \right) = \mu_0^{-1} \left(\vec{B} \cdot \vec{\nabla} \right) \vec{B} \tag{1.3.19}$$

In many interesting cases, such as a straight cylinder with axial field, the right-hand side vanishes. In many other cases the right-hand side is small. Equation (1.3.19) then becomes:

$$p + \frac{B^2}{2\mu_0} = constant \tag{1.3.20}$$

Since $B^2/2\mu_0$ is the magnetic field pressure, the sum of the particle pressure and the magnetic field pressure is a constant. In a plasma with a density

gradient, the magnetic field must be low where the density is high, and viceversa. The decrease of the magnetic field inside the plasma is caused by the diamagnetic current. The size of the diamagnetic effect is indicated by the ratio of the two terms in equation (1.3.20). This ratio is usually denoted by β:

$$\beta \equiv \frac{\sum n\kappa T}{B^2/2\mu_0} \tag{1.3.21}$$

Generally, β can be used to determine the quality of the plasma confinement:

1. $\beta << 1$: Then the magnetic pressure is much higher than the plasma kinetic pressure; this is the condition for an optimal confinement;
2. $\beta = 1$: The diamagnetic effect generate an internal magnetic field exactly equal to the external one and two regions exist: one where only the magnetic field is present, the other where only the plasma, without magnetic field, exists;
3. $\beta > 1$: The plasma pressure is higher than that due to the magnetic field, then the plasma cannot be magnetically confined;

The magnitude of the diamagnetic current can be found by taking the cross product of equation (1.3.16) with $\vec{B}$ in the equilibrium case ($\partial/\partial t = 0$):

$$\vec{j} = \frac{\vec{B} \times \vec{\nabla} p}{b^2} = (KT_i + KT_e)\frac{\vec{B} \times \vec{\nabla} n}{b^2} \tag{1.3.22}$$

The $\vec{j} \times \vec{B}$ force generated by the diamagnetic current balances the pressure force in steady state and stop the motion, as shown in figure (1.3.1).

1.4 Particle motion in a magnetized plasma

In this section the motion of electrons and ions within a magnetized plasma will be analyzed by following the single particle approach discussed in section 1.3.1. In section 1.2 it has been shown that collision frequencies have different importance for electrons and ions: electrons can be considered non-collisional while ions are strongly collisional.
The general motion equation for an electron moving in an external magnetic field in absence of collisions:

$$m_e \frac{d\vec{v}}{dt} = q\vec{v} \times \vec{B} \tag{1.4.1}$$

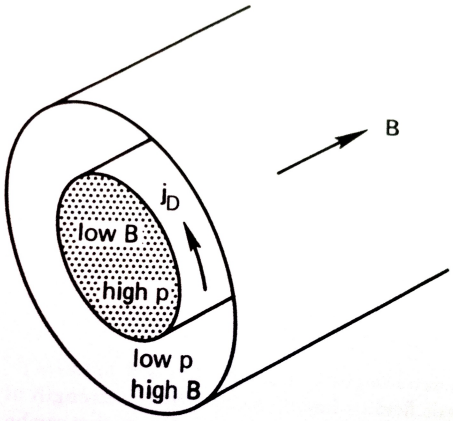

Figure 1.3.1: Diamagnetic current and magnetic field direction in cylindrically shaped plasma

The reference system can be defined in order to have the magnetic field oriented along the z axis, so that $\vec{B}$ can be written as $\vec{B} = B\hat{z}$. The solution of equation (1.4.1) is then:

$$\begin{aligned} v_x &= v_{0\perp}\cos(\omega_c t + \phi) \\ v_y &= -v_{0\perp}\sin(\omega_c t + \phi) \\ v_z &= v_{z0} \end{aligned} \tag{1.4.2}$$

where $v_{0\perp}$ is the component of the velocity orthogonal to the magnetic field, $\phi = \arctan(-\frac{v_{0y}}{v_{0x}})$ is the phase, and ω_c is the **cyclotron frequency**:

$$\omega_c = \frac{|q|B}{m_e} \tag{1.4.3}$$

Equation (1.4.2) tell us that electrons move along the direction of the magnetic field with helicoidal trajectories. The electron gyration radius, usually called *Larmor radius* is equal to:

$$r_L = \frac{m_e v_\perp}{|q|B} \tag{1.4.4}$$

Therefore, for electrons the space is no more isotropic and the presence of the magnetic field introduces a preferential direction along $\hat{z}$.

The ion equation motion can not neglect longer the presence of collisions. Equation (1.4.1) becomes:

$$m\frac{d\vec{v}}{dt} = q\vec{v} \times \vec{B} - m\omega_{coll}\vec{v} \tag{1.4.5}$$

where ω_{coll} represents the collision frequency multiplied by 2π.
When the collisions are taken into account, the velocity components of equation (1.4.2) are multiplied by the term $e^{-\omega_{coll}t}$.
This means that, for time-scale larger than $1/\omega_{coll}$, the mean velocity of ions goes to zero[6]. Hence ions are no longer influenced by the magnetic field and they can be considered unmagnetized.

1.4.1 Drift effects in plasmas

External or internal forces can affect the motion of particles in a magnetized plasma. Such forces can be superimposed from outside[7] or self-generated from inside the plasma[8]. Their effect is to modify the original cyclotron motion of the particle, adding a drifting component to the velocity.
Only the component of the force perpendicular to the magnetic field $F_\perp$ has importance in the resolution of the problem. The F_z component, in facts, generates simply an acceleration along the z axis and it does not interact with $\vec{B}$ ($\vec{F_z} \times \vec{B} = 0$) For sake of simplicity, thus, we may choose $\vec{F}$ to lie in the $x - y$ plane. In presence of such force, the equation motion becomes:

$$m\frac{d\vec{v}}{dt} = q\vec{v} \times \vec{B} + \vec{F} \tag{1.4.6}$$

It can be shown [1] that the solution of equation (1.4.6) is given by the sum between the velocity component of equation (1.4.2) and a constant vector.
To find the module and the direction of the drift velocity $\vec{v}_d$ is hence sufficient to solve equation (1.4.6) for the constant vector $\vec{v} = \vec{v}_d$:

$$\vec{F} + q\vec{v}_d \times \vec{B} = 0 \tag{1.4.7}$$

taking the cross product with $\vec{B}$, one finds:

$$\vec{F} \times \vec{B} + q\vec{v} \times \vec{B} \times \vec{B} = qvB^2 - q\vec{B}(\vec{v} \cdot \vec{B}) \tag{1.4.8}$$

[6] In reality also if $< v >= 0$, $< v^2 >$ is ever different from zero, allowing ion diffusion.
[7] For example, in RF ion sources[4], plasma is generated by means of a variable electric field superimposed to electron motion.
[8] In many cases[86], as the one described in the experimental chapters of this work, the plasma heating mechanism is able to self-generate strong electric field.

looking at the transverse component of $\vec{v}$ with respect to $\vec{B}$, we finally have:

$$\vec{v}_d = \frac{\vec{F} \times \vec{B}}{qB^2} \tag{1.4.9}$$

Equation 1.4.9 shows that the direction of $\vec{v}_d$ depends on the sign of charge, so in general ion and electrons, under the effect of the same force, drift in oppositive directions. As it was explained previously, in ECRIS and MDIS ions are unmagnetized, so they can not be affected by drift motions, depending on the interaction between $\vec{F}$ and the effective magnetic field. However, if ion lifetime is long enough to allow momentum transfer among ions and electrons, the drifting electrons can accelerate ions via $e - i$ collisions. In many practical cases, the force generating the electron drift is due to the action of uniform or a non-uniform electric field on plasma electrons. These two case will be treated separately. For sake of generality also drift effect on ions will be taken into account.

- Drift generated by an uniform electric field;

In such case equation (1.4.9) becomes:

$$\vec{v}_d = \frac{\vec{E} \times \vec{B}}{B^2} \tag{1.4.10}$$

The drift velocity $\vec{v}_d$ is independent of q, m and $\vec{v}_\perp$. Both ions and electrons are drifted in the same direction with the same drift velocity whose module is $|v_d| = E/B$.

- Drift generated by a non-uniform electric field;

Self-generated electric fields have often a wave behaviour and they generally vary both in space and time as $\vec{E} = \vec{E}_0 e^{i(\vec{k}\cdot\vec{r}-\omega t)}$. For an arbitrary variation of $\vec{E}$ in space, and a sinusoidal variation in time, it can be shown [1] that equation (1.4.10) can be rewritten as:

$$\vec{v}_d = \frac{\vec{E} \times \vec{B}}{B^2} + \frac{1}{4} r_L^2 \nabla^2 \left(\frac{\vec{E} \times \vec{B}}{B^2} \right) \pm \frac{1}{\omega_c B} \frac{d\vec{E}}{dt} \tag{1.4.11}$$

In last term the sign $\pm$ stands for the signs of the particle charge.
If one assumes $\vec{E}$ varying sinusoidally also in space, the previous equation can be written as:

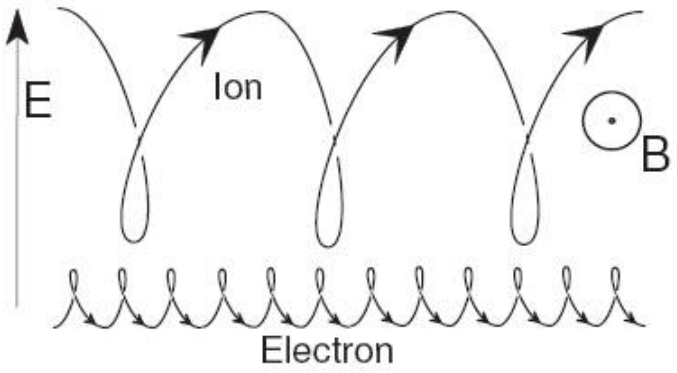

Figure 1.4.1: *Motion of a charged particle subjected to an external magnetic filed* $\vec{B}$ *and to an electric field* $\vec{E}$.

$$\vec{v}_d = \frac{\vec{E}\times\vec{B}}{B^2} - \frac{1}{4}r_L^2 k^2 \left(\frac{\vec{E}\times\vec{B}}{B^2}\right) \pm \frac{1}{\omega_c B}\frac{d\vec{E}}{dt} \tag{1.4.12}$$

Equations (1.4.11) and (1.4.12) show that the motion of the guiding center has two components, one perpendicular to $\vec{B}$ and $\vec{E}$, and one directed along the direction of $\vec{E}$. The first term of equation (1.4.11) corresponds to the drift velocity in case of uniform electric field. The second term is called the *finite-Larmor-radius effect*. Since r_L is much larger for ions than for electrons $\vec{v}_d$ is no longer independent of species. However the effects due to this term are important only for relatively large k (small wavelength) or small scale length of inhomogeneity. The third term is called *polarization drift* and it also depends on the charge of the particle. It is directed along the direction of the Electric field and it tends to separate ions from electrons. When a field $\vec{E}$ is suddenly applied, for example, ions move in direction of $\vec{E}$, while electrons will move in the oppositive direction. The polarization effect in a plasma is similar to that in a solid dielectric, where $\vec{D} = \epsilon_0\vec{E} + \vec{P}$. The dipoles in a plasma are ions and electrons separated by a distance r_L. The polarization current generated by the oppositive motion of ions and electrons (for Z=1) is:

$$\vec{j}_p = ne(v_{ip} - v_{ep}) = \frac{n}{B^2}(m_i + m_e)\frac{d\vec{E}}{dt} \cong \frac{m_i}{B^2}\frac{d\vec{E}}{dt} \tag{1.4.13}$$

Clearly since ions and electrons can move around to preserve quasi-

neutrality, the application of a steady $\vec{E}$ field does not result in a polarization field $\vec{P}$. However, if $\vec{E}$ varies sinusoidally as $\vec{E} = \vec{E}_0 e^{i\omega t}$, then an oscillating current $\vec{j_p}$ results from the lag due to the ion inertia. In such a case the polarization current $\vec{j_p}$ will be:

$$\vec{j_p} = \frac{m_i n \omega}{B^2} \vec{E}_0 e^{i\omega t} \tag{1.4.14}$$

1.5 Plasma diffusion

The plasma diffusivity plays a very important role because it strongly influences the lifetime, the charge state distribution and hence the performance of the source. This implies that the knowledge of the particle loss mechanisms in plasmas may play a fundamental role for the enhancement of the performance of such devices [14].

1.5.1 Free diffusion

The diffusivity arises because of the presence of the collisions among the particles of the plasma. A fluidodynamics approach [1] shows that, in absence of electric and magnetic fields, the flux of particles $\vec{\Gamma} = n\vec{u}$ is related to the density and electric field by means of the following law:

$$\Gamma = \pm T n \vec{E} - D \vec{\nabla} n \tag{1.5.1}$$

where the sign depends on the charge of the species, positive for ions and negative for electrons. T and D are the mobility and diffusion coefficient defined as:

$$T = \frac{|q|}{m\nu} \tag{1.5.2}$$

$$D = \frac{k_B T}{m\nu} \tag{1.5.3}$$

with ν the collision frequency. The transport coefficients T and D are connected each other by the *Einstein relation*:

$$\mu = \frac{|q| D}{K_B T} \tag{1.5.4}$$

Fick's law of diffusion is a special case of equation (1.5.1), occurring when either $\vec{E} = 0$ or the particle are uncharged, so that $T = 0$:

$$\vec{\Gamma} = -D \vec{\nabla} n \tag{1.5.5}$$

The root mean square path covered by a particle in a time t. It is proportional to the diffusion coefficient [5]:

$$\langle x^2 \rangle = \frac{D}{2} t \tag{1.5.6}$$

Equation (1.5.5) merely express the fact that diffusion is a random-walk process, in which a net flux from dense regions to less dense regions occurs simply because more particles start in the dense region. This flux is obviously proportional to the gradient of the density. In plasma, Fick's law is not necessary obeyed. Because of the possibility of organized motions (plasma waves), a plasma may spread out in a manner which is not truly random. Both equations (1.5.1) and (1.5.5), furthermore, show that if free diffusion were possible, electrons could diffuse faster than ions because of their smaller mass. This is clearly not reasonable in the case of the plasmas, because of the quasi-neutrality principle. So, if electrons could diffuse far away from ions, a strong electric field would arise as to retard the loss of electrons and accelerate the ion loss. This property is usually called **Ambipolar diffusion**. In such conditions the fick law is yet valid, but the new diffusion coefficient is given by [12]:

$$D_a = \frac{\mu_i D_e + \mu_e D_i}{\mu_i + \mu_e} \tag{1.5.7}$$

By virtue of its definition, the diffusion coefficient is mostly determined by the slower species, usually ions. The magnitude of D_a can be estimated by noting that $\mu_e \gg \mu_i$ and by using Einstein relation (1.5.4):

$$D_a \simeq D_i \left(1 + \frac{T_e}{T_i} \right) \tag{1.5.8}$$

The previous formula is valid **only** in case of free diffusion, i.e. when electron mobility is larger than the ion one.

1.5.2 Ambipolar diffusion in a magnetized plasma and short-circuit effects

As it will be detailed explained in chapter 3, MDIS and ECR ion sources are characterized by strong magnetic fields (0.1 T in MDIS and several Tesla in the new generation ECRIS), hence it is important to study the effects of a magnetic field on the diffusion mechanisms. In section 1.4 it was demonstrated that the plasma particles in a magnetic field are forced to move along

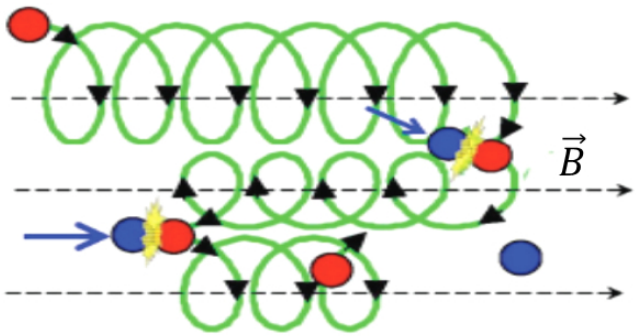

Figure 1.5.1: *A charged particle in a magnetic field will gyrate about the same line of force until it makes a collision, only the collisions can allow the motion across* $\vec{B}$.

their gyration orbits and, in absence of collisions, they cannot diffuse across the magnetic field. Only by means of collisions, the particles can move to a different force line, as shown in figure 1.5.1. The Lorentz force does not act along the magnetic field, therefore, along z, the diffusion mechanism occurs as in the case of unmagnetized plasmas. In presence of a magnetic field, hence, diffusion is no longer isotropic, but it is necessary to distinguish between the diffusion along or across the magnetic field, characterized respectively by the diffusion coefficients $D_{\parallel}$ and $D_{\perp}$.

In MDIS and ECRIS ion sources, as demonstrated in section 1.2, ions are unmagnetized because of the strong collisionality, while electrons can be considered collisionless (in ECRIS), or almost quasi-collisionless (in MDIS). This means that in such devices ions diffuse isotropically and only the electron diffusion is affected by the external magnetic field. The effect of a strong magnetic field is indeed to reduce the coefficient of diffusion for electrons to the value [1]:

$$D_{\perp} = \frac{D}{1 + \omega_c^2 \tau^2} \tag{1.5.9}$$

where ω_c and τ are respectively the cyclotron frequency and the mean time between collisions. In the limit $\omega_c^2 \tau^2 \gg 1$ we have:

$$D_{\perp} = \frac{kT\nu}{m\omega_c^2} \tag{1.5.10}$$

Comparing with equation (1.5.3), we see that the role of the collision fre-

quency ν has been reversed. In diffusion perpendicular to $\vec{B}$, $D_\perp$ is proportional to ν, since collisions are needed for cross-field migration. On the contrary, the ions, being unmagnetized, diffuse faster with diffusion coefficient given by equation (1.5.3). It might be supposed that, also in such a case, an ambipolar diffusion would arise, in order to reduce the ion losses and accelerate the electron diffusion across $\vec{B}$. Simon shown [13] that in a medium with anisotropic diffusivity the equalization of losses along and across the magnetic field it is not necessary, but it is sufficient that the excess of positive charge lost across $\vec{B}$ is balanced by the negative charge lost along $\vec{B}$. In other words the resultant negative current directed axially must be equal to positive current directed radially. If the walls are made of conductive materials, the current can flow through the wall, creating a short-circuit, as it is shown in figure 1.5.2. The absence of ambipolar diffusion allows the radial loss rate be regulated by the faster species, i.e. the ions. Radial diffusion increase up to 100 times with respect to the expected values in case of ambipolar diffusion [13]. This effect increases the losses of the plasma influencing negatively the performances of the source in terms of electron density and mean charge state. In the course of time various techniques have been applied to improve the performance of an electron cyclotron resonance ion source [14], in particular the use of Bias disk [15] decreasing the axial electron losses, the use of insulators like Alumina (Al_2O_3) and boron nitride [16] covering the walls of the plasma chamber and blocking the short circuit on the walls or the use of carbon nanotubes based electron gun [17], whose effect is to compensate the radial ion current, restoring the ambipolar diffusion.

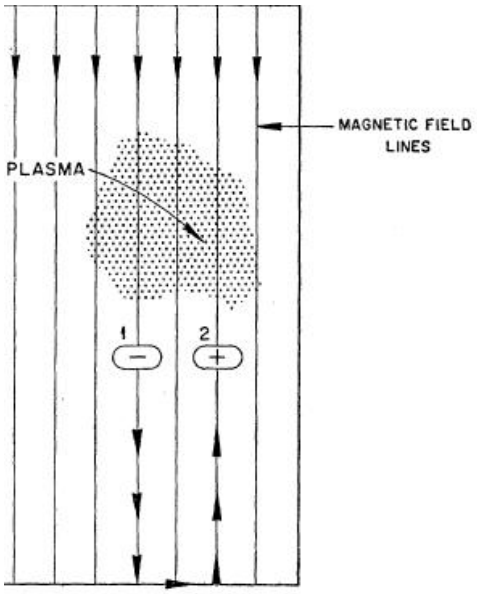

Figure 1.5.2: *Illustration of the short-circuit effect.*

1.6 Plasma confinement

As it was introduced in section 1.2, the ion lifetime in the plasma is a key parameter for the generation of highly charged ions. According to equation (1.2.10), confinement time τ_c must be large enough to guarantee the step-by-step ionization up to high charge states. Plasma confinement is obtained by means of magnetic structures able to reflect back a large part of plasma particles which leave the plasma core.

1.6.1 The simple mirror configuration

The most simple device for plasma confinement was early investigated by Fermi and it is named **Simple Mirror** [8]. In this magnetic configuration the field is provided by two solenoids with coinciding axes, located to definite distances each other. Figure 1.6.1 features the shape of the field lines. When the current on the two circular solenoids flows in parallel directions with each other, the magnetic field strength near both coils increases while it remains weak between them.

Transversally, i.e. along the perpendicular direction with respect to the

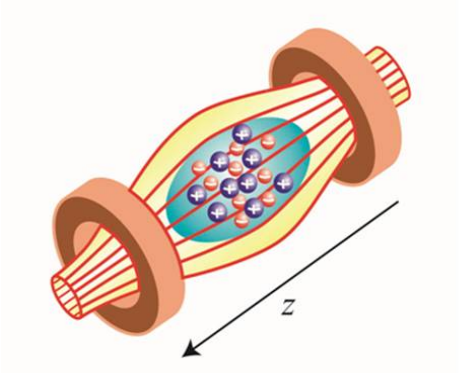

Figure 1.6.1: *Magnetic field lines produced in a simple mirror configuration. The density of the field lines increases at the extremities of the trap, and this generates the gradient which allows the confinement of the charged particles.*

mirror axis, the particles are automatically confined because they gyrate around the magnetic field lines. From the Lorentz force comes that the component along the z axis can be written as:

$$F_z = \frac{1}{2} q v_\phi r \frac{\partial B_z}{\partial z} \tag{1.6.1}$$

By averaging over one gyration, considering a particle moving along the mirror axis, we obtain [1]:

$$\bar{F}_z = -\frac{1}{2} \frac{m v_\perp^2}{B} \frac{\partial B_z}{\partial z} \tag{1.6.2}$$

We define the *magnetic moment* of the gyrating particle to be:

$$\mu \equiv \frac{1}{2} \frac{m v_\perp^2}{B} \tag{1.6.3}$$

Where $v_\perp$ is the velocity component orthogonal to $\vec{B}$. Then the force along z becomes:

$$\bar{F}_z = -\mu \frac{\partial B_z}{\partial z} \tag{1.6.4}$$

Generalizing for a whatever gradient along the particle motion, the force parallel to B is:

$$\vec{F}_\parallel = -\mu \vec{\nabla}_\parallel B \tag{1.6.5}$$

The magnetic moment μ is an adiabatic invariant for the particle motion [1]. The confinement of charged particles in mirror-like devices can be studied in terms of μ invariance. The adiabatic invariance is valid as long as the spatial scale of the field uniformity is large with respect to the gyroradius:

$$\frac{B}{\nabla B} \ll \rho_L \tag{1.6.6}$$

If such condition is not satisfied, non-adiabatic effects begin to play their role, leading to the expulsion of the particle from the confinement. The ability in confining the particles by means of a simple mirror depends on the so called *loss cone aperture* [2]. In facts, the particles having $v_\perp \approx 0$, and therefore $\mu \approx 0$, do not feel any confining force $\vec{F}_\parallel$. In general, there exist a minimum value of $v_\perp$, below which the particles are lost because the magnetic force (1.6.2) cannot guarantee the mirroring. By defining θ as the angle between the particle velocity $\vec{v}$ and $\vec{B}$, starting from the conservation of magnetic moment, it is possible to demonstrate that the particle is lost if:

$$\theta < \theta_{min} = \sin^{-1}\sqrt{\frac{B_{min}}{B_{max}}} \tag{1.6.7}$$

Where B_{min} and B_{max} represent the minimum and maximum magnetic field of the mirror. The equation (1.6.7) defines the loss cone. A representation of the loss cone is shown in figure 1.6.2.

The mirror motion implies a second quasi-periodic motion for a particle in a mirror magnetic field, i.e. the motion from one mirror point to the opposite and back with a bouncing frequency ω_b. This second adiabatic invariant is the *longitudinal invariant* J, defined as [1]:

$$J = \oint_a^b m v_\parallel dl \tag{1.6.8}$$

where a and b are the turning point over which the particles bounce in a confining magnetic field. J determines the length of the force lines traversed from the particles between the two reflection points, and its invariance means that the particle will move, after being subjected to reflection, on the same force line. The force lines with the same value of J define the surface on which will move the particles with a given value of W/μ, W being the kinetic energy of the particle. Mirror Confinement systems are designed so that these $J = constant$ surfaces do not intersect a material wall. The bouncing frequency of the magnetic system depends on $v_\perp$ and the properties of the

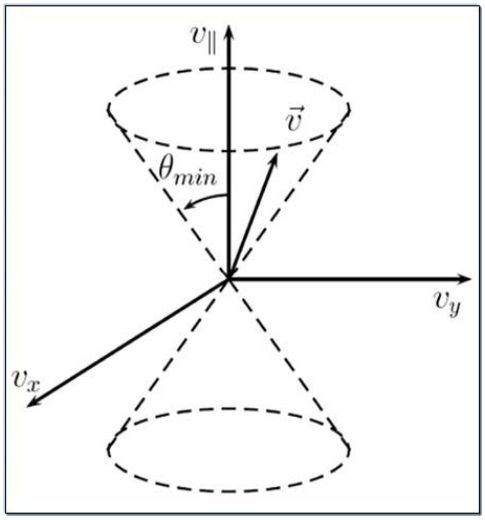

Figure 1.6.2: *Schematic representation of the loss cone in the velocity space; θ_{min} indicates the cone aperture.*

magnetic field B. It can be found from the motion equation along the z axis [10]:

$$m\ddot{z} = -\mu\frac{\partial B_z(z)}{\partial z} \tag{1.6.9}$$

In simple mirrors the magnetic field components can be described as it follows [11]:

$$\begin{cases} B_r = -rzB_1 \\ B_z = B_0 + B_1 z^2 \end{cases} \tag{1.6.10}$$

Replacing $\dfrac{\partial B_z(z)}{\partial z}$ calculated from equation (1.6.10) and substituting into equation (1.6.9), it comes out the equation of an harmonic oscillator, whose frequency is clearly the bouncing frequency ω_b:

$$\ddot{z} = \omega_b^2 z, \qquad \omega_b = \sqrt{\frac{2\mu B_1}{m}} = \sqrt{\frac{B_1}{B_0}}v_{\perp 0} \tag{1.6.11}$$

The bouncing frequency ω_b increases with $v_{\perp 0}$ and therefore with the component of electron energy orthogonal to B. Its role in plasma heating will be clarified in section 2.2. Even if ω_b was obtained by the motion

equation in a simple mirror, equation (1.6.11) is valid also in more complex magnetic configurations, as the B-minimum configuration we are going to introduce.

1.6.2 The B-minimum configuration

Simple mirror represents one of the more simple magnetic systems enabling plasma confinement. These magnetic structures are stable by the point of view of a single particle approach, however, a MHD approach demonstrates that different instabilities can arise in the central region of the mirror, leading to a plasma flux in perpendicular direction with respect to the mirror axis [2]. The more efficient magnetic system able to guarantee the plasma confinement is the so called **minimum B structure**[9]. In such configuration, the magnetic field increases in every direction away from the plasma boundary, and there not exist any region where the magnetic field goes to zero inside the plasma. The scattering of the particles in the loss cone is essentially due to the Spitzer collisions. Such a configuration can be obtained as a superposition of two different magnetic fields: one created by two solenoids (simple mirror), and the other created by six conductors surrounding the plasma chamber (an hexapole), as shown in figure 1.6.3. In this way the magnetic field increases in every direction going from the plasma. Ioffe demonstrated [9] on B-min configurations that the confinement times are one hundred times higher than simple mirrors. Hence the B-minimum structure represents the fundamental magnetic configuration characterizing the ECRIS. Such a structure enables them to increase ion lifetime and to generate highly charged ion currents. A complete description of the particle motion and of the ion confinement in a B-minimum structure is beyond the scopes of the present work. A more detailed analysis can be found in reference [10].

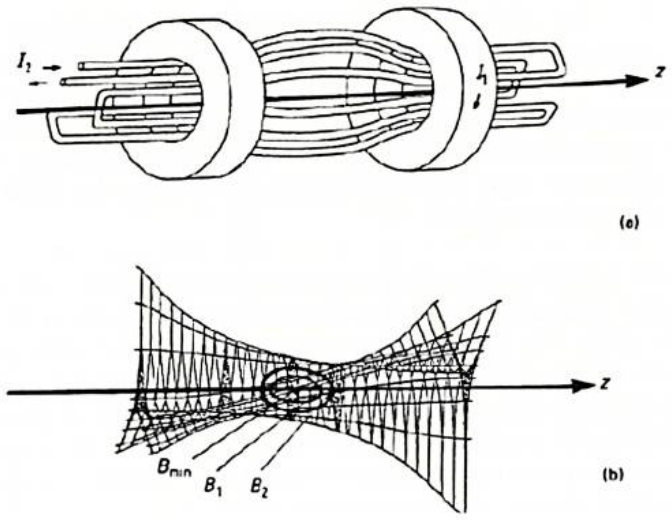

Figure 1.6.3: *Magnetic system (a) and magnetic field structure (b) obtained by the superposition of the field produced by two solenoids and an hexapole (minimum-B field).*

Chapter 2

Waves in plasmas

The study of wave propagation has an extraordinary importance in plasma physics. MDIS and ECRIS plasmas, in facts, are generated and sustained by means of the interaction with E.M. waves. Furthermore, electrostatic waves (E.S.) can be generated within plasmas, able to strongly influence the Electron Energy Distribution Function (EEDF) or modifiy the diffusion rates of the species. Plasma Waves are always associated with a time and space varying electric field, and the propagation properties of such fields are determined by the dielectric properties of the medium, which in turn depend on applied magneto-static or electrostatic fields. A plasma may be both inhomogeneous and anisotropic, and this affects its dielectric properties. The anisotropy can be easily induced by a magneto-static field, if any. MDIS and ECRIS plasmas, for example, are anisotropic media by the point of view of electromagnetic wave propagation. The first part of the chapter will be dedicated to the interaction between E.M waves and plasmas, with particular attention to the mechanisms which take to the Electron Cyclotron Resonance in ECRIS and to the microwaves energy absorption in MDIS. The second part will be dedicated to an introduction to E.S. waves and to the study of the E.M waves to E.S. waves coupling. Finally the last part of the chapter will be dedicated to the complete characterization of the Electrostatic Bernstein waves (EBW). EBW, in facts, enables us to obtain electron densities and temperatures much higher than the usual E.C.R heating, in such a way increasing the quality factor of the ion sources.

2.1 Propagation of E.M. waves in plasmas

A complete analysis of the waves propagation in a magnetized plasma should take into account the effects of the wave on the different plasma particles. Wave and particles dynamics are in facts reciprocally influenced. If the thermal velocity of the particle is low with respect to the wave's phase velocity, i.e. $v_{th} \ll v_\phi$, v_{th} can be neglected. This approximation, usually called **"cold plasma approximation"**, is equivalent to set $T_e = T_i = 0$ and consequently, P=0 in equation (1.3.9). Waves that depend on finite temperature effects, such as ion acoustic waves or Bernstein waves, can not be deduced by this treatment. Accordingly, for waves with very small phase velocities, **warm plasma approximation** must be used (see subsection 1.3.3 for further details). The E.M. waves propagate in the plasma with phase velocity of $10^7 - 10^8 m/s$, values much higher than the particles thermal velocity ($10^3 - 10^5 m/s$), except for the restricted regions where the waves exhibit resonances[1]; therefore, the cold plasma model is a useful approximation to determine the dispersion relation of the E.M wave in a magnetized plasma. In the following only the propagating electric field on E.M. wave will be considered. The module of magnetic force due to the influence of the magnetic field of the wave, in facts, is [3]:

$$F_m = \frac{v}{c}\sqrt{\epsilon_r} qE \tag{2.1.1}$$

Thus, for particles velocity $v << c$ the magnetic field of the wave can be neglected. This approximation is totally valid in the case of MDIS, whereas in ECRIS only a little part of hot electrons (see section 1.2.3) can reach relativistic energies, then being influenced by the magnetic field of the wave. For the scope of this section the magnetic effect can be neglected.
ECRIS and MDIS operative frequencies range between 2.45 GHz and some tens of GHz. At so high frequency ions are unsensitive to the electric field because of their high inertia, and their contribution in wave propagation can be neglected.

2.1.1 E.M. waves in a cold-unmagnetized plasma

In absence of a magnetic field, plasma is an isotropic medium. This means that the constitutive parameters assume the simple form of multiplicative

[1] As it will be shown in section 2.1.3, at the resonance the phase velocity of the E.M wave goes to zero.

constants. The fluid equation (1.3.9), in absence of magnetic field and in the cold plasma approximation becomes:

$$\frac{\partial \vec{v}}{\partial t} = q\vec{E} \tag{2.1.2}$$

Assuming that both electric field and velocity are varying in time as $e^{i\omega t}$, following the direction of the electric field, it can be easily shown that the dielectric constant is [3]:

$$\epsilon = \epsilon_0 \left(1 - \frac{\omega_p^2}{\omega^2}\right) \tag{2.1.3}$$

where ω_p is the **plasma frequency** and represents the natural oscillation frequency of an electron in a plasma (see section 2.4). The plasma frequency is proportional to the square root of the electron density:

$$\omega_p = \sqrt{\frac{ne^2}{\epsilon_0 m_e}} \tag{2.1.4}$$

As ϵ is defined positive, from equation (2.1.4) it follows that:

$$\left(1 - \frac{\omega_p^2}{\omega^2}\right) \geq 0 \quad \rightarrow \quad \omega^2 > \omega_p^2 \tag{2.1.5}$$

this means that electromagnetic waves with frequencies lower than ω_p cannot propagate into the plasma. As a consequence in *homogeneous and non magnetized plasmas the density cannot exceed the so called* ***cutoff density*** given by:

$$n_{cutoff} = 4\pi^2 \frac{m\epsilon_0}{e^2} f_p^2 \tag{2.1.6}$$

An overdense (i.e. above the cutoff) plasma would totally reflect the incoming (feeding) wave, so that the plasma would automatically adjust its own density to contemporary allow the maximum production with transparency for wave propagation. The cutoff density is consequently the main limitation of the plasmas generated by means of E.M waves. Plasmas having a density larger than the cut-off density, i.e. $n_e > n_{cutoff}$, are usually named **overdense**. When this condition is not satisfied, i.e. $n_e < n_{cutoff}$, the plasma is named **underdense**. The dispersion relation for waves in unmagnetized plasma is [2]:

$$\omega^2 - \omega_p^2 = k^2 c^2 \tag{2.1.7}$$

For the dispersion relation $\vec{k}$ is imaginary whenever $\omega < \omega_p$, implying the total reflection of the incident radiation, as it has been deduced from equation 2.1.3. In this case, assuming propagation along the x axis, the electric field in overdense region varies as:

$$\vec{E} = \vec{E}_0 e^{i\vec{k}\cdot\vec{r}-\omega t} = \vec{E}_0 e^{ikx-\omega t} = e^{\frac{x}{\delta}} e^{-i\omega t} \tag{2.1.8}$$

representing an evanescent oscillation whose amplitude in the medium decays exponentially with a characteristic distance δ called *skin depth*:

$$\delta = \frac{c}{\left(\omega_p^2 - \omega^2\right)^{\frac{1}{2}}} \tag{2.1.9}$$

Except for values close to ω_p, the penetration depth δ is of the order of 1 cm., i.e. small compared to most ECRIS plasma.

2.1.2 E.M. waves in a cold-Magnetized plasma

If we apply a magneto-static field to the plasma, then it will become an anisotropic medium for the electromagnetic waves propagation. Necessarily, the dielectric constant will transform in a tensor ($\bar{\bar{\epsilon}}$), as the field propagation will depend on the direction of propagation of the wave with respect to the external magnetic field.
Let's assume, without losing in generality, $\vec{B}$ directed along the z axis, so that it can be written as $\vec{B} = B_0\hat{z}$. It is possible to consider the plasma as a dielectric with internal current $\vec{j}$. As a consequence, the fourth Maxwell equation can be written as:

$$\vec{\nabla} \times \vec{B} = \mu_0 \left(\vec{j} + \epsilon_0 \frac{\partial \vec{E}}{\partial t} \right) = \mu_0 \frac{\partial \vec{D}}{\partial t} \tag{2.1.10}$$

By assuming a $e^{i\omega t}$ dependence for all plasma motions and by defining a conductivity tensor $\bar{\bar{\sigma}}$, by the relation $\vec{j} = \bar{\bar{\sigma}} \cdot \vec{E}$, it is possible to obtain the relation between $\vec{D}$ and $\vec{E}$:

$$\vec{D} = \epsilon_0 \left(\bar{\bar{I}} + \frac{i}{\epsilon_0 \omega} \bar{\bar{\sigma}} \right) \cdot \vec{E} \tag{2.1.11}$$

Where $\bar{\bar{I}}$ is the identity tensor. Remembering that, in a general way, $\vec{D}$ is linked to $\vec{E}$ by the relation:

$$\vec{D} = \epsilon_0 \bar{\bar{\epsilon_r}} \cdot \vec{E} \tag{2.1.12}$$

Then the effective dielectric constant of the plasma is the tensor:

$$\bar{\bar{\epsilon}} = \epsilon_0 \left(\bar{\bar{I}} + \frac{i}{\epsilon_0 \omega} \bar{\bar{\sigma}} \right) \tag{2.1.13}$$

To evaluate $\bar{\bar{\sigma}}$, we use the fluid equation (1.3.9). By neglecting the collisional effects and the pressure terms, according to the cold plasma approximation, one obtains:

$$m_i \frac{\partial \vec{v}}{\partial t} = e \left(\vec{E} + \vec{v}_s \times \vec{B} \right) \tag{2.1.14}$$

This vectorial equation is equivalent to a system of three scalar equations, whose solution gives the relation between $\vec{v}$ and the electric field of the wave $\vec{E}$, therefore between $\vec{j}$ and $\vec{E}$, since $\vec{j} = ne\vec{v}$ and also $\vec{j} = \bar{\bar{\sigma}}\vec{E}$. For sake of brevity, the algebraic passages will be omitted and only the final value of the dielectric tensor $\bar{\bar{\epsilon}}$, obtainable from $\bar{\bar{\sigma}}$ by means of relation (2.1.13), is shown:

$$\bar{\bar{\epsilon}} = \epsilon_0 \begin{vmatrix} S & -iD & 0 \\ iD & S & 0 \\ 0 & 0 & P \end{vmatrix} \equiv \epsilon_0 \bar{\bar{\epsilon}}_r \tag{2.1.15}$$

where S, D and P are respectively [1]

$$S \equiv 1 - \frac{\omega_p^2}{\omega^2} \left(\frac{1}{1 - \omega_c} \right) \tag{2.1.16}$$

$$D \equiv -\frac{\omega_p^2}{\omega^2} \frac{\omega_c}{\omega} \left(\frac{1}{1 - \omega_c} \right) \tag{2.1.17}$$

$$P \equiv 1 - \frac{\omega_p^2}{\omega^2} \tag{2.1.18}$$

We can derive the wave equation by taking the curl of the Maxwell equation $\vec{\nabla} \times \vec{E} = -\dfrac{\partial \vec{B}}{\partial t}$ and remembering equations (2.1.10) and (2.1.12) we obtain:

$$\vec{\nabla} \times \vec{\nabla} \times \vec{E} = -\mu_0 \epsilon_0 \bar{\bar{\epsilon}}_r \cdot \frac{\partial^2 \vec{E}}{\partial t^2} = -\frac{1}{c^2} \bar{\bar{\epsilon}}_r \cdot \frac{\partial^2 \vec{E}}{\partial t^2} \tag{2.1.19}$$

Finally, by assuming an $e^{i\vec{k}\cdot\vec{r}}$ spatial dependence of the electric field, and by introducing the vectorial index of refraction, we can write:

$$\vec{k} \times \vec{k} \times \vec{E} + \frac{\omega^2}{c^2} \bar{\bar{\epsilon}}_r \cdot \vec{E} = 0 \tag{2.1.20}$$

If θ is the angle between the wave vector and the magnetic field $\vec{B}_0$, and remembering that the vector $\vec{N}$ is linked to $\vec{k}$ by means of the relation:

$$\vec{N} = \frac{c}{\omega}\vec{k} \tag{2.1.21}$$

the previous equation can finally be written as:

$$\begin{pmatrix} S - N^2\cos^2\theta & -iD & N^2\cos\theta\sin\theta \\ iD & S - N^2 & 0 \\ N^2\cos\theta\sin\theta & 0 & P - N^2\sin^2\theta \end{pmatrix} \begin{pmatrix} E_x \\ E_y \\ E_z \end{pmatrix} = 0 \tag{2.1.22}$$

Equation (2.1.22) is a set of three simultaneous, homogeneous equations. The condition for the existence of a solution is that the determinant of the coefficient matrix vanishes. This condition, finally, gives out the **relation dispersion** for E.M waves in plasmas:

$$\left(S\sin^2\theta + P\cos^2\theta\right) N^4 + \left(RL\sin^2\theta + SP(1+\cos^2\theta)\right) N^2 + PRL = 0 \tag{2.1.23}$$

where, for sake of simplicity, we defined $R = S+D$ and $L = S-D$. Equation (2.1.23) contains all the information about the propagation of the waves in magnetized plasma. it has two solutions:

$$N^2_{o,x}(\theta) = 1 - \frac{2X(1-X)}{2(1-X) - Y^2\sin^2\theta \pm \sqrt{Y^4\sin^4\theta + 4Y^2(1-X)^2\cos^2\theta}} \tag{2.1.24}$$

Hence for a given arbitrary direction, defined by θ, we have two waves characterized by different index of refraction. $N^o(\theta)$ is called **ordinary wave**, whereas $N^x(\theta)$ is named **extraordinary wave**. Here we have introduced two important parameters, X and Y, which will be very useful to simplify the mathematical notation:

$$X = \frac{\omega_p^2}{\omega^2} \propto n_e \qquad Y = \frac{\omega_c}{\omega} \propto B_0 \tag{2.1.25}$$

X is the parametric electron density, proportional to n_e, whereas Y is the parametric magnetic field, proportional to B_0.

2.1.3 Cutoffs and resonances

By means of equation (2.1.24) it is possible to determine the wave's propagation properties as a function of the angle θ, of the electron density n_e and of the magnetic field B_0. By definition, the index of refraction N is positive, so that the wave can propagate in the medium only if $N > 0$.
In general we can have four different cases:

- $N > 0$ **Propagation region**: The wave propagates in the medium with phase velocity given by c/N;
- $N < 0$ **Stop-band region**: The wave can not propagate;
- $N = 0$ **Cut-off**: The wave is reflected;
- $N \to \infty$ **Resonance**: The wave is absorbed by the medium.

According to equation (2.1.24), cutoffs can be found by setting $N = 0$. So they occur only when is verified the condition $PRL = 0$, i.e. when:

$$P = 0 \quad or \quad R = 0 \quad or \quad L = 0 \tag{2.1.26}$$

It is very important to note that condition (2.1.26) does not depend on θ. Thus **cutoffs does not depend on the angle of propagation** θ. From (2.1.26), thus we obtain the three cutoffs of E.M. in magnetized plasmas expressed as a function of plasma parameters:

1. $P = 0 \Rightarrow \omega = \omega_p$ or $X = 1$: as in unmagnetized plasmas, $\omega = \omega_p$ is a cutoff condition also in magnetized plasmas. This cutoff is usually named *O cutoff*;
2. $R = 0 \Rightarrow \omega = \omega_R = \frac{1}{2}\left[\sqrt{\omega_c^2 + 4\omega_p^2} + \omega_c\right]$ or $Y = 1 - X$: this cutoff is named *upper cutoff frequency* or *R cutoff*, occurring at frequency above both ω_p and ω_c;
3. $L = 0 \Rightarrow \omega = \omega_L = \frac{1}{2}\left[\sqrt{\omega_c^2 + 4\omega_p^2} - \omega_c\right]$ or $Y = X - 1$: this cutoff is named *lower cutoff frequency* or *L cutoff*, placed below ω_p;

Ordinary waves are reflected when $\omega_{RF} = \omega_p$ i.e at O cutoff. Extraordinary waves are unaffected by this cutoff and reflected at R and L cutoffs (they are not reflected at O cutoff, being, $N_2|^{X=1} \neq 0$). **Resonances** can be

!h

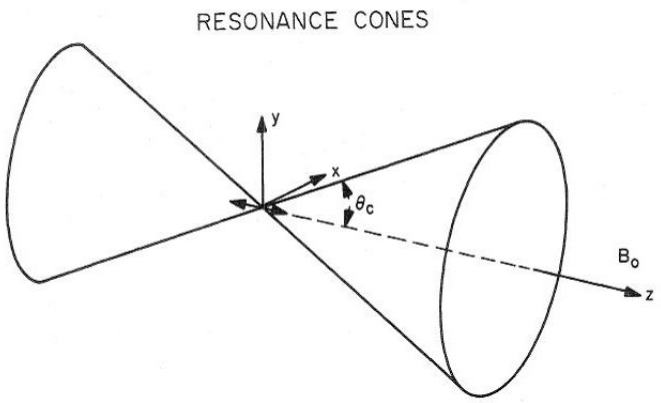

Figure 2.1.1: Resonance cones in a magnetized plasma. The wave encounters a resonance only on the surface of the cone of angle θ_c, where the relation $\tan^2\theta_r = -\dfrac{P}{S}$ is satisfied.

found by imposing the condition $N \to \infty$ in equation (2.1.23), which imply that the coefficient of the term of larger order (N^4) must go to zero[2]:

$$S\sin^2\theta + P\cos^2\theta = 0 \quad \rightarrow \quad \tan^2\theta_r = -\frac{P}{S} \tag{2.1.27}$$

The resonance angle θ_r can be written as a function of the plasma parameters as it follows:

$$\cos^2\theta_r = \frac{X + Y^2 - 1}{XY^2} \tag{2.1.28}$$

If the electron density and the applied magnetic field are almost constant[3], thus the resonance can occur only on the surface of a cone, named **resonant cone** [19], whose axis is aligned with the external magnetic field $B_0\hat{z}$ and with aperture angle θ_r, as displayed in figure 2.1.1. This cone corresponds to conical surfaces in the real space.

[2]to verify this it is sufficient to we set $M = 1/N^4$ in equation (2.1.23) and look for M=0 solution. When $M \to 0$, then $N \to 0$.

[3]This condition is valid, for example, in the magnetosphere.

The conditions for establishing of the resonances, thus, depend on the direction of wave propagation. By setting the denominator of equation (2.1.24) equal to zero it is possible to verify that only the extraordinary wave can have resonances. Equation (2.1.28) enable us to calculate the value of X and Y needed to have a resonance at the angle θ_r. For the special angle $\theta = 0°$ the resonance takes place for each value of X when $Y = 1$ i.e $\omega = \omega_{RF} = \omega_c$. In this case the microwave frequency is equal to the Larmor frequency, hence the wave is in resonance with the cyclotron motion of the electrons. This resonance is of primary importance for ECRIS and MDIS and takes the name of **Electron Cyclotron Resonance**. In plasma physics, the extraordinary wave propagating with θ=0 is named **R wave**. For the special angle $\theta = 90°$ the resonance occurs when $X + Y^2 - 1 = 0$ i.e:

$$\omega_{RF} = \omega_{UHR} = \sqrt{\omega_c^2 + \omega_p^2} \tag{2.1.29}$$

This resonance is named **Upper Hybrid Resonance (UHR)**, and the wave propagating exactly across $\vec{B}_0$ ($\theta = 90^\circ$) is named **X wave**.
The resonance condition implies that X and Y parameters lie on a parabola, as shown in figure 2.1.2. At this frequency the electrons are subjected to the cyclotron motion at frequency ω_c and to the plasma oscillation, having frequency ω_p. The combination of the two motions turns the trajectory into ellipses which are covered with resulting frequency $\omega_{UH} = \sqrt{\omega_p^2 + \omega_c^2}$. When $\omega_{RF} = \omega_{UHR}$ the energy of the microwave can be transferred to plasma waves. For a generic angle θ, the resonances of the extraordinary wave are placed in the $X - Y$ plane lying between ECR and UHR. It is important to notice that the resonance curves lie in the plane $X, Y \leq 1$, i.e. when $\omega \leq \omega_c$ and $\omega \leq \omega_p$. Only when the incidence angle is exactly zero the resonance (ECR) can occur even at density larger than the cutoff density. Because this effect is found for just a single value of the angle θ (i.e. it represents a sort of singularity). The existence of an "overdense resonance" can be viewed more like a formal consequence of a mathematical treatment that a real physical process.

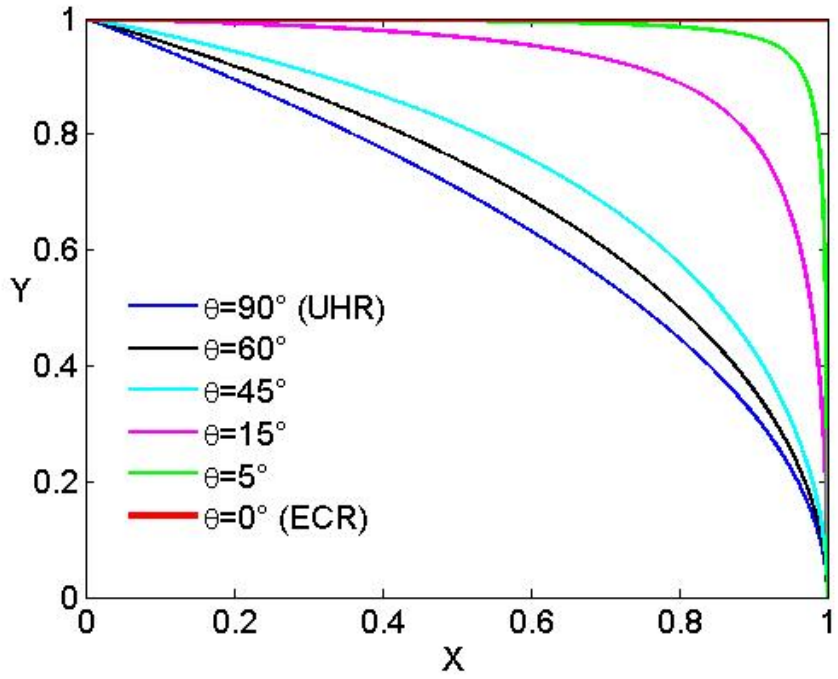

Figure 2.1.2: Corresponding values of X and Y parameters satisfying resonance conditions of the Extraordinary waves propagating for different propagation angles θ.

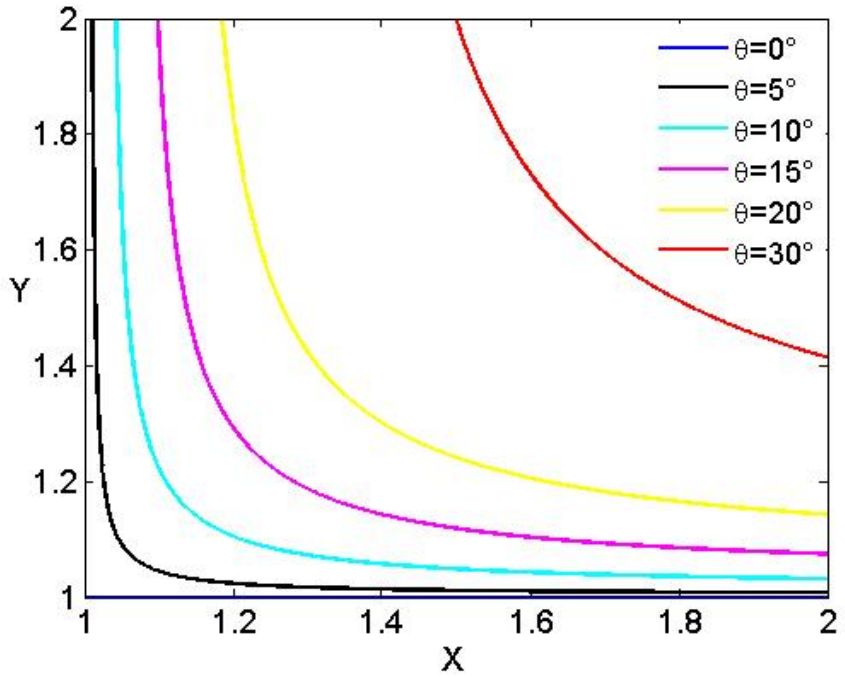

Figure 2.1.3: Resonances of the Ordinary waves propagating for different angle propagation angles θ.

The resonances of the Ordinary waves can be found easily by looking at the zeroes of equation (2.1.24). It is easy to see that these solutions correspond to the ones of equation (2.1.28) placed in the $X, Y \geq 1$ region of the X-Y plane[4], as shown in figure 2.1.3. These resonances, however, are placed in a forbidden region for ordinary waves, i.e. over the O cutoff X=1; therefore such resonances could be reached only by wave tunneling through the O cutoff. In case of incidence angle $\theta = 0^{\circ}$, the ordinary wave is named L wave, and it encounters a resonance for Y=1. When θ increases, hyperbole shaped resonances move toward larger values of X and Y.

As we have seen above, a conventional nomenclature is normally adopted in plasma physics to label waves propagating at certain angles, in particular at 0° and 90°. Ordinary waves propagating along or across the magnetic

[4]In a more general picture, taking into account also ion motion, ordinary wave can be absorbed by ions at Ion Cyclotron Resonance ($\omega_i = \omega_{RF}$), while at the Lower Hybrid Resonance, the wave is submitted to a resonant coupling to electrostatic wave.

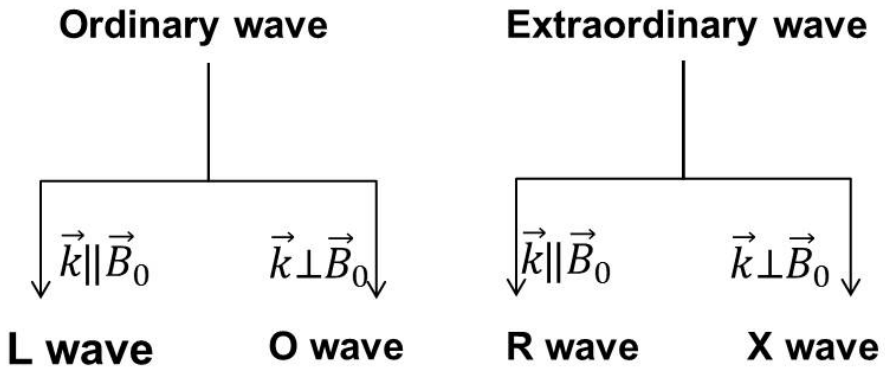

Figure 2.1.4: Scheme of the wave propagation in anisotropic plasmas. According to the mutual orientation of $\vec{k}$, $\vec{E}$ and $\vec{B}$, the last being the magnetostatic field, the waves have different characteristics and are named R, L, O and X [10]. See also figure 2.1.6.

field are respectively named O wave and L waves. As we introduced previously, Extraordinary waves propagating along or across the magnetic field are respectively named R wave and X waves. A scheme of the four type of waves is shown in figure 2.1.4, whereas in table 2.1.5 the respective refraction indexes, obtainable from equation (2.1.24) are displayed. For a more detailed treatment of these issues we refer to the next sections.

refraction index	wave type
$\omega^2 = \omega_p^2 + k^2c^2$	light waves
$\frac{c^2k^2}{\omega^2} = 1 - \frac{\omega_p^2}{\omega^2}$	O wave
$\frac{c^2k^2}{\omega^2} = 1 - \frac{\omega_p^2}{\omega^2}\frac{\omega^2 - \omega_p^2}{\omega^2 - \omega_h^2}$	X wave
$\frac{c^2k^2}{\omega^2} = 1 - \frac{\omega_p^2/\omega^2}{1 - (\omega_c/\omega)}$	R wave
$\frac{c^2k^2}{\omega^2} = 1 - \frac{\omega_p^2/\omega^2}{1 + (\omega_c/\omega)}$	L wave

Figure 2.1.5: Cutoffs and resonances of the waves propagating in a magnetized plasma considering $\theta = 0$, $\theta = 90^\circ$ directions.

It can be useful to study the polarization of the waves in a magnetized plasma. From the middle line of equation (2.1.22) it is possible to calculate the relation between E_x and E_y, that is the polarization in the plane perpendicular to $\vec{B}_0$:

$$\frac{iE_x}{E_y} = \frac{N^2 - S}{D} \tag{2.1.30}$$

From this relation it follows that the waves are linearly polarized at the resonance ($N^2 = \infty \rightarrow E_y = 0$) and circularly polarized at cutoff ($N^2 = 0$, $R = 0$ or $L = 0 \rightarrow E_x \pm E_y$). Furthermore, following [3], it comes out that the ordinary waves are left-hand polarized, whereas extraordinary waves are right-hand polarized. A sketch showing the orientation of the electric field with respect to the magnetostatic field is shown in figure 2.1.6.

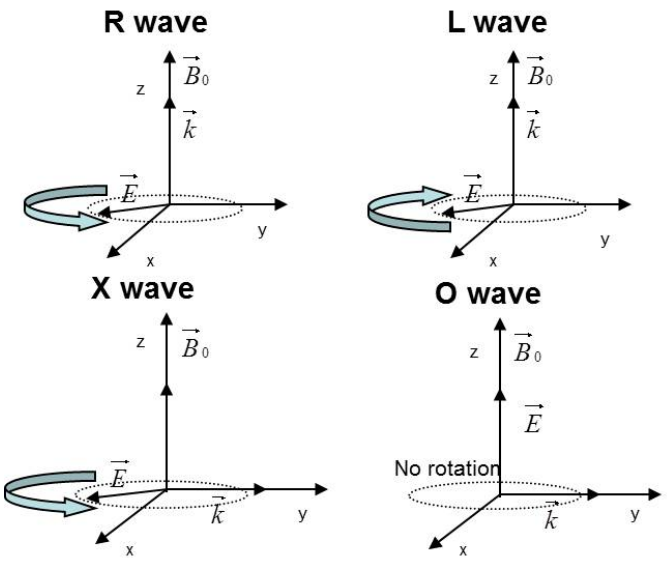

Figure 2.1.6: Diagram showing the possible orientations of the electric field with respect to the magnetostatic field, along with the possible waves polarizations [2].

Because of their polarization, electric field of the R wave rotates in the same direction and versus of the gyrating electrons in a magnetic field. When the frequency of the injected microwave ω_{RF} matches the cyclotron frequency ω_c, then electrons see a constant field leading to resonant energy absorption. If the electrons gain enough energy, they are able to ionize the neutrals of the nascent plasma. It is really important to note that **in a collisionless plasma, the ECR is the only physical mechanism allowing the direct energy transfer from E.M wave to electrons**. The mechanism of the resonant electron acceleration can be easily demonstrated by looking to the solution of the equation of motion (2.1.14) for an harmonic E.M field in a magnetized plasma acting on a free electron:

$$\begin{cases} v_x = \dfrac{e}{m}\dfrac{-i\omega E_x + \omega_c E_{E_y}}{\omega_c^2 - \omega^2} \\ \\ v_y = \dfrac{e}{m}\dfrac{-i\omega E_y + \omega_x E_x}{\omega_c^2 - \omega^2} \\ \\ v_z = \dfrac{eE_z}{-im\omega} \end{cases} \tag{2.1.31}$$

Electron velocity and kinetic energy goes to infinity only when $\omega_c \to \omega$, that is the ECR. ***ECR heating***, is actually the most powerful method to generate and sustain a plasma. In other plasma resonances, in facts, the E.M energy is not directly transferred to electrons, but indeed to plasma oscillation modes that, only in a second time, can transfer their energy to electrons by means of collisions or non-linear effects. Such oscillation modes can be excited by either ordinary or extraordinary waves. Their dispersion relation can be easily found from the resonance condition (2.1.28):

$$\omega^2(\omega^2 - \omega_{UHR}^2) + \omega_c^2\omega_p^2\cos^2\theta = 0 \tag{2.1.32}$$

In a more general picture these oscillation modes are usually called Trivelpiece-Gould (T-G) modes [1], from the name of the scientists which first demonstrated their existence [21]. T-G waves consist in collectives modes of rarefaction and compression of plasma fluid which can occur at zero electron temperature and which can be excited at the resonances of the E.M waves. From equation (2.1.32) it is evident that for a fixed propagation angle, two different waves can exist. The upper branch is excited by the extraordinary wave, while the lower branch is excited from ordinary waves at their respectively resonances. The upper branch behaves like the upper hybrid oscillation, while the lower behaves as a Langmuir wave [1]. In this picture upper hybrid oscillations represent only a particular case of T-G modes: in facts their oscillation frequency can be easily obtained by setting $\theta = 90^\circ$ in equation (2.1.32); in such a way one of the roots vanishes, while the other gives $\omega = \omega_{UHR}$. The dispersion curves of the two branch of the T-E modes are shown in figure 2.1.7, where oscillation frequency is plotted against the wave vector k_z, for $\omega_c > \omega_p$ and for $\omega_c < \omega_p$.

A powerful method to visualize the cutoffs and the resonances of the various modes is to plot them on the so called CMA diagram[5] [30]. This

[5]The CMA diagram takes the name from Clemmow, Mullaly and Allis who proposed the graphical representation of the many cutoffs and resonances of electromagnetic waves

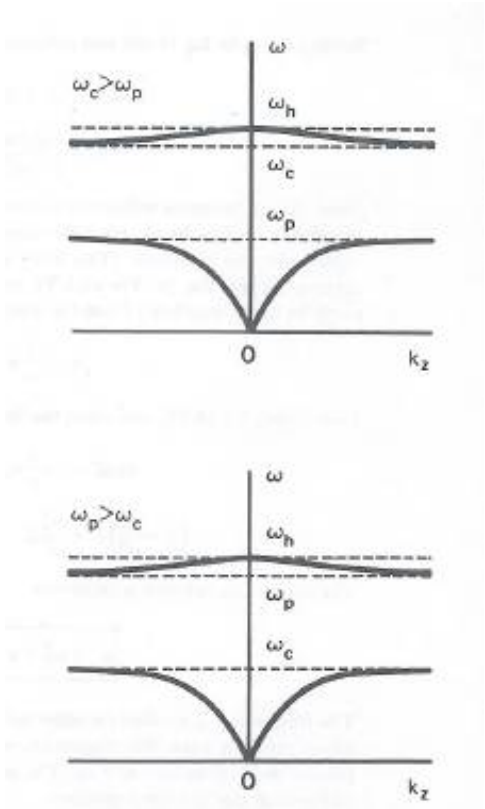

Figure 2.1.7: Trivelpiece-Gould dispersion curves for electrostatic electron waves in a magnetized plasma [21] in $\omega_c > \omega_p$ and $\omega_c < \omega_p$ plasma regions. Since $\tan\theta = k_x/k_z$, $k_z = 0$ corresponds to $\theta = \pi/2$, while $k_z \to \infty$ corresponds to $\theta = 0$

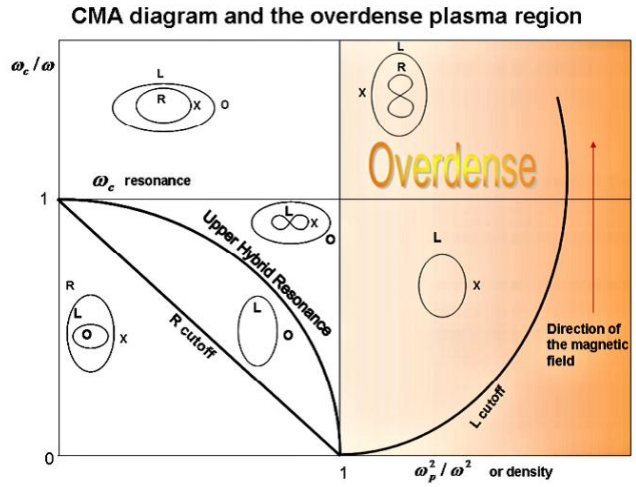

Figure 2.1.8: A detailed view of the Clemmow-Mullaly-Allis diagram showing the region of the so-called overdense plasma, i.e. that region where the plasma density exceeds the cutoff of the ordinary (O) mode.

diagram is reported in figure 2.1.8. The diagram however works only in case of cold plasma approximation. The use of a warm plasma approximation implies a so great number of complications that the diagram cannot be further employed. The diagram can be viewed as a plot of the Y versus X, or equivalently a plot of the magnetic field versus the plasma density (here we remember that $Y = \omega_c/\omega \propto B$ and $X = \omega_p^2/\omega^2 \propto n_e$) . For a given frequency ω, any experimental situation characterized by X and Y is denoted by a point on the graph. The total plane is divided into several zones, and the boundaries of each zone are the cutoffs and the resonances of the main modes mentioned above. The vertical line at $X = 1$ is the O cutoff; it corresponds to the cutoff density in an unmagnetized plasma. Above this value the plasma will be overdense. The small diagrams in each region delimitated by the cutoffs and the resonances (i.e. the eight-shaped or ellipsoidal small diagrams) indicate not only which wave propagates, but also the qualitative variation of the phase velocity with the angle (considering that the magnetic field is directed along the vertical direction).

propagating in a cold plasma.

2.2 ECR and stochastic heating

ECR heating is a very impressive method to heat selectively the electrons in the plasma. If we introduce into a plasma an electromagnetic wave whose frequency is equal to the cyclotron frequency of electrons, an extremely efficient energy transfer will take place. Even if the basic idea underlying ECR heating is rather simple, it is very difficult to obtain a quantitative description. The main issue concerns the non-deterministic acceleration, that is strongly dependent on the phase difference between the electron cyclotron motion and and the right-hand circularly polarized component of the E.M field. If the phase difference is zero, the electron will be accelerated, but if the phase different is π the electron will be decelerated. Hence, to obtain the temporal evolution of the hot-electron component, one has to calculate the motion of individual electrons crossing the ECR region, averaging over many individual phase differences. In this case, the methods leads to a kind of "**stochastic heating**" due to multiple passages through the ECR [2]. It was demonstrated [2] that, when averaging over a random phase angle, the energy gain is positive and proportional to the wave energy density $|\tilde{E}|^2$ and to the time spent in the resonant region. In section 1.2 an apparent contradiction came out: even collisionless electrons have a temperature and their energies distribute along a Maxwellian distribution. This may appear to be unreasonable, because if electrons do not collide each other, they can not randomize their momenta. In facts, an electron population accelerated by ECR gains only kinetic energy, but its temperature would remain low. It is evident that other mechanisms must be invoked to explain the effective heating, and the stochastic heating mechanism in collisionless plasma may be a solution to the problem. An electron moving in the plasma with velocity v_e equal to the wave phase velocity v_ϕ can be trapped by the wave potential. Let us consider a frame moving with the wave velocity: particles moving with a similar velocity can oscillate into the wave potential $\phi(z)$. Because of the energy conservation we can write the relation linking v_e to $\phi(z)$:

$$\frac{1}{2}mv_e^2 + e\phi(z) = E = const \tag{2.2.1}$$

Then v_e is:

$$v_e = \pm\sqrt{\frac{2}{m}\left(E - e\phi(z)\right)} \tag{2.2.2}$$

Such equation represents a mechanical oscillator with small amplitude oscillations around equilibrium. As long as the perturbation is small enough,

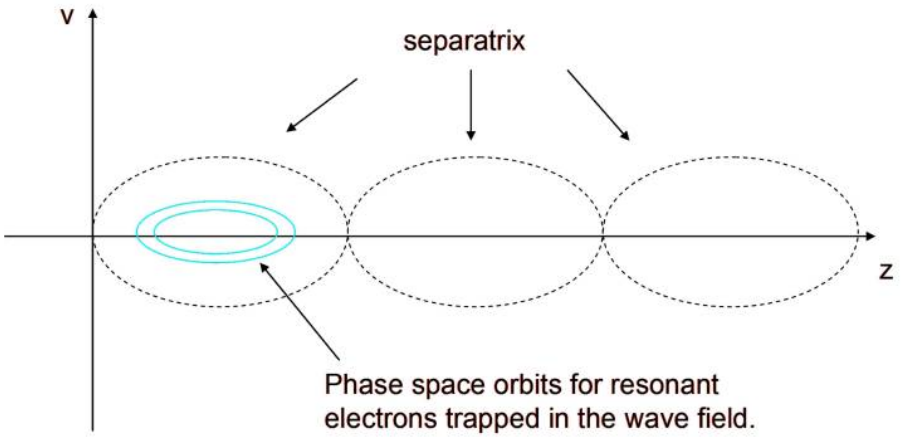

Figure 2.2.1: separatrix in the phase space. The electrons trapped by the wave in resonant conditions are also shown.

the motion around the minimum will be harmonic and the electron is resonantly trapped by the potential of the wave. In the phase space, these motions are represented as ellipsoidal closed trajectories, named "separatrix". To higher electron velocities bigger ellipsoidal trajectories in the phase space correspond. However, if the electron energy becomes appreciable with respect to $\phi(z)$, the motion is no longer harmonic and non-linear effects arise. If the electron stays on the top of the $\phi(z)$ potential, then the electron velocity will be zero according to the equation (2.2.2). In this case the electron has the same velocity of the wave, but as it stays on top of the wave potential, its equilibrium is not stable, and chaotic motions may arise. When this condition is satisfied the phase space separates in different zones. Inside each zone the particle is trapped by the wave. The figure 2.2.2 features the separatrices of a sinusoidal wave interacting with a single particle. This theory, named **pendulum model**, explains easily how the non linearity and the stochastic effects can play a fundamental role in collisionless wave-particle interaction. Such interaction affects only the particle moving with velocity similar to that of the wave. Electrons whose velocity differ considerably from the wave phase velocity are not trapped and their velocity is only slightly perturbed by the wave.

In the easier case of Simple Mirror configuration, the equation describing the positioning of the particle along the z axis is:

$$z = z_0 cos(\omega_b t + \psi_0) \tag{2.2.3}$$

where ω_b is the bouncing frequency between the two inversion points in a simple mirror magnetic trap, introduced in section 1.6, and ψ_0 is the initial phase. The perpendicular component of the wave electric field, felt by the electron during its bouncing motion depends on the time t, on the coordinates of the position in the magnetic trap, z and r, and on the initial phase $\theta_\perp$ of the field component. In the Simple Mirror case, it can be written as:

$$E_\perp = E_{\perp 0} cos(\omega_{RF} t - kz + \theta_\perp) \tag{2.2.4}$$

Taking into account equation (2.2.3), previous equation becomes:

$$E_\perp = E_{\perp 0} cos(\omega_{RF} t - k z_0 cos(\omega_b t + \psi_0) + \theta_\perp) = \sum_n A e^{i[(\omega - \omega_c)t + \theta_\perp + \theta_b]} \tag{2.2.5}$$

where:

$$\theta_b = \omega_b t + \psi_0 \tag{2.2.6}$$

Then the equation (2.2.5) takes into account the cyclotron frequency, the frequency of the wave and the bouncing frequency. The Fourier expansion puts in evidence that the composition of the bounce and cyclotron frequencies leads to an effective multi-waves interaction: i.e. we may imagine the single particle interacting with a couple of waves at the resonance. Then each wave-particle interaction has a proper separatrix and many zones like those shown in figure 2.2.2 are present in the phase space. The figure shows the structure of the several separatrices in the phase space in proximity of the ECR zone. It is clear that all the separatrices are overlapped in $p_\perp$, being the distance between them proportional to ω_b. In addition, if the electron motion initially occur in one of the separatrix, the motion can evolve into the several separatrices in a complicated manner, according to the electron kinetic energy and phase and to non-linearities in the wave-particle interactions.

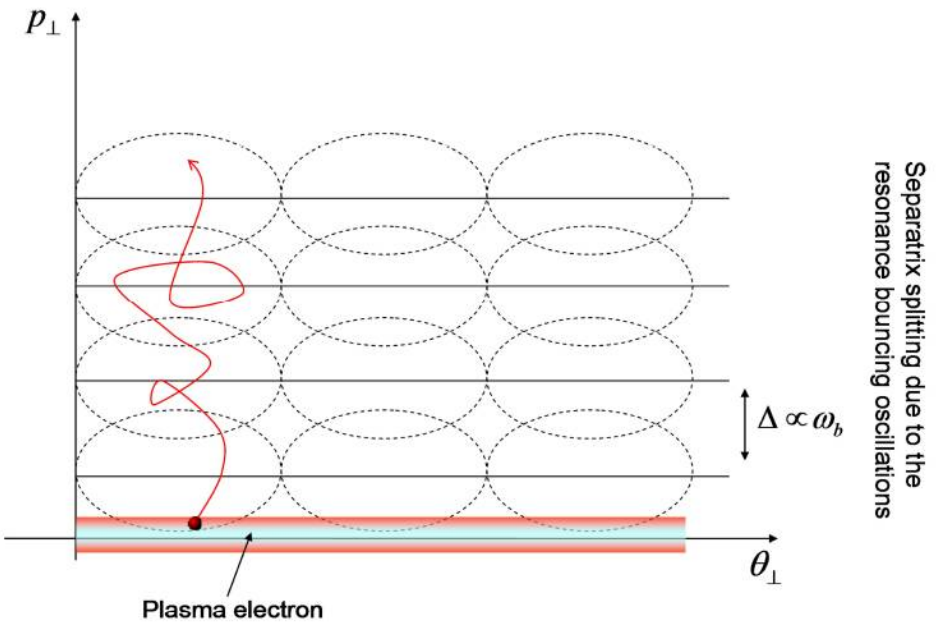

Figure 2.2.2: separatrices in the phase space. The electrons trapped by the wave in resonant conditions are also shown.

Because of the separatrices overlapping, the electron perpendicular momentum (then its energy) will increase more and more passing from a separatrix to the subsequent one, as schematically shown in figure. In the real situation the horizontal separatrix extension at the resonance is spatially limited, then the electron will escape after a fixed time from the interaction zone. But because of its bouncing motion, it will pass again through the resonance. As the former interaction was regulated by a stochastic motion in the phase space, it will arrive again to the ECR with a completely random phase, thus being able to gain more energy. This process goes on for many passages through the resonance. However, the higher is the electron energy, the higher is the perpendicular component of the velocity $v_\perp$ and then ω_b (see equation 1.6.11). When the bouncing frequency becomes comparable with the Larmor frequency, then the separatrices split, and the electron cannot pass through. Electron heating stops because the phase randomization process, strictly connected to the separatrix overlapping, does not work anymore. Such a mechanism can be seen also by another point of view.

When the bouncing frequency is comparable with the Larmor one, electrons interact with resonance region with a well-defined phase, i.e. the motion of the electron in phase space become periodic in time and the interaction of a very fast electrons with the resonance zone is no longer stochastic. In such conditions heating can not continue.

2.3 Collisional absorption

In the previous sections we have analyzed the propagation and absorption of the E.M waves in collisionless approximation. This is valid for the largest part of ion sources, like the ECRIS, in which collision frequency is so low that collisional effects can be neglected. Such an approximation is only partially valid in other ion sources, working at higher neutral pressure and lower electron temperature, like MDIS. In such a case a new plasma heating mechanism must be taken into account, called **collisional absorption**. The mathematical treatment of the collisional case is totally similar to the collisionless one. Equation (2.1.14) becomes:

$$m_e \frac{\partial \vec{v}}{\partial t} = e\left(\vec{E} + \vec{v}_s \times \vec{B}\right) - m_e \omega_{eff} v \tag{2.3.1}$$

where ω_{eff} is the collision frequency multiplied by 2π. How it is evident, collisions play the role of a frictional term. From the equation of motion, it is then possible to write the dispersion relation in presence of collisions, which represents the generalization of equation (2.1.24):

$$N^2_{o,x}(\theta) = 1 - \frac{2X(1+iZ-X)}{2(1+iZ)(1-X) - Y^2\sin^2\theta \pm \Gamma} \tag{2.3.2}$$

Γ being:

$$\sqrt{Y^4\sin^4\theta + 4Y^2(1+iZ-X)^2\cos^2\theta} \tag{2.3.3}$$

Where Z is:

$$Z = \frac{\omega_{eff}}{\omega} \tag{2.3.4}$$

A detailed treatment of wave propagation in presence of collision is beyond the scopes of the present work, so we will limit to the main conclusions. The imaginary term in equation (2.3.2) indicates the presence of an absorption term in the dispersion relation. To clarify this aspect, it is sufficient to remember that in a plasma the electric field is carried by the oscillating electrons. If electrons do not collide during oscillation, the wave is transmitted, but if a collision occurs, part of the wave energy is transferred to the medium, leading to the attenuation of the wave. Collisions limit also the energies achievable in ECR heating: in facts for each collision occurring during acceleration, the electron loses part of its own energy. Hereinafter we will limit our consideration to slightly collisional plasmas, like the ones generated by MDIS sources (ν_{ee} lies between 10^5 and $10^6 Hz$) and then

$Z = 1 \cdot 10^{-3} \div 1 \cdot 10^{-4}$. Collision frequency is low enough to allow E.M wave propagation and ECR heating, but large enough to affect the plasma eigenmodes. The energy transmitted to the upper hybrid and T-P oscillation modes at the wave resonances can now be transferred to electrons by means of the electron collisions, enabling an heating method different for ECR, but much more efficient.

2.4 The warm plasma approximation

The validity of the cold plasma approximation gets lost in proximity of the cut-off where the refractive index goes to zero. Here the wavelength is no longer negligible in comparison with the scale length of the relevant plasma parameters [27]. In the case of a resonance, where the refractive index becomes infinite, the cold plasma approximation breaks down, if the wavelength reaches the size of the electron gyro (Larmor) radius. Here the so-called finite Larmor radius effects have to be taken into account. Let us therefore introduce the finite Larmor parameter $\mu = (1/2)k_\perp^2 v_{th}^2/\omega_c^2$. Here $k_\perp$ represents the wave vector in any direction perpendicular to the magnetic field. We could choose the magnetic field pointing in the z-direction, without losing the generality. We assume a Maxwellian velocity distribution function and neglect relativistic effects. Finally we express the frequency distance from the n^{th} cyclotron harmonic resonance in Doppler shift units as:

$$\zeta_n = (\omega + n\omega_c)/(|k_z|v_{th}^2) \tag{2.4.1}$$

k_z represents the wave vector components in the z-direction. The dielectric tensor can be rewritten as [30]:

$$\bar{\bar{\epsilon}}_r = \bar{\bar{I}} + \frac{\omega_p^2}{\omega^2} \sum_{n=-\infty}^{n=\infty} \begin{bmatrix} \epsilon_{xx} & \epsilon_{xy} & \epsilon_{xz} \\ \epsilon_{yx} & \epsilon_{yy} & \epsilon_{yz} \\ \epsilon_{zx} & \epsilon_{zy} & \epsilon_{zz} \end{bmatrix} \tag{2.4.2}$$

where:

$$\begin{aligned} &\epsilon_{xx} = \tfrac{n^2}{\mu}\tilde{I}_n Z_n \qquad \epsilon_{xy} = -\epsilon_{yx} = in\tilde{I}'_n Z_n \\ &\epsilon_{xz} = \epsilon_{zx} = -n\sqrt{\tfrac{2}{\mu}}\tilde{I}_n(1+\zeta_n Z_n) \qquad \epsilon_{yy} = \left(\tfrac{n^2}{\mu}\tilde{I}_n - 2\mu\tilde{I}'_n\right) Z_n \\ &\epsilon_{yz} = -\epsilon_{zy} = i\sqrt{2\mu}\tilde{I}_n(1+\zeta_n Z_n) \qquad \epsilon_{zz} = 2\zeta_n\tilde{I}_n(1+\zeta_n Z_n) \end{aligned} \tag{2.4.3}$$

Here the abbreviations $Z_n = Z(\zeta_n)$ and $\tilde{I}_n = e^{-\mu}I_n(\mu)$ are used, where I_n

is the n^{th} order modified Bessel function and Z is the plasma dispersion function [1]

$$Z(\zeta_j) = \frac{1}{\sqrt{\pi}} \int_{-\infty}^{\infty} \frac{e^{-s^2}}{s - \zeta_j} ds \tag{2.4.4}$$

The so-called *hot dielectric tensor* expresses several new features for the wave propagation in comparison with the cold dielectric tensor. Now, the dielectric tensor is a function of not only ω_c and ω_p but also a the temperature and the wave vector $\vec{k}$. This leads to a new kind of solutions of the dispersion relation, the electrostatic modes. It is useful to verify if E. M. wave resonance mechanism is modified when warm plasma approach is taking into account. The treatment used in section 2.1.3, in facts, is valid everywhere except for the resonances proximity, when wave phase velocity becomes comparable with thermal velocity. Solving (2.1.14) in the case of R wave propagation and taking into account for sake of simplicity only the motion along x direction, one obtain [1]:

$$\ddot{x} + \omega_c^2 x = \frac{1}{m} E_x e^{i(kx - \omega t)} \tag{2.4.5}$$

if kr_L is not small the exponent strongly varies from one side of the orbit to the other and it can not be considered as a constant during the electron cyclotron motion. kx can be approximated as $x = r_L \sin \omega_c t$

the solution of the motion equation is than:

$$v_x = -\frac{e}{m} i E_x \sum_{-\infty}^{\infty} \omega - n\omega_c \frac{J_n(kr_L)\, e^{-i(\omega - n\omega_c)t}}{\omega_c^2 - (\omega - n\omega_c)^2} \tag{2.4.6}$$

V_x goes to infinity, i.e. the R wave has a resonance, not only at the ECR deduced by the cold plasma approximation, but also at the multiples of ω_c.

2.5 Electrostatic waves

Generally an electrostatic field $\vec{E}$ is defined as a field with no time dependence. How it is know an electrostatic fields $\vec{E}$ can be derived from a scalar potential V ($\vec{E} = -\vec{\nabla}\mathrm{V}$) and hence obey $\vec{\nabla} \times \vec{E} = 0$. The latter condition is sometimes considered to be a requirement for electrostatic fields. But it shows, however, that there can exist time-dependent electric fields for which $\vec{E} = -\vec{\nabla}V$, which have been given the name "**electrostatic waves**" [28]. Sufficient condition to have $\vec{\nabla} \times \vec{E} = 0$ in a time-dependent electric field

$\vec{E} = \vec{E}_0 e^{i(\vec{k}\cdot\vec{r}-\omega t)}$ is that $\vec{k} \parallel \vec{E}$, i.e. the electric field must be a "longitudinal wave". In facts, if the electric field $\vec{E}$ parallel to the wave vector $\vec{k}$:

$$\vec{\nabla} \times \vec{E} = \vec{k} \times \vec{E} = 0 \tag{2.5.1}$$

As for all electrostatic field, a consequence of equation (2.5.1) is that $\frac{\partial B}{\partial t} = 0$. i.e such waves do not have an associate magnetic field. A longitudinal electric wave can only exist in a medium that can support a nonzero polarization density $\vec{P}$ (volume density of electric dipole moments). In facts, to generate the time-dependent electric field is necessary to separate ions from electrons, generating electric dipoles. The polarization density implies an effective charge density ρ given by:

$$\rho = -\vec{\nabla} \cdot \vec{P} \tag{2.5.2}$$

Which is consistent with the first Maxwell equation only if $\vec{P} = -\vec{E}$. In this case the electric displacement $\vec{D}$ of the longitudinal wave vanishes:

$$\vec{D} = \vec{E} + \vec{P} = 0 \tag{2.5.3}$$

The only medium in which this can happen is a the plasma. Equation (2.5.3) will have a large importance in the following, it represents a necessary condition to have longitudinal wave, which can be found by imposing to the electromagnetic system the simple condition $\vec{D} = 0$

2.5.1 Langmuir waves and ion-acoustic waves

The simplest ES modes which can be found from a warm plasma approximation are the plasma oscillations, also named *Langmuir waves*[6]. In a unmagnetized plasma, Langmuir waves represents the main electrostatic mode together with the ion-acoustic mode. In a magnetized plasma further ES modes arise, as will be shown in the following. When the plasma electrons are displaced from the uniform ion background, an electric field builds up to restore the neutrality of the plasma, by pulling the electrons back to their original positions. Because of their inertia, the electrons will overshoot and oscillate around their equilibrium position with frequency equal to the previously defined plasma frequency ω_p. The dispersion relation of Langmuir waves can be easily found from equation (1.3.9) by assuming a perturbation potential. Without entering the mathematical details one finds [1]:

[6] From Ingmuir Langmuir, who discovered plasma oscillations in the 1920s.

$$\omega_l^2 = \omega_p^2 + \frac{3}{2}k^2 v_{th}^2 \tag{2.5.4}$$

the electron oscillation is so fast that the massive ions do not have time to respond to the oscillating filed and may be considered as fixed. Typical values of ω_l are in the order of some GHz.
In a similar way, ions can be involved in oscillations called *ion-acoustic waves*[7]. Since the motion of massive ions will be involved, these will be low-frequency oscillations. From the fluid equation for the ion species, the ion waves dispersion relation can be found [1]:

$$\frac{\omega_i}{k} = \left(\frac{kT_e + 3kT_i}{M}\right)^{\frac{1}{2}} \equiv v_s \tag{2.5.5}$$

Plasma oscillations are basically constant-frequency waves, with correction due to thermal motions. Ion waves are basically constant-waves and exist *only* when there are thermal motion. typical values of ω_i are in the order of $1 - 100MHz$.

2.5.2 Bernstein waves

Electron Bernstein Waves[29] (EBW) represents a generalization of Langmuir waves in a magnetized plasma. Similarly to the other ES waves, they can exist only in warm plasma, when finite electron temperature is taken into account. When a static magnetic field is superimposed onto the oscillating electric field associated with the plasma wave, the electron orbits become ellipses. On increasing further the magnetic field, the Lorentz force dominates over the electrostatic one and the orbits take a circular form [32] (figure 2.5.1). The EBW occurs when the electron gyrophase is organized in such a way that the space charge distribution has maxima and minima, which are periodically distributed perpendicularly to external magnetic field lines [27]. The gyrophases are no longer random as they were before the impinging of the wave, but they are organized depending on the gyrocenter position. As shown in figure 2.5.2, periodic charge accumulations propagate in the direction of the wave vector with wavelength of the order of four times the electron gyro radius.

The dispersion relation of EBW can be found from equation (2.5.3), which can be written as:

[7] Ions form regions of compressions and rarefaction, just as in ordinary sound waves. Furthermore the dispersion relation is similar to that of sound waves in a fluid.

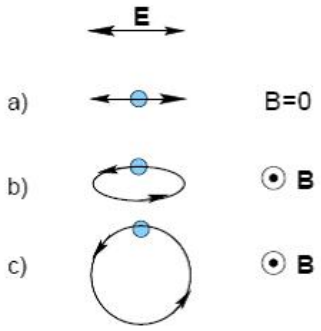

Figure 2.5.1: Electron orbit in a) Langmuir plasma wave, b) upper hybrid oscillation, c) EBW.

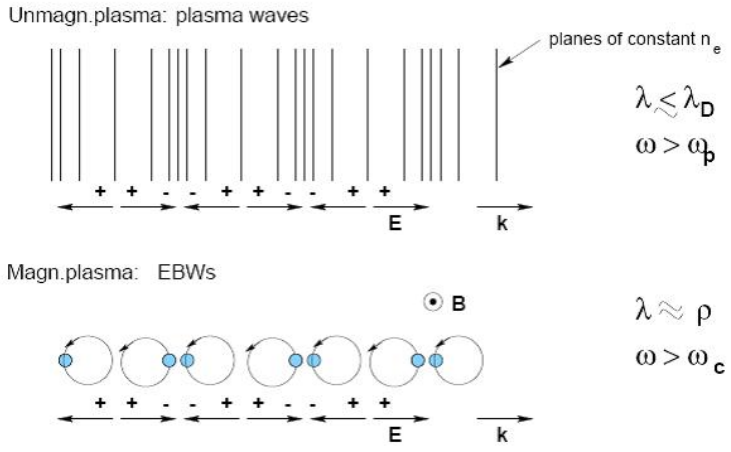

Figure 2.5.2: Electron gyration can create charge accumulation and rarefaction just like Langmuir plasma waves do in unmagnetized plasmas.

$$\vec{D} = \epsilon_0 \bar{\bar{\epsilon}}_r \cdot \vec{E} = 0 \tag{2.5.6}$$

Where $\bar{\bar{\epsilon}}_r$ is the hot dielectric tensor introduced in equation (2.4.2). This equation system admit a non zero solution only if:

$$det\,|\bar{\bar{\epsilon}}_r| = 0. \tag{2.5.7}$$

For sake of simplicity the entire calculation of the determinant will be neglected, and only the conclusions will be treated. Assuming electrostatic perturbation such that $\vec{E} = \vec{\nabla}\phi$ and considering waves varying in space ant time as $\phi = \phi_0 e^{i(\vec{k}\cdot\vec{r}-\omega t)}$, equation 2.5.7 reduces to:

$$k_x^2\epsilon_{xx} + 2k_x k_z \epsilon_{xz} + k_z^2\epsilon_{zz} = 0 \tag{2.5.8}$$

Here, without loss of generality, $\vec{k}$ was chosen lying in the $x-z$ plane, so that $k_y = 0$. Solving in short wavelength approximation and looking for the solution in which $\vec{k} \parallel \vec{E}$ one obtains the dispersion relation for this so-called electrostatic approximation [27]:

$$\frac{k_\perp^2}{2\omega_p^2/v_{th}^2} = 2\omega_c^2 \sum_{n=1}^{\infty} n^2 \frac{e^{-b} I_n(b)}{\omega_{RF}^2 - n^2\omega_c^2} \tag{2.5.9}$$

Figure 5.1.15 shows the dependence of the wave vector $k \perp r_L$ on the ratio ω/ω_c for different values of ω_p^2/ω_c^2 [31]. $k \perp r_L$ goes from zero to infinity in the gap between cyclotron harmonics. At each cyclotron harmonic the wave vector (and consequently the refraction index) becomes infinite and therefore here EBW have a resonance, corresponding to the zeroes of denominator of equation (2.5.9):

$$\omega_{RF}^2 = n^2\omega_c^2 \rightarrow B_{res} = \frac{1}{n} B_{ECR} \quad n = 1, 2, ..., \infty \tag{2.5.10}$$

Thus EBW are absorbed at the harmonics of ω_c, which means that in a ion source like ECRIS or MDIS, EBW absorption is possible for the same can occur at the harmonics of the resonance magnetic field B_{ECR}. Hereinafter we will define ω_c as fundamental harmonic, $\omega = \omega_c/2$ will be the first harmonic, $\omega = \omega_c/2$ will be the second harmonic and so on. Even if EBW electric field is perpendicular to the magnetostatic field, EBW can not be able to arise a $\vec{E} \times \vec{B}$ drift (see section 1.4.1 for reference), in facts since the wave frequency is larger than the cyclotron frequency ($\omega_{EBW} \geq \omega_c$) and thus the average electric field will cancel during the gyromotion. Because of their electrostatic nature, the Bernstein waves cannot propagate outside

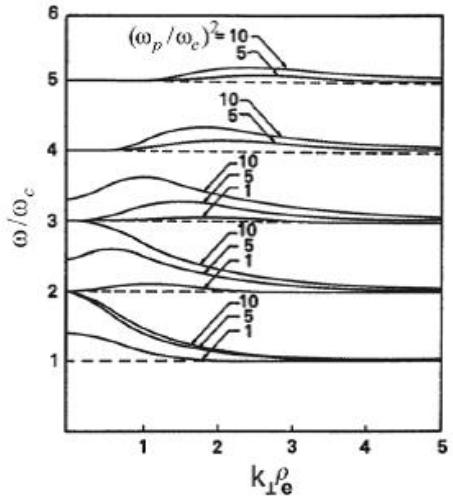

Figure 2.5.3: Dispersion relation of EBW[31]. Here the frequency is normalized by the cyclotron frequency ω_c and the wave vector is normalized by the thermal electron gyro radius.

the plasma, and their boundary is constituted by the UHR layer[27], where EBWs are strongly coupled with extraordinary waves.

One of the most important properties of EBW is that they can propagate in overdense plasmas without any cutoff [33], as shown in figure 2.5.4. This property of EBW is am important step forward with respect to the E.M waves, which are reflected at the cutoff frequency ω_p. EBW does not suffer this cutoff and could be able to sustain the plasma at electron density much larger than the ones obtainable by means of the usual ECR heating. Figure 2.5.5 shows the regions, in the CMA diagram, where the EBW can propagate. At WEGA stellarator of Greifswald, for example, EBW heating has been used to reach densities up to 10 n_{cutoff}[34],[35]. EBW heating thus, could be a valid alternative to the ECR heating. EBWs, like all the ES waves, can not exist outside the plasma, and they have to be generated inside the plasma. The warm plasma theory allows to verify that near the UHR the X and EBW-modes coincide; the X-wave is coupled into an EBW and vice versa. This phenomenon is called modal conversion and will detailed treated in the following section.

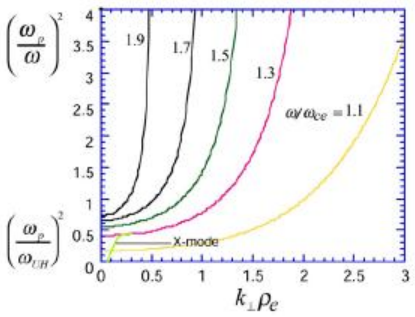

Figure 2.5.4: Density dependence of the EBW dispersion relation for the electrostatic approximation between the first and second harmonic resonances. EBWs show no upper density limit but can be excited at densities above the upper hybrid resonance only [27].

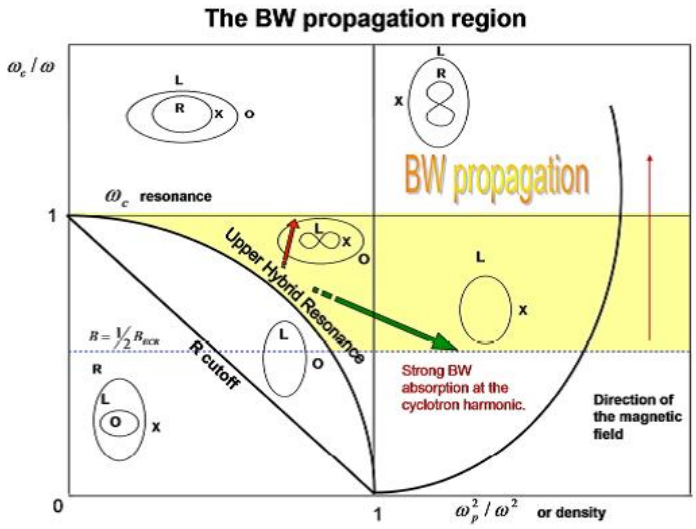

Figure 2.5.5: Representation on the CMA diagram of the region of possible propagation for the Bernstein waves.

2.6 Modal conversion

If we could compare the different electromagnetic and ES modes during their propagation in plasma, we would see that, point by point, they have generally polarization and wave vector very different one from the other. For particular values of plasma parameters, however, it can occurs that the two waves assume the same identical characteristics and they are no more distinguishable. In that particular point, they are the same wave and a mode can convert in the other one. This mechanism enables us to couple the two E.M modes, i.e the ordinary to the extraordinary mode or to couple the E.M waves to the electrostatic ones. The OX conversion is largely used in fusion plasma for allowing the injection of a X mode by means on an antenna from the region external to the plasma. The X mode could not propagate toward the inner plasma because it is reflected at the R cutoff. On the contrary o mode does not suffer R cutoff and can propagate to the core of the plasma where is converted in the X mode [35]. Modal conversion takes place when $N_X = N_Y$. This condition can be verified only if a the O cutoff The propagation angle w.r to the magnetic field θ is null. In facts, by setting $theta = 0$ and X=1 in equation (2.1.24), we have [32]:

$$N_X = N_Y = \sqrt{\frac{Y}{1+Y}} \tag{2.6.1}$$

Extraordinary wave may couple to the the ES waves at the resonances. In particular R waves may convert in Langmuir waves at the ECR[26] whereas X waves may convert to Bernstein waves at UHR[27]. A sketch of the main modal conversion mechanism is shown in figure 2.6.1.

2.6.1 X-B conversion

EBW are excited via the modal conversion of the extraordinary wave at the UHR. When microwave are injected from the vacuum, it may occur that during the propagation in plasma, extr. wave encounters the R cutoff, being totally or partially reflected before reaching the UHR. This means that UHR can be reached essentially by means of the following three mechanisms [27]:

- **High field side launch**; High field side launch is possible when the magnetic field in the extraction region is larger than the resonance magnetic field, i.e. $B/B_{ECR} = Y > 1$. if such a condition is valid, the X wave is not screened by the R-cutoff, but UHR can be reached by crossing the ECR from the high field side. The X waves approach the

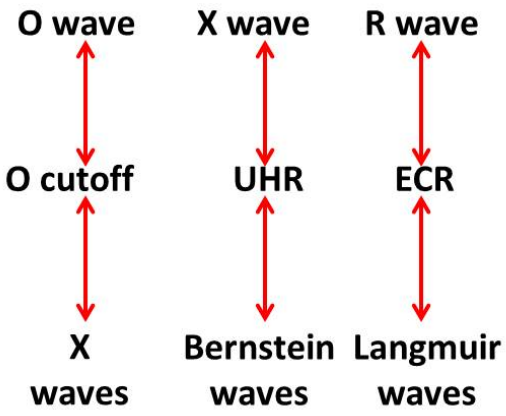

Figure 2.6.1: Representation on the the main mechanism of modal conversion occurring in a ECR plasma.

upper hybrid resonance (UHR) where they are converted into EBWs. Once the density is above the left-hand cutoff (L-cutoff) no X-wave propagation is possible anymore. This means that the electron density between injection and absorption must maintain lower than the L cutoff one. This scheme have been largely experimented in fusion plasma physics, in particular in tokamak[38] and stellarator [39]. This approach could be useful in case of experiment concerning the generation of EBW in ECRIS. In such devices in facts, as it will be shown in the next chapter, microwave injection takes place for $Y > 1$ and $X < 1$.

- **directed X-B conversion**; Another method to excite EBWs is to launch an X-wave from the vacuum into a plasma, which has a steep density gradient with a density scale length of the order of the vacuum wave length of the incident wave. The fast X-mode tunnels through the evanescent region between the R-wave cut-off and the UHR and couples to the slow X-mode which, in turn, mode converts to EBWs at the UHR. Experiments on this mode conversion scheme have been performed at the CDU-X [41] and NSTX [42] tokamaks and at the MST reversed pinch [43].

- **O-X-B conversion**; In such a case the R cutoff is crossed by the O

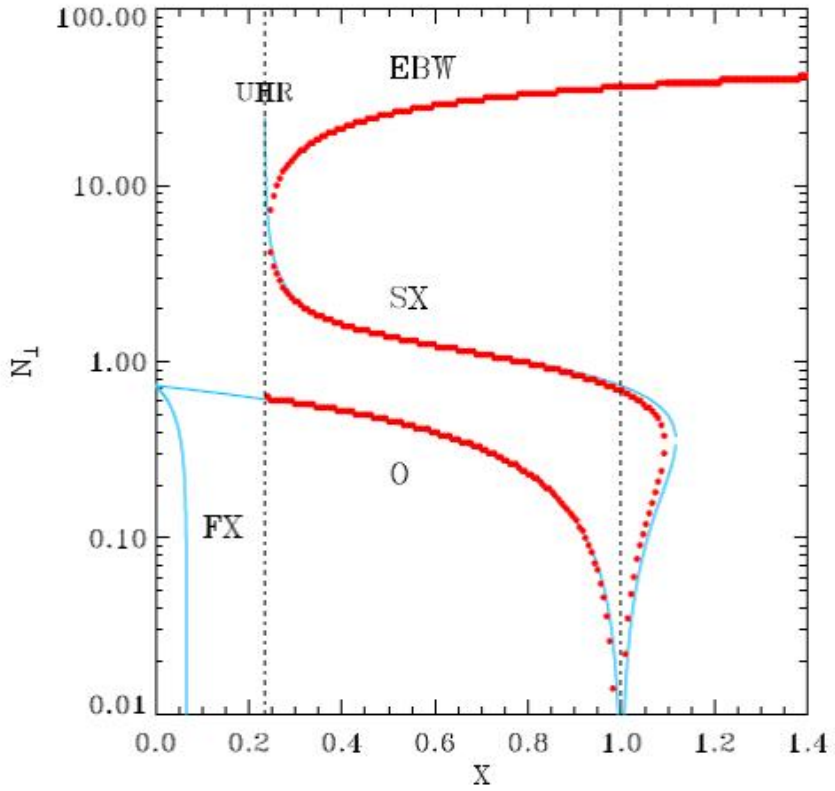

Figure 2.6.2: Hot plasma dispersion relation for oblique propagation at optimal angle, showing OXB mode conversion (points). T_e = 500eV , Y=0.9. Cold plasma dispersion relation also plotted for comparison (line) [32].

wave that, if the conditions for O-X conversion expressed in equation (2.6.1) are valid at the O cutoff, is converted in X wave which can be afterwards converted in Bernstein wave at UHR. This scheme was proposed for the first time by Preinhealter [44]. In figure 2.6.2 O-X-B mode conversion is shown by means of an Hot plasma dispersion relation for oblique propagation at optimal angle.

These schemes have been largely studied for the application in fusion devices [27]. In ECRIS and MDIS devices it is difficult to inject only one type of wave. Plasma chamber, in facts, is a resonator and practically all propagation modes coexist. So it is very difficult to define which mechanism

allowed extraordinary waves to reach UHR. If the UHR layer is enclosed by R and L cutoffs, the X wave can be reflected back and forth passing through the UHR. This is the best condition for the establishment of the Budden-type conversion scenario (i.e.a resonator containing mode conversion to EBW as an effective dissipation is formed). Starting from the Budden tunneling problem, the conversion efficiency can be calculated by means of the following expression:

$$C_{XB} = 4e^{-\pi\eta}\left(1 - e^{-\pi\eta}\right)\cos^2\left(\frac{\phi}{2} + \theta\right) \tag{2.6.2}$$

where ϕ represent the phase difference between the slow X mode propagating towards the L cutoff and the reflected component propagating towards the UHR, whereas θ is the phase of of the gamma function $\Gamma(-i\eta/2)$. The phase factors result from the phasing of the waves in the cavity created by the R and L cutoffs and are also functions of L_n[8]. η is the Budden parameter [40] which is obtained by expanding the wave potential around the UHR to find the position of the R cutoff. This procedure leads to:

$$\eta = \frac{\omega_c L_n}{c}\frac{\alpha}{\sqrt{\alpha^2 + 2\frac{L_n}{L_B}}}\left[\frac{\sqrt{1+\alpha} - 1}{\alpha^2\frac{L_n}{L_B}\sqrt{1+\alpha}}\right]^{\frac{1}{2}} \tag{2.6.3}$$

α represents the ratio between plasma density and cyclotron frequency at UHR:

$$\alpha = \left|\frac{\omega_p}{\omega_c}\right|_{UHR} \tag{2.6.4}$$

L_B and L_n are respectively the the magnetic field and of the electron density scale-length:

$$L_B = \frac{B}{\frac{\partial B}{\partial x}} \qquad L_n = \frac{n_e}{\frac{\partial n_e}{\partial x}} \tag{2.6.5}$$

In the case that $L_B \gg L_n$, and approximating $\alpha \approx 1$, equation (2.6.3) can be written as:

$$\eta \approx \frac{1}{2}\left[\frac{\omega_c L_n}{c}\right] \approx 294\left|BL_n\right|_{UHR} \tag{2.6.6}$$

[8] An exhaustive treatment of the phase factor of equation (5.1.2) con be found in reference [37] and [40]. In this work we will limit to the study of the phase independent factor.

From equation 5.1.2 it is clear that the maximum possible power mode conversion, $C = 1$, is obtained if, simultaneously, $(\phi/2 + \theta)$ is any integer multiple of π and $e^{-\pi\eta} = 0.5$, i.e., $\eta = 0.22$. For this value of η, from equation (2.6.6) we find that optimal condition to have X-B conversion is:

$$|BL_n|_{UHR} = 5.8 \cdot 10^{-4} \quad T \cdot m \tag{2.6.7}$$

This result leads to the optimal value of L_n in MDIS ($B \approx 0.05 \quad T$ at UHR)

$$|L_n|_{UHR} \approx 1cm \quad \rightarrow \quad \left|\frac{\partial n_e}{\partial x}\right|_{UHR} \approx 100\,|n_e|_{UHR} \tag{2.6.8}$$

A similar treatment for ECRIS ($B_{UHR} \approx 0.5T$) leads to $L_n = 10cm$. Therefore, for typical magnetostatic field used in ECRIS, and in particular in MDIS, a steep density gradient is required for an optimal X-B conversion. Similar values, in MDIS, can be found in proximity of the walls of the plasma chamber, where electron density grows from zero to values of about $10^{17}m^{-3}$. Even in ECRIS such density gradients can exist in a thin layer surrounding the ECR region.

2.6.2 Parametric decay

A full-wave analysis of the mode conversion between an electromagnetic wave X-type and electrostatic Bernstein wave allows the identification of non-linear mechanisms that occur during the conversion modal X-B. Through this type of instability, the extraordinary wave, in the vicinity of the resonance UHR, is able to convey part of its energy to the plasma oscillation modes of nature absolutely different, such as ion waves and Bernstein waves. The X wave has normally a longitudinal component of the electric field (TM mode). Starting from equation (2.1.22), in facts, it easy to shown that an X wave propagating along the x axis, can be written as it follows:

$$\left(\omega^2 - \omega_{UHR}^2\right) E_x + i\frac{\omega_p^2 \omega_c}{\omega} E_y = 0 \tag{2.6.9}$$

Approaching UHR $\omega^2 - \omega_{UHR}^2 \rightarrow 0$ and then $E_y = 0$. The only remaining component is E_x, directed parallel to propagation direction. Therefore at UHR, X waves shows only a electrostatic character. The incoming electromagnetic wave, which is becoming purely electrostatic now, then matches the Bernstein oscillations modes. From a physical point of view, at UHR, the two oscillation modes may be regarded as oscillators coupled by the

electric field of the X waves, that in the following will be named E_0. In the description that follows initially neglect the term $\vec{k} \cdot \vec{r}$ of the waves for simplicity, only adding it at the end of treatment.Therefore, at UHR, the motion equation for the Bernstein mode can be written as:

$$\frac{d^2x_1}{dt^2} + \omega_1^2 x_1 = c_1 x_2 E_0 \cos(\omega_0 t) \tag{2.6.10}$$

where x_1 and ω_1 indicate the amplitude and resonant frequency of the first oscillator, whereas x_2 is the amplitude of the nascent Bernstein wave. C_1 is the constant indicating the strength of the coupling. A similar equation can be written also for x_2

$$\frac{d^2x_2}{dt^2} + \omega_2^2 x_2 = c_2 x_1 E_0 \cos(\omega_0 t) \tag{2.6.11}$$

the amplitude x_1 and x_2 are also function of time varying around the respective equilibrium point as:

$$X_1 = \bar{x}_1 \cos(\omega' t) \qquad X_2 = \bar{x}_2 \cos(\omega'' t) \tag{2.6.12}$$

In absence of non-linear interaction, clearly, $\omega' = \omega_1$ and $\omega'' = \omega_2$ and $\omega_0 = \omega_1$, i.e. the frequencies of oscillation of the wave are equal to the frequencies of oscillation of amplitude. In presence of non-linearities this is not true so far, and the driving term can cause a frequency shift so that ω'' is only approximatively equal to ω_2. Furthermore ω'' can be complex, since there is damping or there can be growth. In either case, x_2 is an oscillator with finite quality factor Q [1] and can respond to a range of frequencies about ω_2. In absence of non-linear interaction, the solution of the system of coupled equations (2.6.10-2.6.11) is:

$$\omega'' = \omega_0 \pm \omega' \tag{2.6.13}$$

If ω' is small, both choice for ω'' may lie within the bandwidth of x_2, and one must allow for the existence of two oscillator $x_2(\omega_0 + \omega')$ and $x_2(\omega_0 - \omega')$ Solving equations (2.6.10-2.6.11) with such assumptions, one finds the matching conditions:

$$\omega_0 \simeq \omega_2 \pm \omega_1 \tag{2.6.14}$$

Once the term $\vec{k} \cdot \vec{r}$ is taking into account, a new matching condition arises:

$$\vec{k}_0 = \vec{k}_2 \pm \vec{k}_1 \tag{2.6.15}$$

The two conditions (2.6.14-2.6.15) are easily to be understood by analogy with quantum mechanics. In facts, by multiplying the former by plank's constant $\hbar$, we see that equation (2.6.14) correspond at the energy conservation law for photon-like quantity. Similarly. equation (2.6.14) states the conservation of momentum $\hbar\vec{K}$. The wave of type X, then, in proximity of UHR, generate two waves, the high frequency Bernstein wave, and secondary low frequency wave, which can be proved to be of ionic type [1]. Each one will propagate in opposite direction to the other. A measure of the electromagnetic field performed in conjunction with the phenomenon of mode conversion must then reveal the presence of ionic waves in the range of MHz. Furthermore, at UHR resonance, oscillation frequency of the X wave assumes the form: $\omega_1 = \omega_0 \pm \omega_2$. This leads to the formation of secondary peaks around the main frequency of the electromagnetic wave incident, called sidebands and also characteristics of the mechanism of mode conversion. **The simultaneous presence of ion waves and sidebands around the pumping frequency is consequently an important fingerprint of the modal conversion occurrence in in E.M generated plasmas**

2.6.3 Instability threshold

Parametric instability will occur at any amplitude if there is no damping, but in practice even a small of either collisional or Landau damping (see next section) will prevent the instability unless the pump wave is rather strong. to calculate the threshold, one must introduce the damping rates Γ_1 and Γ_2 of the oscillator x_1 and x_2. The friction terms can be written as $\Gamma_1 dx_1/dt$ and $\Gamma_2 dx_2/dt$. Equations (2.6.10-2.6.11) then becomes:

$$\left(\omega_1^2 - \omega^{'2} - i\omega'\Gamma_1\right) x_1(\omega') = c_1 x_2 E_0 \cos(\omega_0 t) \tag{2.6.16}$$

$$\left(\omega_2^2 - (\omega' - \omega_0)^2 - i(\omega' - \omega_0)\Gamma_2\right) x_2(\omega' - \omega_0)^2 = c_2 x_1 E_0 \cos(\omega_0 t) \tag{2.6.17}$$

Solving the equations system in function of one of the two oscillators, and restricting to the simple case of two waves, i.e. $\omega' \cong \omega_1$ and $\omega_0 - \omega' \cong \omega_2$ one obtains:

$$\left(\omega'^2 - \omega_1^2 + i\omega'\Gamma_1\right) = \left[(\omega_0 - \omega')^2 - \omega_2^2 - i(\omega_0 - \omega')\Gamma_2\right] = \frac{1}{4} c_1 c_2 E_0^2 \tag{2.6.18}$$

at threshold, we may set $Im(\omega) = 0$. The lowest threshold will occur at exact frequency matching, i.e. $\omega' \cong \omega_1$ and $\omega_0 - \omega' \cong \omega_2$. The the previous equation gives:

$$c_1 c_2 \left(E_0^2\right)_{thres} = 4\omega_1\omega_2\Gamma_1\Gamma_2 \tag{2.6.19}$$

The modal conversion, consequently, can not be at any value of power of the electromagnetic field which propagates all'UHR. How large part of the non-linear phenomena, on the contrary, there is a threshold frequency above which the phenomenon of conversion X-B begins.

2.7 Absorption of E.S waves

2.7.1 Landau Damping

Landau damping occurs due to the energy exchange between a wave with phase velocity v_ϕ and particles in the plasma with velocity approximately equal to v_ϕ, which can interact strongly with the wave. Landau damping is a characteristic of collisionless plasmas, but it may may have also application in other fields (galaxies and stars formation). The complete discussion of the problem is quite complex and beyond the scope of this thesis. A complete treatment of the problem can be found in reference [1]. The phenomenon of Landau damping arises when the electrostatic waves have phase velocity $v_{\ phi}$ similar to the thermal speed v_{th} of the plasma particles. In such conditions, if the particles move at exactly the same speed of the wave, they will not even notice the presence of the fluctuating electric field. but if the thermal speed is slightly different, they will be influenced by the motion of the wave. The particles with $v_{th} < v_{\ phi}$ will be accelerated by absorbing wave energy. Those with higher speeds, on the contrary, will be slowed, and will give up their energy to the wave. According to figure 2.7.1(a), a Maxwellian distribution in the number of particles decreases with increasing speed. For which the overall effect of the interaction of the wave with the particles is to a damping of the wave and of a consequent heating of the electrons, in the case of electrostatic waves of electronic nature, or of the ions, in the case of ionic waves. The Maxwellian distribution will be therefore distort in the region where the damping occurred. In certain circumstances, the phenomenon can be opposed. If the Maxwellian distribution presents secondary peaks to higher energies, as shown in figure 2.7.1(b) will this time the wave electrostatic energy gain at the expense of the particles.

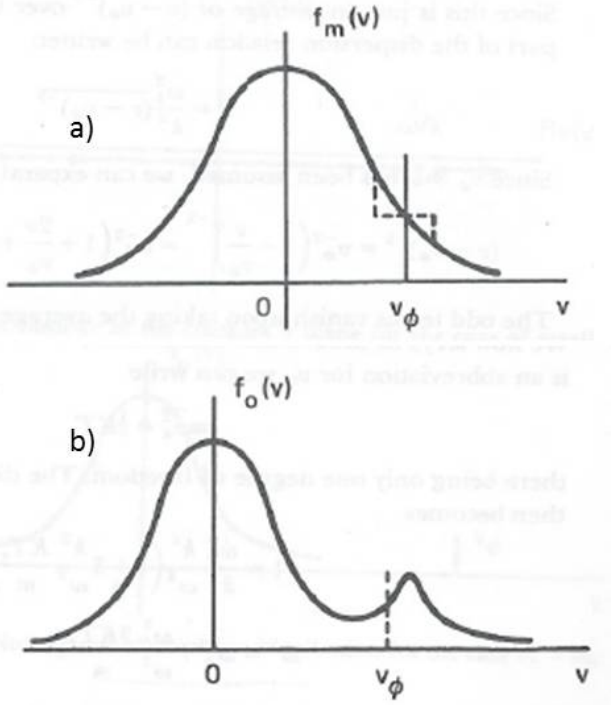

Figure 2.7.1: (a) Distortion of a Maxwellian distribution in the region $v \cong v_{phi}$ caused by Landau damping. (b) A double-humped distribution and the region where instabilities will develop.

A quantitative approach to the landau damping leads to the following equation:

$$Im\left(\frac{\omega}{\omega_p}\right) = -0.22\sqrt{\pi}\left(\frac{\omega_p}{kv_{th}}\right)^3 e^{-12k^2\lambda_D^2} \tag{2.7.1}$$

The minus sign of the imaginary part indicates the absorption of the wave by the particles. The damping is extremely small for small $k\lambda_D$. The phenomenon of Landau damping may surround both electrons and ions. In case electronic, however, the Landau damping can take place only in a direction parallel to the magnetic field. In other words, only electrostatic waves that propagate parallel to the magnetic field (Langmuir waves) can be absorbed by the electrons, whereas for ions such a restriction does not exist. To clarify the causes of this limitation we need to remember what

was introduce in the last chapter. Electrons can not move across $\vec{B}$ because of their strong magnetization and can not absorb waves moving across B. Ions, being unmagnetized because of the collisions, does not suffer such limitation. The main consequence of this treatment is that landau damping can not explain the absorption of EBW, being waves propagating across the magnetic field and another damping mechanism is needed.

2.7.2 The Sagdeev and Shapiro damping

Landau damping disappears if the wave is propagating across a magnetic field. However Sagdeev and Shapiro have suggested [68] a different collisionless mechanism able to explain the absorption of electrostatic waves propagating across a magnetic field. The Sagdeev-Shapiro damping consists in a acceleration of electrons in the direction perpendicular to the direction propagation across the magnetic field lines. The electrons which are trapped by the B wave potential, move with the wave and experience some oscillation inside the potential well. Without loosing in generality we assume, as usual, the magnetic field directed along the $\hat{z}$ axis, and the particle moving in the field generated by the Bernstein waves along the $\hat{x}$ axis. In such condition the motion equation is:

$$m\frac{dv}{dt} = eE_0 \sin(k_b x) + \vec{v} \times \vec{B} \tag{2.7.2}$$

the transverse component of the previous equation are:

$$\frac{dv_y}{dt} = \omega_c v_\phi \tag{2.7.3}$$

$$\frac{dv_x}{dt} = -\frac{e}{m} E_0 \sin(K_B x) - \omega_c v_y \tag{2.7.4}$$

where E_0 is the amplitude of the Bernstein wave. The electrons trapped by the Bernstein wave oscillate during the lapse of time while they are trapped. This means that they escape from the potential well as soon as the right-hand side of equation (2.7.4) changes its sign. It happens when the second term becomes equal or larger than the amplitude of the first term, i.e. when:

$$v_y^{max} = \frac{eE_0}{m\omega_c} \tag{2.7.5}$$

Consequently the maximal obtainable energy is:

$$W^{max} = \frac{e^2 E_0^2}{2m\omega_c^2} = -\frac{1}{2} m \left(\frac{E_0}{B}\right)^2 \tag{2.7.6}$$

Expressing E_0 in terms of the energy flux density of the wave $P = E_0^2 v_\phi / 2$ previous formula becomes:

$$\frac{mP}{v_{\phi B^2}} \tag{2.7.7}$$

This equation shows that **the energy which can be acquired by the electrons increase infinitely where the phase velocity of the wave go to zero, i.e. at the harmonics of the cyclotron harmonics**, according to equation (2.5.10). It means that the absorption mechanism of the Bernstein waves is able to generate very energetic electrons. **The results is the appearance of shell-like energetic hot electron layers** [69]. Even if several cyclotron harmonics are present in a given plasma, in practice only two very energetic layers appears. The reason is that a resonant surface is theoretically an impenetrable barrier for Bernstein waves, since both phase and group velocity are zero at resonance [1]. The hot electron layers are quite thin because the electron acceleration take place in the near vicinity of the cyclotron harmonics surfaces, and the diffusion of the accelerated electrons is restricted by the magnetic field [69]. One of the main consequences of Sagdeev and Shapiro damping is the formation, in case of cylindrical geometry, of a azimuthal electronic current. This is because the electrons are accelerated perpendicularly to both the magnetic field to the direction of propagation of the wave. The azimuthal current can have both diamagnetic or paramagnetic characteristics depending on the direction in which the Bernstein wave is propagating [69].

2.8 Remarks about EBW heating

2.9 Remarks about wave propagation in plasmas

The theory on the E.M wave propagation in magnetized plasmas shows incontrovertibly its main limitation. The discussion followed the propagation of electromagnetic waves in magnetized plasmas has shown incontrovertibly the main limitation of this method of ignition of the plasma: Both ordinary waves that are reflected extraordinary wave above the respective cutoff density, (O cutoff for ordinary waves, L cutoff for the extraordinary). The experimental measurements confirm the theoretical results: In the case of

the ECRIS were measured plasma density slightly higher than the cutoff wave O [24], while the MDIS, thanks to the non-resonant absorption of the electromagnetic waves, can generate plasmas with density 2-3 times higher than the cut-off value [2]. However, it is clear that the only way to raise the value of the electron density is to increase the microwave frequency, so that the density cutoff occurs at higher values. The increased frequency RF also involves the increase in the magnetostatic field associated, according to the scheme shown in the following equation:

$$n_{cutoff} \propto \omega_{RF} = \omega_c \propto B_{ECR} \tag{2.9.1}$$

Consequently, the increase in performance of the sources of new generation implicitly involves a continuous increase of the magnetic fields used. The latest generation of ECRIS in the design phase, for example, have being projected to operate at frequencies in the range 40-56 GHz and to make use of magnetic fields (generated by superconducting materials) of the order of 7 T [25]. By looking to the results of ECR ion sources in the last thirty years, it is evident that such a rush cannot be continued "ad libitum". For highly charged ions, the increase of available beam current accounted to one order of magnitude per decade. Moreover, the technological limits of the superconducting magnets and of microwave generators, as well as the increasing cost, suggest that the saturation point is approaching. The above discussion explains why in recent years the search for new technologies of plasma ignition has become a priority. One possible candidate to replace the heating electromagnetic waves is represented by the Electrostatic waves, and in particular by the Bernstein waves. These waves are not affected by any cutoff and can propagate and be absorbed in widely overdense plasmas. Necessary condition for the EBW generation is the presence of the UHR resonance, which exists when $\omega_p < \omega_{RF}$ and $\omega_c < \omega_{RF}$ or, in terms of plasma parameters, $X < 1$ and $Y < 1$. UHR lies between the fundamental harmonic (B_{ECR}) and the first harmonic ($B_{ECR}/2$), as shown in figure 2.9.1.

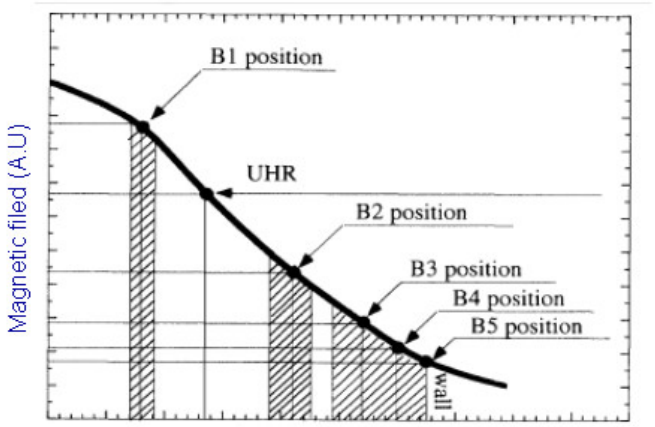

Figure 2.9.1: UHR and cyclotron harmonics Position as a function of the magnetic field [69].

As explained in the previous sections, the generation and absorption of EBW can be demonstrated by means of 3 fundamental evidences:

1. *Appearance of sidebands in the spectrum of the pumping electromagnetic waves and of ion waves in the range of MHz;*

2. *Generation of large energy electrons (with respect to the usual energies in the source;*

3. *Achievement of densities much higher than the density cutoff;*

In chapter 5, each of these signatures will be taken into consideration to demonstrate the effective excitation and the consequent absorption of EBW.

Chapter 3

Introduction to the ion sources and beam characteristics

The ion sources represent the first stage of an acceleration facility. It generates and contains the plasma from which is then extracted the ion content. In the last century several types of ion sources have been developed, each one characterized by a different manner to generate and maintain the plasma. These differences cause the plasma generated in the different ion sources to differ for electron temperatures and densities and plasma for lifetime. Obviously, these properties reflect on the ion beam. Generally, plasmas are created by means of electrical discharges under vacuum, by means of electron beams passing through the neutral gases or, as introduced in the previous chapter, by means of electromagnetic waves interacting with gases or vapours, in presence of a well shaped magnetic field. Ion sources based on this last method usually produce plasmas by means of the Electron Cyclotron Resonance or by means of the so-called off-resonance discharge. They are frequently used in modern accelerator facilities, as they enable to reach larger highly charge states and extracted currents than other devices. In the forthcoming chapter a brief description of the main ion sources and of the corresponding ion beams will be given. Particular attention will be paid to the Electron Cyclotron ion sources and Microwave discharge Ion sources, which represent the equipment on which a large part of the experimental measurements have been carried out.

3.1 Ion sources requirements

Ion sources represent the first stage of the acceleration system. Each accelerating device needs an ion source able to generate beams fulfilling having well-defined requirements in order to maximize the performances. In particular, main requests are:

- **High charge states** q: especially in case of ion sources for cyclotrons, for which the maximum accelerating energy is proportional to q^2;
- **Intense extracted current** I_e: especially for experiments involving low cross section reaction measurements; high currents help to considerably reduce the acquisition times;
- **High reliability** and **high brightness**: required to increase the efficiency of the device;

As discussed in section 1.2 about the step by step ionization process, the mean charge state available depends on the quality factor of the source

$$< q > \propto n_e \tau_c \tag{3.1.1}$$

and on the electron temperature T_e, according to equation (1.2.9). The ion confinement time will be a crucial parameter to determine the maximum achievable charge state. To minimize the charge exchange phenomena (which decreases $< q >$), we need that the number of neutrals n_0, and hence the background pressure $P_0 \propto n_0$, be sufficiently low, as stated by equation (1.2.11). Therefore, ion sources devoted to the production of highly charged ion beams need a magnetic structure able to confine the plasma and increase the ion lifetime. On the contrary, the extracted current is inversely proportional to the confinement time [2]:

$$I_{extr} \propto \frac{n_e}{\tau_i} \tag{3.1.2}$$

Too long confinement time, hence, limit the amount of ions extracted from the plasma per time unit, thus reducing the expected current. By equations (3.1.1) and (3.1.2) may be noted that the crucial parameter for generating high currents of highly charged ions is n_e. Only by maximizing the density, it is possible to increase both the current and the charge states. These simple considerations on the main proportionalities of current and charge states are decisive to address the research in the field of ion sources.

Once known the physical processes able to maximize the electron density and the plasma lifetime, then new techniques and methods for plasma heating to apply on ion sources can be developed. Finally, in order to perfectly match the ion sources with the accelerators, the beam quality must be high, especially in terms of emittance and beam brightness (such requirements will be detailed in section 3.5.1). Other important characteristics of ion sources are important, as the reliability, the lifetime of the system, the maintenance and the last, but not the least, the cost (for building and for ordinary operations).

3.2 Principal ion sources

The development of the ion sources is closely linked to that of the accelerators. The design of new accelerators triggered the research on ion sources able to satisfy their request. At the beginning of the last century some surface ionization sources and electron impact sources with low intensity and low energy spread were developed and used in mass spectroscopy [84]. In the thirties the costruction of the Cockcroft-Walton type accelerators and the development of the first Cyclotron stimulated the development of the Penning sources. In fifties the large number of Van de Graaf accelerators encouraged detailed studies on RF sources. The development of high energy accelerators resulted in the discovery and development of the duoplasmatron [4]. Tandem accelerators encouraged the development of negative ion sources. In the seventies the research on ion sources come to a golden age with the development of the Electron Beam Ion Sources (EBIS), the Electron Cyclotron Ion sources, The Metal Evaporation vacuum (MEVVA) ion sources, the laser ion sources (LIS), while the use of cesium improved the performance of negative ion sources. In the following we briefly describe the most commonly used ion sources for production of mono and multicharged ions:

The Penning Ion Gauge (PIG source)

The Penning Ionization Gauge (PIG) [84] discharge is composed of two cathodes positioned at the extremity of an hollow anode. Electrons from one cathode are accelerated trough the hollow anode and reflected at the oppositive cathode. A strong magnetic field is used to further increase the electron path. The electrons are therefore forced to oscillate between the two cathodes ionizing the gas up to high charge states. Confinement time is

proportional to the strength of the magnetic field and to the surface of the plasma. PIG sources are able to deliver ion beams whith charge states up to 16^+ (for xenon). Typical currents are of the order of $10 \div 100 mA/Acm^2$, where A is the ion mass. However, such sources have different disadvantages: the beam has a poor quality and it varies during the source operations; the components have a short lifetime, especially when the source is optimized for charge states as 12^+, 14^+, so that the source is not suitable for long running activities needing high reliability [84].

Electron Beam Ion source (EBIS)
In the EBIS [48] the plasma is generated by an electron beam produced by an electron gun. Plasma is immersed in a uniform magnetic field produced by a solenoid. The highly charged ions are generated by successive electron impact. All the high performance EBIS uses superconducting magnets able to produce magnetic field of 1.7-5 T to increase ion lifetime, and cryogenic pumping to create a residual gas pressure lower than 10^{-10} mbar and avoid charge exchange between particles. Such solution make possible the production of completely stripped light ions or highly charged heavy ions up to 54^+ with an advanced version of EBIS, thereby called EBIT (Electron Beam Ion Trap). In particular it was possible to generate a few particle per second of U^{90+}. According to equations (3.1.1) and (3.1.2), for very high charge states the maxima currents are not higher than some nA. The low currents, together with the high realization costs of this very complex device, represent their main disadvantages.

RF ion source

There are two ways in which a low-pressure gas can be excited by RF voltages: 1) a discharge between two parallel plates across which an alternating potential is applied (capacitively coupled discharge) and 2) a discharge generated by an induction coil (inductively coupled discharge). In this case, an azimuthal RF electric field is generated by the alternating magnetic field in the discharge region. Electrons constrained into oscillation by the RF electric field acquire enough kinetic energy to ionize the background gas atoms. Typical operating parameters for RF sources are the gas pressure 10^{-3} mbar, the RF frequency ~ 10 MHz. A $\vec{E} \times \vec{B}$ drift generated by the RF electric field, and the subsequent $\vec{j} \times \vec{B}$ causes a partial plasma compression, thus increasing the plasma density up to $10^{11} cm^{-3}$, and makes this source able to deliver several tens of mA of positive or negative mono-charged ions [4]. However, as no magnetic confining system are used, this source is not

able to produce highly charged ions; furthermore, the extracted beams show a large energy spread due to the influence of the strong RF electric field existing in the extraction region [4].

Laser Ion Source (LIS)

In Laser Ion Sources [84], the plasma is generated by the interaction of a focused laser beam onto a solid targets. If the power density of the laser beam is high enough, a rapid vaporization of the target material occurs, and a plasma plume is generated expanding at supersonic velocities. Typically the laser energy used by LIS varies from 1 J to 50 J, with pulse lengths up to 1 μsec and repetition rate up to 1 Hz for CO^2 lasers. The electron temperature T_e, and the charge $< q >$ states distribution depend on the laser properties:

$$T_e = (P < q >)^{\frac{2}{7}} \tag{3.2.1}$$

where P is the laser power. The main limitation to the use of LIS in the accelerator facilities is linked to the low repetition rate. This is mainly due to the laser pumping, which requires a lot of time especially in case of high power - high intensity lasers. Furthermore, the extracted beam are usually characterized by a large emittance, leading to poor quality ion beams. It has been demonstrated that a strong electric field can be generated inside the plasma plume, and these field can accelerate the ions up to MeV energies in case of laser at high intensities. In the next future, therefore, the LIS method could conjugate either the ion formation and then their acceleration to high energies.

3.3 ECR-based ion sources

ECR-based ions sources generate a plasma by means of the absorption of E.M waves in the microwaves range. With respect to the afore-mentioned ion sources, ECR ions sources maximize the quality parameter $n_e\tau_c$. Equations (3.1.1) and (3.1.2) show how the confinement time is a fundamental parameter to determine the characteristics of the extracted beams. A high confinement time leads to the production of relatively low current of highly charged ion beams, while a low confinement time determines high currents of low charged ions (generally 1+ ionized). **Electron cyclotron Ion sources (ECRIS)** can be included in the first category, whereas the **Microwave Discharge Ion Sources (MDIS)** belong to the second one. For sake of

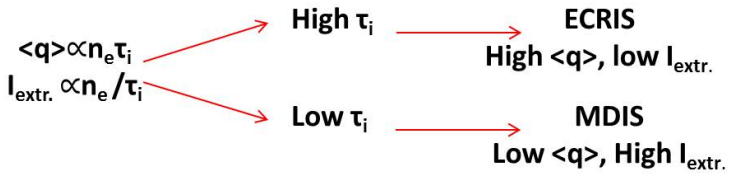

Figure 3.3.1

simplicity, the main differences between ECRIS and MDIS can be depicted as in figure 3.3.1.

3.3.1 ECRIS

Electron Cyclotron Resonance Ion Sources were first proposed by R.Geller in 1965 [55]. In 1971 the first operational ECRIS, called MAFIOS, was completed. The long ion confinement time is obtained by means of a B minimum structure, whose properties were introduced in section 1.6.2 The Electron Cyclotron Resonance ensures a resonant absorption of electromagnetic energy by the plasma electrons. At the beginning of the discharge process few free electrons, spiralizing around the magnetic field lines, are accelerated by the electric field of the injected microwaves. In a time of several hundreds of μs the discharge develops with an avalanche of ionization events. Then a plasma in a stationary state is established. The electron-atom collisions allow to obtain multiply-charged ions, and very high charge states can be reached because of quite long confinement times ($\gg 10^{-3} - 10^{-2}$ sec).
The B minimum magnetic configuration is generated by means of two or three solenoids producing an axis-symmetric simple mirror structure, while an exapole generates a field which increases from the the center of the plasma chamber to the walls. Electrons are mainly heated, by means of ECR, in the region of the chamber where $B = B_{ECR} = qB/m$ which is an iso-B surface with egg-shaped structure. Figure 3.3.2 shows the typical B-minimim trap [10], whereas in figure 3.3.3 a simulation of the electron dynamic within the B minimim trap is shown. From the two images it comes out that the largest part of particles is well confined inside the egg-shaped resonant surface. This effect, not adequately investigated in the past, has been recently focused by the Catania's group; it is based on the additional confinement provided by the resonant acceleration of cold electrons crossing for the first the resonance layer. In [56] it largely commented why do the electrons fluxes

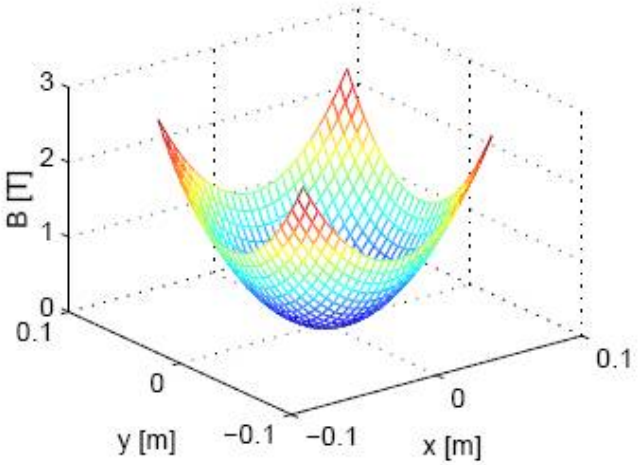

Figure 3.3.2: B-minimum field structure in a ECRIS. The magnetic field is given by the sum of the field generated by two solenoids (simple mirror) and of the field generated by an hexapole.

are concentrated in the axis region. According to this model, the plasma separates in two well distinguishable regions called "plasmoid" (inside the ECR surface) and "halo" (outside the ECR surface).

The constituents an ECRIS can be summarized as follows:

- resonant cavity: it is a vacuum metallic chamber containing the plasma, which acts as a resonant cavity for the microwaves necessary so that we can have resonance ECR. It is insulated from the magnetic system and usually positively charged to allow the extraction of the ions;
- System of magnets for the magnetic confinement of the plasma: is formed by two or more solenoids which generate a Simple Mirror type field for axial confinement and by a multipole magnet (usually a hexapole) to improve the radial confinement;
- Gas injection system and microwaves injection;
- Extraction of the ion beams with different charge states in the plasma. Appropriate generators or amplifiers (magnetron, TWT) provide microwaves, whose frequencies span from about 2 GHz to about 30 GHz, which are delivered to plasma trough circular or rectangular waveguides.

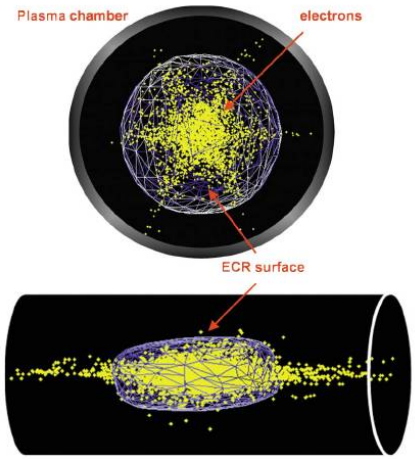

Figure 3.3.3: Simulated electrons inside the SERSE plasma chamber together with the egg-shaped ECR surface.

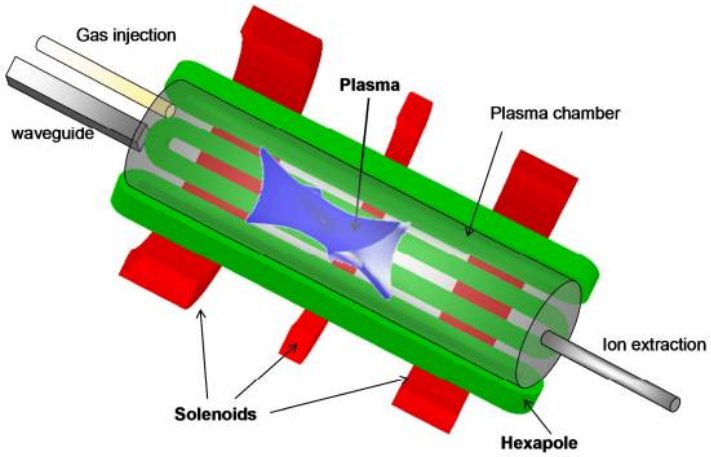

Figure 3.3.4: The main ECRIS devices (magnets, microwave injection, gas injection, ion extraction, plasma chamber) together with the six-cusp plasma generated in the central region of the plasma chamber.

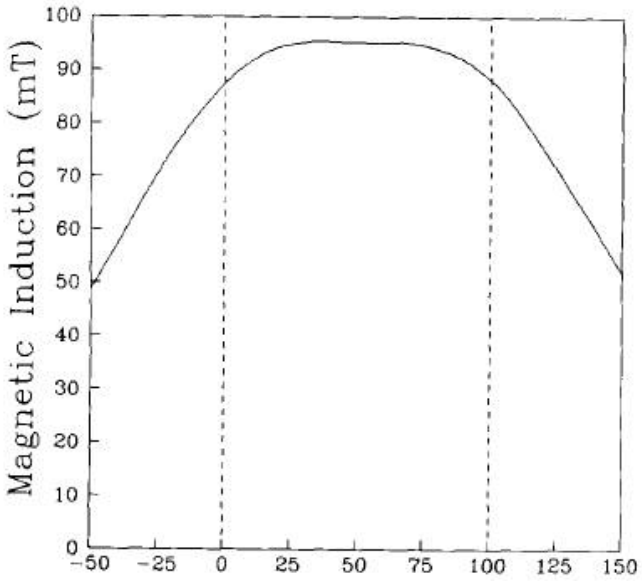

Figure 3.3.5: Magnetic field profile of the MDIS designed by Taylor and Willis in 1991 [57]. The dashed vertical lines define the axial extent of the plasma chamber. Nowadays the magnetic field is designed to be zero in extraction region, in order to decrease the beam emittance, proportional to the field at extraction.

3.3.2 MDIS

The Microwave Discharge Ion Sources were first developed at the beginning of 90^{th} for the production of high currents of proton beams and light ions [57]. Their principal characteristic is the absence of a confining magnetic field. On the contrary, the magnetic field is about flat within the plasma chamber. The shape of the magnetic field is designed in order to allow that the injected microwaves match ECR conditions at the injection and extraction points. In the central region of the plasma chamber, the field is about flat and off-resonance, i.e. $B > B_{ECR}$, according to figure 3.3.5 showing the magnetic configuration of the first MDIS [57]. Trough the years the magnetic field profile changed only in the extraction region. Nowadays the magnetic field is designed to be zero in the such a region, in order to decrease the beam emittance, which is proportional to the field at extraction.

A large part of the MDIS operates at 2.45 GHz, with a off-resonance magnetic field of 0.1 T in the center of the plasma chamber. Several measurement carried out during the last decades (and reported also in this

thesis demonstrate that **slightly overdense plasmas can be generated in MDIS** [2], which are not expected by the standard theory of E.M absorption. In particular, Sakudo [61] demonstrated that the higher plasma density is obtainable when $B_{ECR} < B < 1.3B_{ECR}$.
Different theories have been proposed to explain the plasma ignition in MDIS: a first theory, due to Geller [2], takes into account the off-resonance plasma effervescence. In the case of dense and turbulent plasmas a strong effervescence may arise, leading to a collective scattering frequency ν_{ω_p} depending on the plasma frequency ω_p. When $\nu_{\omega_p} > \omega_c$ the electron gyromotion is strongly perturbed by the collective collisions and during the ECR acceleration, the electron may go out of phase with respect to the wave because of such collective collisions (see figure 3.3.6). This means that the equivalent gyro-period is higher than in the collisionless case. In order to recover the synchronization with the rotating wave electric field, the electron needs to go faster and faster, then to gyrate around a magnetic field line whose field values is higher than B_{ECR}. Once the synchronization is recovered, the acceleration goes on. Then the off-resonance magnetic field allows the acceleration even for those electrons which go out of phase at the ECR zone. The main limitation of such a theory is that it does not explain why MDIS plasmas are overdense. The second theory is somehow similar to the previous one but it considers the electron-neutral collisions instead of the collective collisions. However it is valid only if the electron-neutrals collision frequency is comparable with the microwave frequency. This occurs when the neutral pressure is higher that 10^{-1} mbar, i.e it is not satisfied in large part of the cases, as MDIS usually operate at $10^{-4} - 10^{-5}$ mbar. Another theory applies to the cases of off resonance wave-plasma interaction. Different authors [62]-[63] affirm that resonances between the electromagnetic waves and the plasma electrons can occur in off-resonance magnetic fields (Y¿1) and in high densities condition (X¿1). How was detailed in section 2.1.3 in the X¿1, Y¿1 region of the CMA diagram, ordinary wave can couple to the electrostatic oscillation modes, in particular to the lower branch of T.G. modes, which can propagate in overdense plasmas. However, such regions need to be reached by tunneling of the Ordinary wave beyond the O cutoff, before they can be absorbed by electrostatic T.G. waves which, only in a second moment, could transfer the oscillation energy to the medium by means of collision or nonlinear interaction wave-electron, generating a low temperature high density plasma. Also this theory, however, needs further confirmation. A large part of the measurements present in this thesis have been carried out in a MDIS in a different magnetic configuration. In partic-

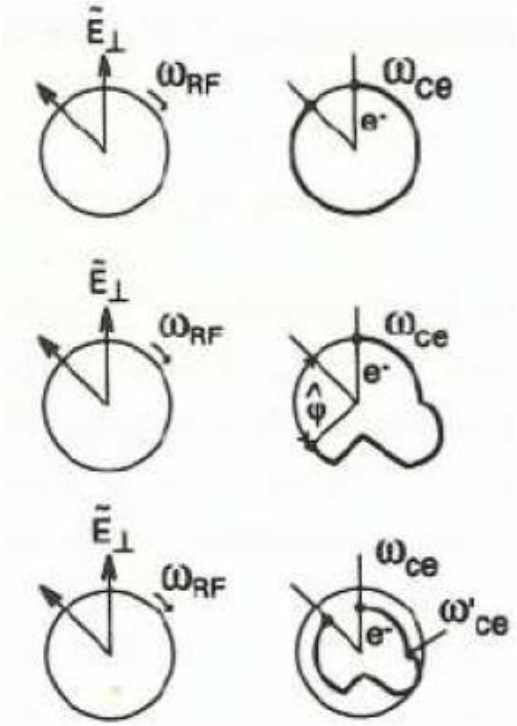

Figure 3.3.6: R wave electric field vector rotations and electron gyrations in ECR (bottom), off-ECR (middle), and with B ¿ BECR [2].

ular we have studied the performance of our source in an under-resonance magnetic configuration, ($\omega > \omega_c$, Y¡1). Also in these conditions ECR is not possible, but the eventual presence of the UHR can enable the generation and propagation of EBW, which then can be absorbed at the cyclotron harmonics, generating an overdense plasma. The absorption of the electrostatic waves is really more effective than the usual off-resonance heating. In particular this heating methodic increases significantly both electron density and temperature, and therefore of the energy content of plasma $n_e t_e$. This new plasma heating approach, once adequately studied, can therefore represent a step forward in the field of MDIS (and in general, of all ECR-based ion sources) because can allow to generate high current of multi-charged light ions by means of a simple and inexpensive device (with respect to other ion sorces) like MDIS.

3.4 Ion sources at INFN-LNS

The development of different types of ion sources has been one of the most valuable assets for the Laboratori Nazionali del Sud (LNS) [49], strongly supporting the upcoming needs of nuclear physics research during the last 25 years and of multidisciplinary physics in the most recent years. The activity of the team started in 1983 when a standard negative ion source was installed as injector for the Tandem accelerator. The major activity started at the end of Eighties, aimed to the design of the injectors for the **K-800 superconducting cyclotron** (SC), in order to let it work in stand-alone mode. At the beginning, in facts, in absence of a positive ion source, Tandem was used as injector for the SC. An ECR ion source devoted to product highly charged ion beams would allow better performance than in the Tandem-coupled mode, either in terms of available charge states and in terms of beam intensity and reproducibility. In 1990 the proposition of the High-B mode concept [51] was the trigger for the preliminary design of the **superconducting SERSE source** in 1991 [52]. In the same years (1989-1993) the tests of biased disk method in collaboration with KVI [53] and the explanation of this phenomenon and the demonstration of High-B mode in collaboration with MSU-NSCL were carried out [54]. In 1992 the project for the construction of the superconducting SERSE source was approved by INFN and funded in 1993. The construction began in 1994, completed in 1997 and installed in June 1998 at LNS. In 1997 the construction of a second, conventional ECRIS was funded; the source, named **CAESAR** [58], was completed at the end of 1998 and installed in 1999 at LNS. During the construction of SERSE, a new field of research was investigated, i.e. the efficient ionization of atoms, to be used for the **Radioactive Ion Beam Facility EXCYT**. The microwave discharge ion source **MIDAS** [59] was designed in 1993 and the prototype was built in the following years. The final goal was achieved in 1999 by the second version MIDAS2 [60], with excellent ionisation efficiency for many species. After, a completely new MDIS was designed and named **TRIPS** (**TRasco Intense Proton Source**). The source was completed early in 2003 and its performance exceeded the requirements of the **TRASCO (TRasmutazione SCOrie)**project. The aim of the TRASCO project was to verify the conceptual design of an Accelerator Driven System (ADS) for nuclear waste transmutation and to develop the related technologies, according to the Rubbia proposal [64]. A new compact version, the **Versatile Ion Source VIS** [65] with permanent magnet was built in 2008. A **plasma reactor** aimed to the dissociation of complex molecules and also to the study of the propagation and absorption of

microwaves in cold (T≪100 eV) and weakly ionized plasmas was here designed and installed in 2007. Even if different R&D was developed in the course of last years, the major commitment remains the study and design of innovative ion sources. In fact the study of ECRIS operations at higher frequency than 18 GHz was started within the frame of a RTD programme funded through the 5^{th} **Framework Programme of European Union**. This programme named "**Innovative ECRIS" (INES)** was mainly based on the study of intense beam production for highly charged heavy ions; a test for the coupling of a 28 GHz-10 kW gyrotron-based generator to the SERSE source was carried out and the study of the scaling laws was done at the different frequencies (14,18,28 GHz) permitted by this superconducting ECR source, at that time the unique tool worldwide able to perform such experiment. It should be remarked that not only a beam current close to the one needed for the next generation of accelerators was obtained (above 0.5 mA for charge states between 20 and 25^{+} for Xenon), but also a collection of data required for the design of 3rd generation ECRIS was gathered, thus completing the preparation of the **GyroSERSE project**, conceived in 1994 and proposed in 1999. In 2003 the **ISIBHI** collaboration was established within the EURONS proposal for the 6^{th} Framework Programme and the GyroSERSE project was used as the basis for the design of the prototype **MS-ECRIS**. The construction was funded for the period 2005-2008 with the contribution of INFN, GSI, GANIL and other European Laboratories. The source commissioning will be carried out at GSI, Darmstadt. The activities concerning the microwave-generated plasma and ECR ion sources have been also applied to medical applications. Our team has been asked to elaborate the design of the ion sources for the **CNAO** accelerators (**Italian Center for Oncological Hadroterapy in Pavia**). A relevant role in the success of the **CNAO** sources was played by the discovery of the "**Frequency Tuning Effect**". INES and the following **HELIOS** experiment (2009-1012), have given a remarkable insight of the EEDF formation in ECRIS plasma and they permitted to explain clearly the mechanism underlying the frequency heating and the origin of high energy tails in the X-ray spectra. Recently the LNS R&D group has been involved in the **European Spallation Source (ESS)**, to be built in Lund, Sweden, devoted to the production of neutron beam for different applications from a proton beam, and in the **DEδALUS** project, which will make use of MDIS as injector of a new high power cyclotron to be installed in USA.

3.5 Beam parameters

3.5.1 Emittance and Brightness

The quality of the ion beam extracted from an ion source is mainly characterized by the beam emittance and brightness. These quantities are frequently used to determine the compatibility with given beam transport and optical systems. The emittance is the volume of the beam in the phase space and it represents a measure of its dispersion. By definition the emittance is the six dimensional hyper-volume of a certain fraction of the particles in a bunch divided by π:

$$\epsilon = \frac{1}{\pi} \int\int\int\int\int\int dxdydzdp_x dp_y dp_z \tag{3.5.1}$$

For uncoupled motion in which a beam is moving along the $\hat{z}$ direction under the action of conservative forces, the four-dimensional hyperarea V_4^t or transverse phase space area is a conserved quantity, according to Liouville's theorem. If also the motion along $\hat{x}$ and $\hat{y}$ directions is decoupled, the four-dimensional hyperarea can be factorized as:

$$V_4^t = A^x A^y \tag{3.5.2}$$

Because of the predominately elliptical shape of emittance figures, most authors proceed to define the emittance as the **half-axis product of an ellipse with an area equal to the emittance area occupied by a certain fraction of the particle distribution**:

$$\epsilon^x = \frac{A_x}{\pi}, \qquad \epsilon^y = \frac{A_y}{\pi} \tag{3.5.3}$$

Generally the emittance in the transverse space is isotropic, i.e. it does not depend on the choice of the frame in the transverse space. As a consequence $\epsilon^x \cong \epsilon^y$. So it is possible to know the transverse emittance of a beam just by measuring the emittance along a random direction in transverse space to the direction of the beam. For beams extracted from ion sources, a useful estimation of the emittance is given as [45], [46]:

$$\epsilon^{xx'-rms-norm} = 0.016 r \sqrt{\frac{qT_i}{M}} + 0.032 r^2 \frac{qB_0}{M} \tag{3.5.4}$$

where r is the radius of extraction hole [mm], T_i is the ion temperature [eV], B_0 is the (eventual) axial magnetic field at extraction [T], and finally M and q are respectively the ion mass in *amu* (atomic mass unit) and charge

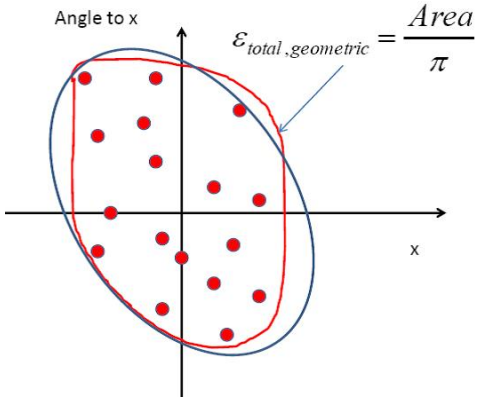

Figure 3.5.1: The emittance can be defined as the ellipse eith an area equal to that occupied by the particle in the phase space.

state of the ion beam. Equation (3.5.4) shows that ion beam emittance depends on two parameters, the ion beam transverse temperature and the axial magnetic field on the extraction region. For the ion sources described in this thesis, the ion temperature is generally very low, because the time needed for ion heating is smaller than ion confinement time (see section 1.2). However, as it will be shown in chapter , Landau damping can heat the ions, leading to an increase of emittance. The presence of an axial magnetic at extraction, on the other hand, can induced the beam rotation (angular momentum). In many cases, however, the thermal term of equation (3.5.4) is much smaller than the magnetic part and can be neglected. To reduce the emittance, usually, the magnetic system is built up in order to reduce significantly the stray field in the extraction area.

For a comparison of different sources, it is often used another quality parameter: the normalized brightness. Because the emittance depends on the dimension of the extraction hole, it is possible to reduce the emittance to an arbitrarily low value. However, this is done at the expense of beam current, and hence, it is not always a practical option. The brightness of the beam gives a measure of how much current can be concentrated in a small spot, and is defined as:

$$B = \frac{I}{\pi^2 \epsilon^{xx'} \epsilon^{yy'}} \tag{3.5.5}$$

Like the emittance, the brightness is an invariant along the beam path,

and a higher brightness is associated with a higher performance beam.

3.5.2 Space charge effects

In high intensity ion beams the space charge created by the ensemble of positive charges constituting the beams can not be neglected. The repulsive force generated by the Coulombian interaction increases the transverse momentum of the beam particles and consequently the emittance. To study the effects of the space charge on the beam, we consider a continuous beam of cylindrical symmetry distribution that moves with a constant velocity $v = \beta c$. For symmetry reason, the electric field has only a radial component E_r. Using the integral form of the Gauss' law over a cylinder centred on the beam axis, one obtains [66]:

$$E_r(r) = \frac{1}{\epsilon_0 r} \int_0^r \rho(r) r dr \tag{3.5.6}$$

The particles of the beam can be seen as set a of parallel currents. This means that particles attract each other by the effect of their magnetic field. For symmetry reason, the magnetic field has only an azimuthal component B_θ. Using the integral form of the Ampere's law over a cylinder centred on the beam axis [66]:

$$B_\theta(r) = \frac{\mu_0 \beta c}{r} \int_0^r \rho(r) r dr \tag{3.5.7}$$

the resulting charge space force $\vec{F} = qE_r\hat{r} + qv\hat{z} \times B_\theta\hat{\theta}$ on a test particle at radius r has only a radial component:

$$\vec{F_r} = qE_r \left(1 - \beta^2\right) \tag{3.5.8}$$

In the above equation, the 1 represents the electric force and the $-\beta^2$ the magnetic force and E_r is given by equation (3.5.6). The electric force is defocusing for the beam; the magnetic force is focusing. The ratio of magnetic to electric force, β^2, is independent of the beam density distribution. For relativistic particles the beam magnetic force almost balance the electric force. For non-relativistic particles (like low energy ion beams) the space magnetic force is negligible and therefore **the space charge has a defocusing effect**. Because of its detrimental effects, beam space charge needs to be removed. The ionization of the residual gas present in the Low Energy Beam Transport (LEBT) allows to generate an electron space charge compensating the positive one of the beam. After the ionization of

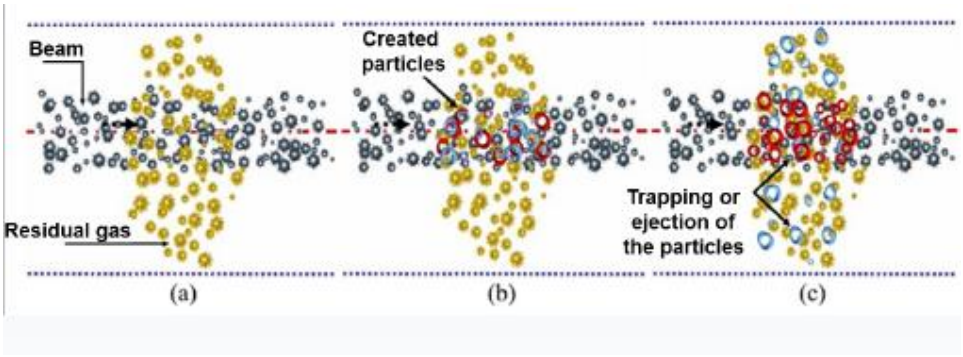

Figure 3.5.2: Sketch of S.C.C principle: a) as the ions beam is extracted from the source, it crosses the residual gas present in the beam line b) the ionization of residual gas generates a cloud of ions and electrons c) ions are expelled from the center of the beam line, electrons are attracted by the beam and compensate the positive space charge of the ion beam.

the residual gas, the ions are expelled from the center of the beam line, where the potential is positive, towards the wall. Electrons from the wall are attracted into the beam, so that the beam is compensated, provided that the pressure is high enough to have an adequate number of electrons (a compromise between beam losses and space charge compensation is to be found experimentally) [67]. In figure 3.5.2 the Space Charge Compensation (S.C.C) principle is synthesized.

Chapter 4

Experimental equipment and diagnostics

The research activity and the experimental measurements shown in this thesis have been entirely carried out at the **Laboratori Nazionali del Sud (LNS)**. A large part of the experimental activities was carried out on the two Microwave discharge Ion sources operating at LNS: **The Plasma Reactor (PR)** and the **Versatile Ion Source (VIS)**. Further measurements have been carried out on the ECRIS **CAESAR**. The plasma reactor enabled us to carry out several different measurements with different plasma diagnostic tools. This device has not any extraction system, and it has been specifically designed for plasma diagnostics, either invasive and non invasive. The experimental data collected with the PR are consistent with a plasma heating mechanism based on modal conversion and generation of Electron Bernstein. Measurements of electron density and hot electron temperature have been performed mainly by means of **Langmuir Probe (LP)** and **X-rays diagnostics**. The microwave spectrum emitted by the plasma has been analysed by means of a **Spectrum Analyzer**. The diagnostic of the extracted beams, which is not possible to perform on PR, was carried out with the VIS source; in particular it has been possible to correlate the beam characteristics to the plasma parameters. Finally, CAESAR allowed to confirm and generalize the conclusions we have derived on the basis of data collected on the two MDIS. The observation of phenomena related to the same physical mechanism but in different devices, furthemore represents a strong confirmation of the used theory and of the physical approach. In the following pages, the devices and the diagnostics briefly introduced here, will been detailed treated.

4.1 The plasma reactor

The operational scheme of Plasma Reactor is basically similar to that of the other 2.45 GHz MDIS. It was originally designed for applications in the field of environmental physics, in particular for reclaiming toxic fumes through the intra-plasma dissociation of complex molecules such as dioxins or fullerenes. In the first measurements carried out in 2006 [73], the reactor was used at high pressure ($0.1 \div 0.5$ mbar), producing a plasma weakly ionized and strongly collisional due to low electron temperatures ($T_e \sim 5 \div 20eV$). The dissociation of complex molecules was carried out in a prelimary test with normal hexane and cyclo-hexane. Hexane fragmentation occurred due to electron impact, since the electron energy was higher than the C_6H_{14} and/or C_6H_{12} dissociation energy. PR is constituted by a stainless steel cylinder 250 mm long, with a diameter of 136 mm and two welded flanges at the ends, for a total of 276 millimeters in length. Figure 4.1.1 show the front (A) and the back/internal (B) part of the PR. In the front there are four flanges, two DN 40, a DN 25 and a flange designed to insert the LP in, hereinafter named LP flange. In the back side two DN 16 and a DN 25 flanges are situated, together with the rectangular shaped waveguide port, used for the microwave injection.

A Nd-Fe-B permanent magnets system (radius 75 mm, 180 mm length), visible in figure, generates an off-resonance magnetic field along the plasma chamber axis (with a maximum of 0.1 T on axis), as shown in figure 4.1.2. Because the region of high magnetic field, $\sim$ 10 cm long, is smaller than the PR length, then in the PR there exist regions where the magnetostatic field goes to zero or becomes negative. The Microwave can be generated by a **Magnetron**, able to deliver 2.45 GHz microwaves (with 300 W of maximum power) or by a **Traveling wave tube (TWT)**, enabling the generation of microwave frequencies in the range 3-5 GHz. The electromagnetic field created by a generator (magnetron or TWT) is initially delivered, by means of a coaxial cable, to a rectangular waveguide excited in its dominant mode TE_{10}. To ensure stable vacuum conditions during the measurements, it is necessary to place a Kapton sheet, $50\mu m$ between the waveguide and the windows located at the injection endplate of the plasma chamber. The Kapton sheet closes the cavity while maintaining the vacuum and allowing the microwaves to penetrate without alteration. When operating at 2.45 GHz, $B_{ECR} = 875G$ and ECR can occur in two different surface. For microwave frequencies larger than $\sim 2.8GHz$, the condition $B = B_{ECR}$ can not be satisfied in PR, and E.M field can not directly transfer energy to the electrons. Such a configuration is the ideal one for studying new plasma

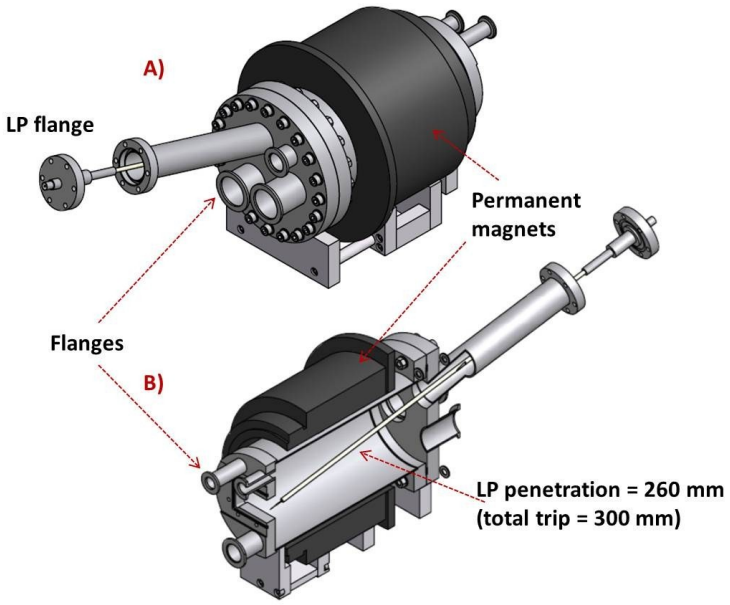

Figure 4.1.1: Render view of the plasma reactor.

heating methodics, in particular for the study of generation and absorption of Bernstein waves.

The permanent magnets position is not fixed w.r.t. the plasma chamber; they can be moved thus leading to different magnetic configurations. Ancillary equipment is essential to the correct operation of PR and they are connected to the PR by means of the six flanges previously shown. The low operative pressure ($10^{-4} - 10^{3}$) is obtained by means of rotative and a turbo-molecular pumps. A full range vacuum gauge allows to measure the neutral pressure in the chamber. The connection between the gas cylinder and the flange of the PR is done through a micrometre valve allowing a gradual gas fluxing, or the slowly return to the air. Furthermore the DN 40 flange has been prepared to enable a CCD camera to obtain images in the visible domain of the plasma, and to mount of a X ray detector to obtain the spectrum of the plasma X-rays emission.

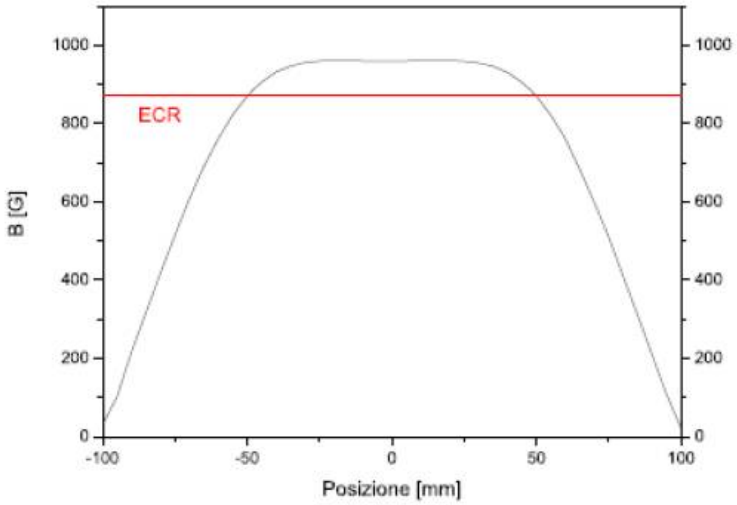

Figure 4.1.2: Plasma reactor magnetic field.

4.2 The Versatile Ion Source (VIS)

The Versatile Ion Source (VIS)[70] is based on permanent magnets producing an off-resonance microwave discharge at 2.45 GHz. It operates up to 75 kV without a bulky high voltage platform, producing several tens of mA of proton beams. The VIS source ensures long time operations without maintenance and high reliability in order to fulfil the requirements of the future accelerators. A render view of the VIS source is shown in figure 4.2.1. The construction of this source comes from the experience obtained through the TRIPS project [72]. Compared to this, VIS presents a much more simplified extraction geometry and movable permanent magnets. All the devices for the remote control were placed at ground potential, thus leaving only the plasma chamber and the permanent magnets at high voltage; the compact dimensions have also helped to get a better and easier maintenance.

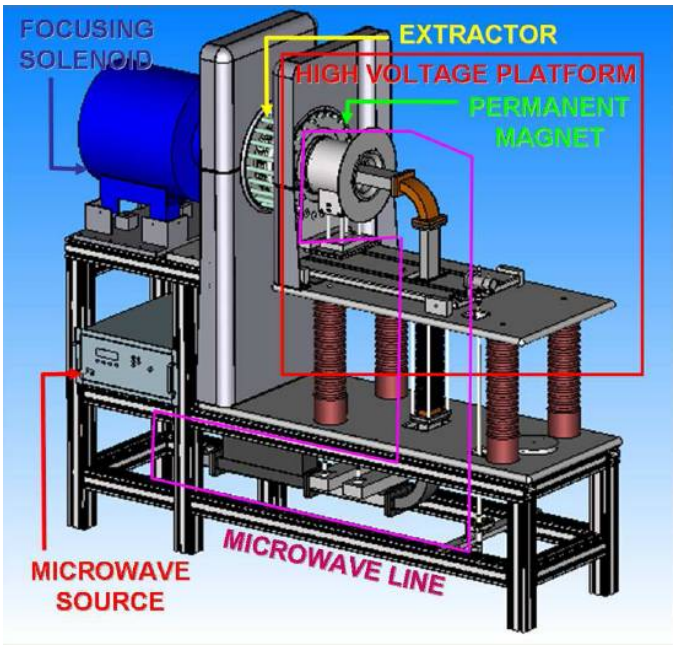

Figure 4.2.1: A render view of the VIS source together with the focusing solenoid.

Microwave System

The microwave line, in figure 4.2.2, is the result of an optimization study carried out with tools for high frequency structures simulation in order to reduce the microwave losses, simultaneously with an adequate matching of the waves to the plasma chamber. A plasma is generated by means of the microwaves provided by a 2.45 GHz Magnetron through a WR 340 (86.4 mm $\times$ 43.2 mm) waveguide excited in the TE_{10} dominant mode. An automatic tuning unit adjusts the modulus and phase of the incoming wave in order to match the plasma chamber impedance with and without the plasma, and a dual-arm directional coupler is used to measure the forward and the reflected power. In order to separate the high voltage region from the grounded one a waveguide DC-break has been designed and realized with the support of HFSS electromagnetic simulator [71]. It is made of 31 aluminum disk of a WR 340 waveguide insulated one each other by means of fiberglass disks. The conductive parts will be fixed to voltages gradually decreasing from 80 kV to ground voltage, still keeping low the insertion loss. The high pressure quartz window is placed before the WR 284 water-cooled copper bend in

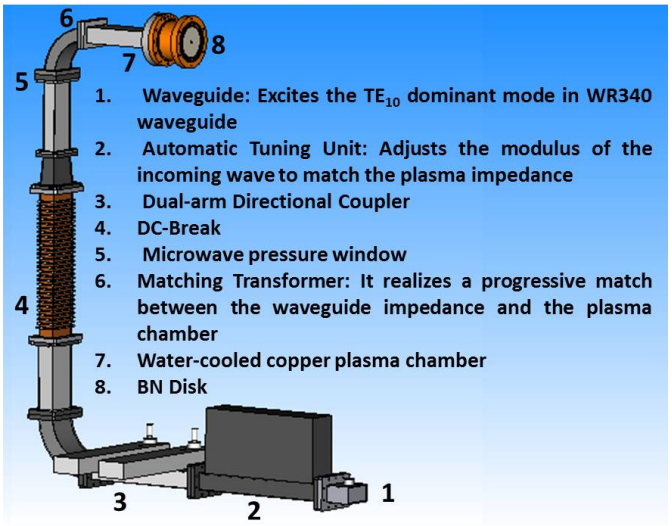

Figure 4.2.2: VIS microwave line.

order to avoid any damage due to the back-streaming plasma electrons. Finally a maximally flat matching transformer has been inserted before the plasma chamber.

The magnetic system

The magnetic system of the VIS source has been designed and realized with the aim to drastically reduce the stray field in extraction region and to avoid the discharges between different electrodes. It consist of a set of 3 Vacodym 745 HR permanent magnets; they are packaged together with two soft iron spacers and supported by a stainless steel tube (figure 4.2.3). The magnets produce an almost flat field profile lower than 0.1 T (see figure 4.2.4). Due to the outer iron components the magnetic field quickly falls off in the extraction region. The resonant field for 2.45 GHz is present in two points along the plasma chamber axis. (As observed for similar ion sources these position, where two BN disks will be placed, are the optimum extremes of the chamber. This feature has been proven to be the best solution to increase the plasma electron density. The magnetic field profile is mechanically tunable by moving permanent magnets with respect to the plasma chamber. Such modification enable us to make possible that

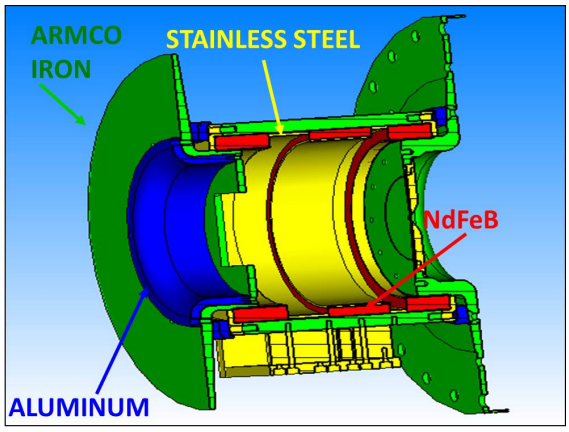

Figure 4.2.3: View of the VIS magnetic system (in red the Nd-Fe-B magnets, in yellow the stainless steel components, in blue the aluminum ones and in green the ARMCO iron parts).

microwave injection occurred in under-resonance or off-resonance positions. The measurements shown in the the next chapter will help to understand how slight modifications of the magnetic induction on injection side can modify strongly the current intensity and affect the emittance of the extracted beam. In figure 4.2.5 the mechanism of magnetic system tuning is shown. In the former the permanent magnets are set at "home" position. In the latter the permanent magnets have been moved toward the injection line.

The plasma chamber

The plasma chamber plays two roles: it couples microwave power to the plasma and it contains the plasma. The source body consists of a water-cooled copper plasma chamber (100 mm long and 90 mm diameter). In order to improve the performance of the source, thick BN plate or Alumina tube can be inserted in the plasma chamber. BN plates are placed at the two extremities of the plasma chamber, one near the maximally flat matching transformer and the other near the extractor electrode, whereas the alumina tube is usually embedded in order to totally cover lateral walls of the chamber. Such materials, being insulators, are able to modify the diffusion rate of plasma decreasing the Simon currents and recovering ambipolar diffusion [83]. In figure 4.2.6 is visible the plasma chamber and the embedded alumina tube. At bottom also the extraction hole is visible. The two small plastic

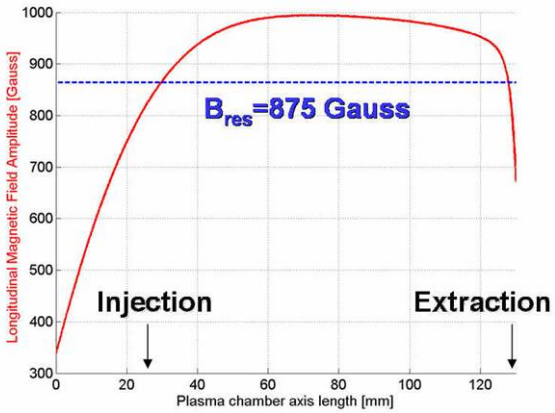

Figure 4.2.4: magnetic field generated by the Nd-Fe-B magnets along plasma chamber axis.

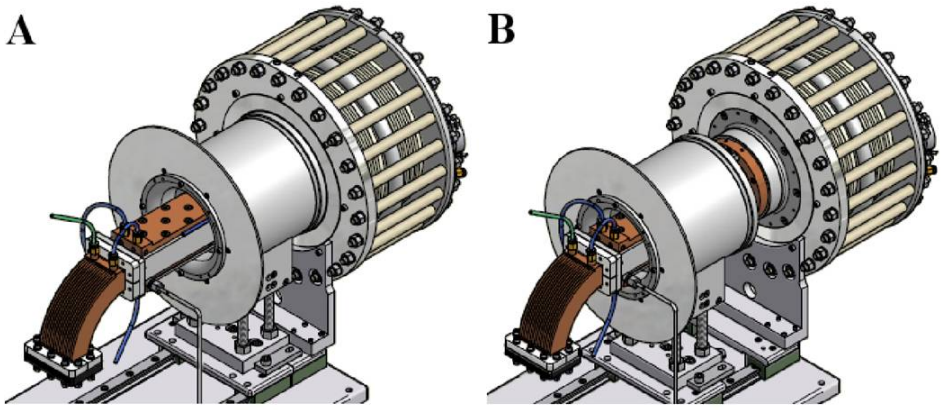

Figure 4.2.5: *A*) Permanent magnets in their "home" position. *B*) Permanent magnets in shifted position.

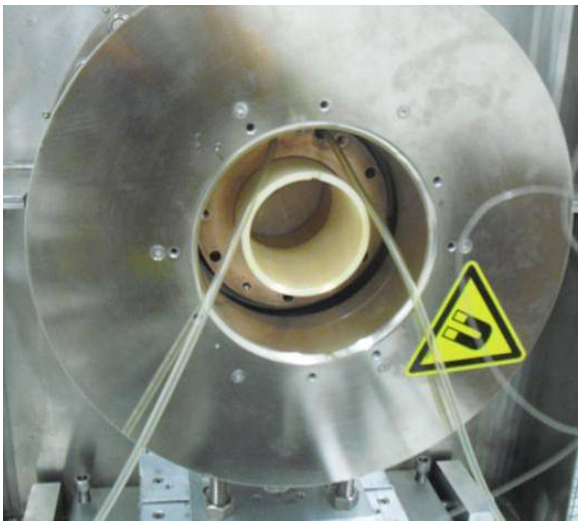

Figure 4.2.6: Positioning of the alumina tube within the plasma chamber. The water-cooling system is also visible.

tubes visible in the foreground constitute the cooling system of the chamber. The low operative pressure of 10^{-4}-10^{-3} mbar in the plasma chamber, and 10^{-5}-10^{-6} mbar in extractor system is obtained by means of rotative and turbo-molecular pumps. The pressure difference in the plasma chamber and the extractor system was obtained because the plasma chamber was evacuated through an hole in the plasma electrode whose dimension can vary from 5 to 10 mm.

The extraction

The ion beam is extracted from the plasma by means of a four electrodes extraction system. The latter consists of a plasma electrode made of molybdenum and usually biased at 65 kV voltage (but able to work up to 75 kV), two water cooled grounded electrodes and a 3.5 kV negatively biased screening electrode inserted between them, in order to repel secondary electrons due to residual gas ionization. In figure 4.2.7 a render view of the plasma chamber and of the extraction system is shown.

The LEBT

The Low energy Beam Transport Line (LEBT) allows the beam analysis and it consists of a focusing solenoid, a four-sector diaphragm to measure the

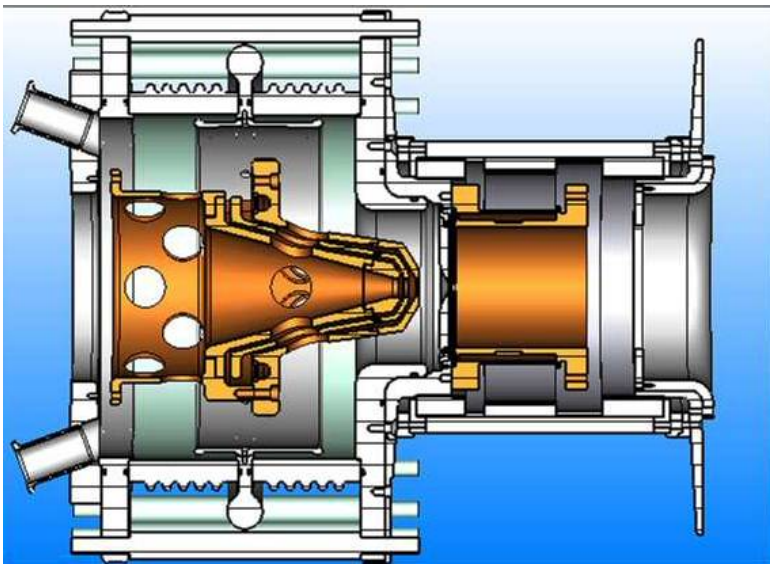

Figure 4.2.7: A render view of the plasma chamber and of the extraction system.

beam misalignments, a Direct-Current Current Transformer (DCCT), a 30° bending magnet and an insulated beam stop to measure the beam current.

4.3 Plasma diagnostics

The Plasma can be characterized with the aid of plasma immersed probes introduced inside or by the analysis of the radiation emitted by free or bounded electrons. Therefore we can distinguish a variety of methodologies such as interferometry, spectrometry and the use of electrostatic probes. We know that the free particles can emit radiation whenever they are accelerate or decelerate; inside the plasma particles are of the same sources of variable fields, so for example an electron moving in the Coulombian field of an ion emit Bremsstrahlung radiation. The radiation, in addition, can also be emitted by bound electrons that give rise to transitions between the energy levels of the atoms or molecules. The characteristic wavelength of the scattered radiation is used to identify the atomic composition and molecular plasma, while the emission intensity is proportional to the density of excited states. The plasma diagnostic can be roughly divided into two groups:

- Non-invasive diagnostics (optical spectroscopy, Thompson scattering, X spectroscopy);

- Invasive diagnostic made by means of electrostatic probes (Langmuir Probe);

The invasive diagnostic measures locally practically all the plasma parameters we are interesting to, however it can perturb the same parameters we want to know, or can get destroyed by a to energetic plasma (for this motivation this diagnostic is applied only in low temperature, low density plasmas, like the ones generated by MDIS). On the other hand, non-invasive diagnostic, does not allow a local measure of the plasma parameters, then providing only average values of the desired values. Furthermore, different plasma parameters (as the plasma potential, the cold population temperature, the floating potential, ecc.) can not be known by means of non-invasive diagnostics. In this thesis work both types of diagnostics for used to determine plasma parameters:

- An electrostatic probe was introduced into the plasma in order to determine density and temperature of the electronic component, (we will describe it in the next section).

- A solid state detector, appropriately collimated and calibrated, has been used in order to characterize the X-ray emission .

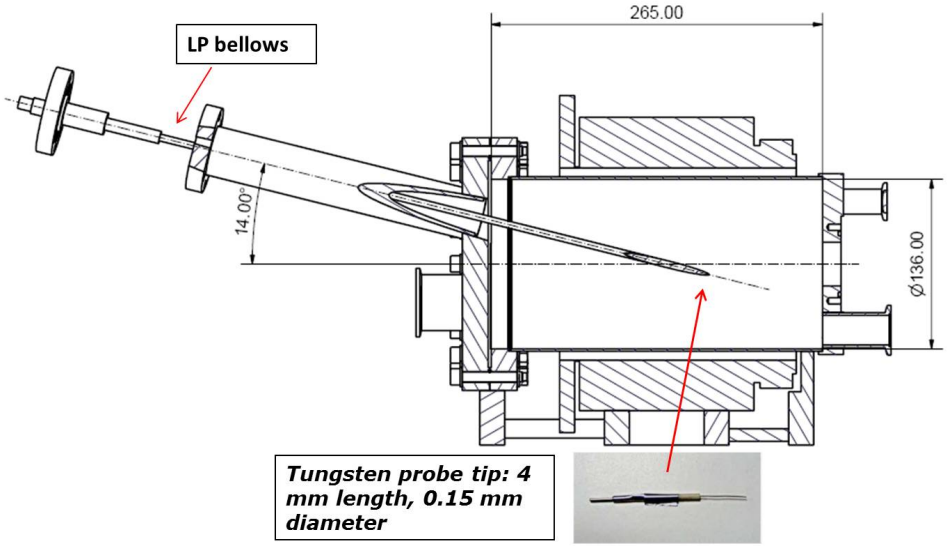

Figure 4.3.1: LP apparatus: the LP penetration axis has a 14° inclination w.r.t. the plasma chamber axis. Its position within the chamber can vary from 0 to 300 mm

4.3.1 Langmuir probe diagnostics

A Langmuir probe is a device so-named after Nobel Prize winning physicist Irving Langmuir, it is used to determine the electron temperature, electron density, and electric potential of a plasma from the resistivity curve. It works by inserting one or more electrodes into a plasma, with a constant or time-varying electric potential between the various electrodes or between them and the surrounding vessel. The measured currents and potentials in this system allow the determination of the physical properties of the plasma. The Langmuir probe used during measurements consists of a tungsten tip with a diameter of 0.15 mm and a length (which can be adjusted varied) of 0.4 mm. These dimensions are important for the analysis of the characteristic curve, since the diameter of the tip must be compared with the Debye length. The tip, inserted in a tungsten core coated by alumina, is then connected to a handling system via a bellows as shown in figure 4.3.1. Its position within the chamber can vary from 0 to 300 mm, with an inclination of 14° w.r.t. to the plasma chamber axis, in order to cover the entire length crossing the center.

During the measurements the only information we have is the penetration depth (0-300 mm) of the probe within the plasma chamber. such information does not give any information about the real positioning inside plasma chamber, so it is useful to introduce a relation between the LP penetration depth and a reference system describing the PR. For sake of simplicity, we set the origin of the coordinates in the center of the extraction flange according to figure 4.3.2. The $\hat{z}$ axis is directed along the axis of the chamber, whereas the $\hat{r}$ axis is directed along the radius of the flange. Because of the axial symmetry of the reactor, it is not necessary to introduce the angular coordinate, and the $\hat{r}, \hat{z}$ coordinates are sufficient to describe the system. The relation between the probe reference and plasma chamber reference are:

$$P_{PR}(r) = (P_{LP} - 41)\sin(14^{\circ}) - 37.5 \qquad [mm] \tag{4.3.1}$$

$$P_{PR}(z) = (P_{LP} - 41)\cos(14^{\circ}) \qquad [mm] \tag{4.3.2}$$

where $P_{PR}(r)$ is the position along the $\hat{r}$ axis, $P_{PR}(z)$ is the position along the $\hat{z}$ axis and P_{LP} is the position in the probe reference. The probe position can be manually adjusted through an external graduated scale (with millimeter sensitivity). At home position, i.e. when $P_{LP} = 0$ the tip of LP is placed out of the plasma chamber, inside the LP flanges. Tip penetrates in the chamber only when $P_{LP} = 41mm$.

Plasma parameters can be derived from the resistivity curve I-V of the plasma. As the probe can be inserted within the plasma chamber, electron density and temperature can be characterized point by point by varying the position of the probe (spatially 1D resolved measurements. A typical resistivity curve is shown in figure 4.3.3. For negative values of the probe potential, if the voltage is large enough, almost all electrons will be repelled, and only positive ions will reach the probe. Such region is usually named ion saturation region. The ion saturation current is much lower than the electric one, being proportional to particle velocity. Bohm criterion demonstrates that ion velocity in plasmas is proportional to $\sqrt{T_e/m_i}$. On the contrary, electron velocity in plasmas is proportional to $\sqrt{T_e/m_e}$. As a consequence, the ratio between electron saturation current and ion saturation is expected to be of the order of $\sqrt{m_i/m_e}$. When the negative potential is reduced, the more energetic electrons are able to overcome the potential barrier and begin to reach the probe. So, as the potential increases, a larger number of electrons reaches the probe, leading to an exponential increase of current: such region is usually called retarding potential current. Finally, when probe

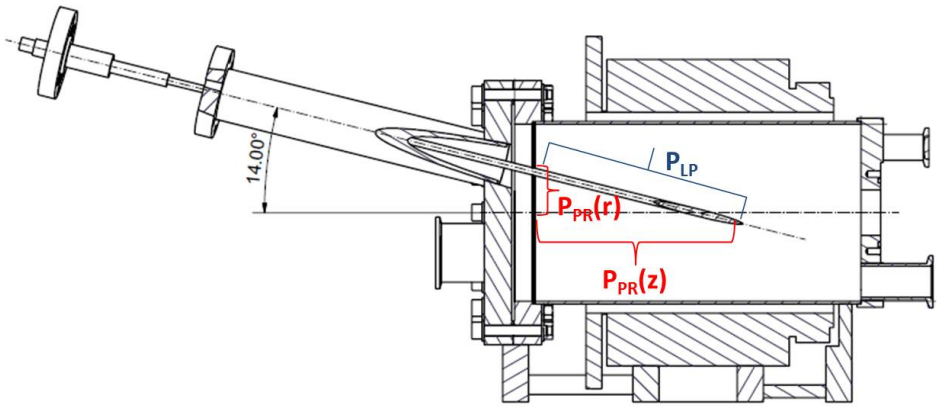

Figure 4.3.2: The simple probe reference P_{LP} does not give information about the 3-D positioning within the plasma chamber. It is hence necessary to use equations (4.3.1) to pass from the Lp reference to the Plasma chamber one.

potential becomes larger than plasma potential, current does not longer increase exponentially and it saturates. Plasma potential represents the potential assumed by the plasma because of the different mobility of the particles, ions and electrons. Because of the faster diffusion of electrons, plasma potential is positive, usually placed in the range 10-30 eV.

The transition from the I.V. curve directly obtained from the measurements to the evaluation of electron density and temperature of plasma is not immediate and requires the implementation of specific theoretical models which are helpful in data analysis. Several model attempted to describe the capture of charged particles by a charged probe [74]. At the moment, the most complete LP theory is that of Lafambroise [75], however, such approach requires a long calculation time. An useful alternative is given by Orbited Motion Limited model [78]. This theory was originally proposed by Mott-Smith and Langmuir: they considered the particles orbiting within a region in which the plasma is characterized by space charge (i.e. the quasi-neutrality is violated): this region is defined sheath, extending several Debye lengths and completely surrounding probe. They assumed that the potential difference between the probe and the plasma was confined within the sheath, so that outside the system could be considered undisturbed. Different works [76]-[77] show that OML is correct in the limit of vanishing probe

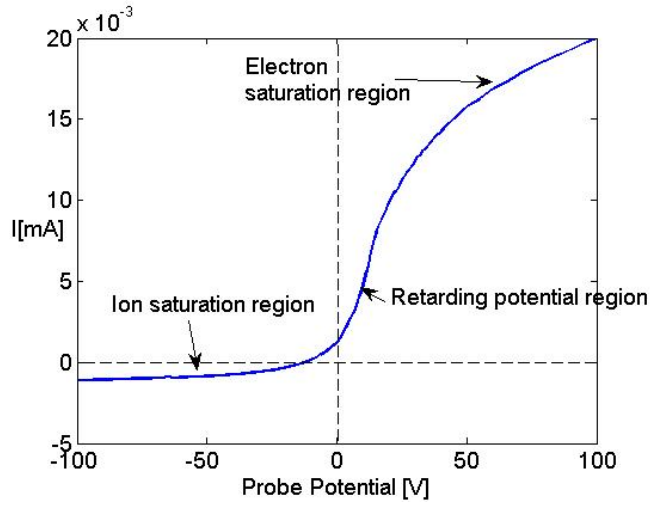

Figure 4.3.3: Typical resistivity curve of a plasma.

radius, i.e when the ration between probe radius and Debye length goes to zero and then, for common experimental plasmas, OML is an excellent approximation for quantitative calculations.

4.3.2 OML approach

Let us examine how charged particles (ions and electrons) are attracted by a cylindrical shaped probe, when affected by an attracting potential, in conditions of saturation current. If the length of probe is much larger than its radius, then the particle will move in a central potential. Solving the problem for electrons, we can write, starting from conservation of energy and angular momentum:

$$\frac{1}{2}mv^2 = \frac{1}{2}mv_p^2 - eV_p; \qquad mvh = mv_p r_p \tag{4.3.3}$$

where v_p is the velocity of the electron at the surface of the probe, h is the impact parameter, V_p the probe potential and r_p its radius (figure 4.3.4).

If probe has length l, than that lateral surface is $A = 2\pi r_p l$. The contribution of the current due to the electrons in a narrow range of speed is then given by:

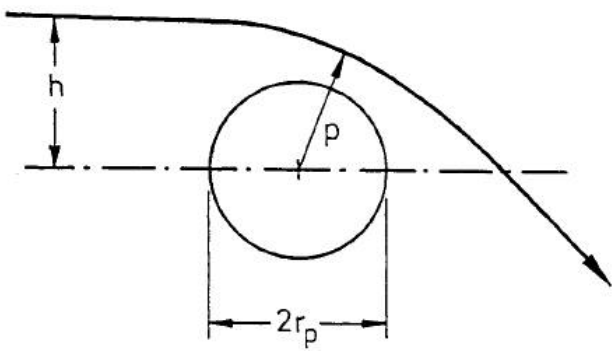

Figure 4.3.4: Diagram illustrating charged particles motion around a charged probe [74].

$$dI = 2\pi r_p l e \left(1 + \frac{V_p}{V_0}\right)^{\frac{1}{2}} \frac{v}{\pi} dn \tag{4.3.4}$$

where the quantity $\frac{v}{\pi}dn$ represents the flux crossing a unit area when considering electrons moving in planes perpendicular to the probe axis. We are not interested in velocity components parallel to the axis. If we consider a Maxwellian distribution (for a distribution at temperature T) of velocities and integrate on the velocity, we finally obtain:

$$I = 2\pi n_e r_p l e \left(\frac{T}{2\pi m}\right)^{\frac{1}{2}} \frac{2}{\sqrt{\pi}} \left(1 \pm \frac{eV_p}{T}\right)^{\frac{1}{2}} \tag{4.3.5}$$

Equation (4.3.5) includes also the "ions" case. The positive sign is related to electron current, while the negative one is related to the ion contribution. Equation (4.3.5) tell us that in the current saturation regions, $I \propto V^{\frac{1}{2}}$. The proportional constant depends on the plasma density. Therefore, by the calculation of the slope of the I-V curve in these regions is possible to calculate the density. In practical cases we only use the ion part of the resistivity curve, because the electron part is often strongly affected by diffusion mechanisms and the magnetic field. In figure 4.3.5 a typical fit of I^2 versus V in the ion saturation region is shown. The extremes of the fit are taken in order to avoid any influence coming from of the electrons contribution. Once know the first derivative of the fitting curve is therefore

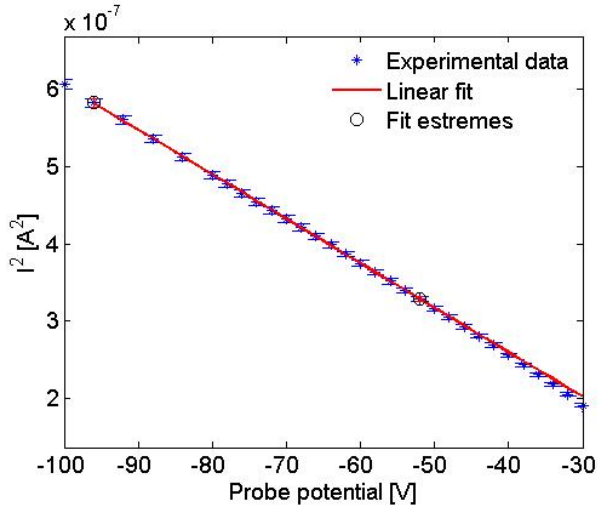

Figure 4.3.5: Plot of V versus I^2. The dependence is linear and the slope of the curve is proportional to the ion density.

possible to perform the calculation of ion density[1]:

$$n_i = \left[\frac{m\pi^2}{2Ae^2}\left(\frac{dI^2}{dV_p}\right)\right]^{\frac{1}{2}} \tag{4.3.6}$$

In the retarding potential regime, only those electrons with an energy greater than $(-eV_p)$ can reach the probe. In such condition equation (4.3.5) is thus modified and becomes:

$$I = 2\pi n_e r_p l e \left(\frac{T}{2\pi m}\right)^{\frac{1}{2}} e^{\frac{V_p}{T_e}} \tag{4.3.7}$$

The logarithm of the current, in the retarding potential region, is therefore proportional to V_p and inversely proportional to the electron temperature. By fitting the curve logarithm is therefore possible to obtain the temperature. In facts from 4.3.7 we obtain:

$$T_e = \frac{1}{\frac{d\ln I}{dV_p}} \tag{4.3.8}$$

[1]The plasma is quasi-neutral, thus ion density and electron density equalize each others.

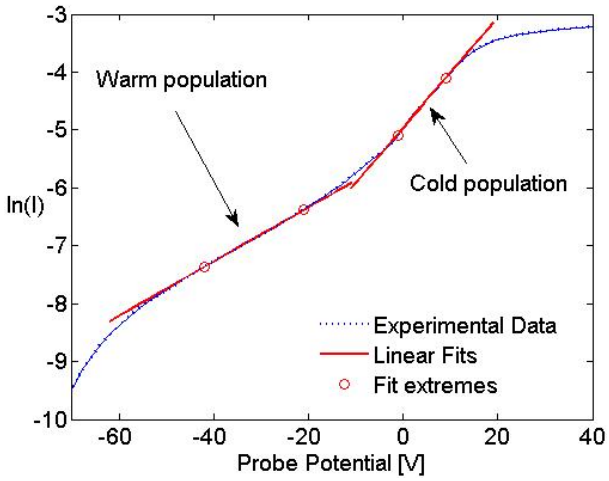

Figure 4.3.6: The plot of $\ln I$ versus V in retarding potential region shows two different electron populations. The slope of the curves is inversely proportional to the temperature.

As it was introduced in section 1.2, in plasma different electron populations coexist. This occurs also in MDIS plasmas, which are often characterized by two or more different electron populations, each one with an own temperature. In particular, this occurs in plasma region where electrons have some resonance. In these regions a part of the electron population absorb stochastically energy from the waves increasing its temperature. In such conditions two different maxwellian distributions can be found by means of LP diagnostic. Unfortunately electrons having an energy larger than the maximum probe potential (100-200 V) can not be collected by the probe, so in general the hotter electron population is generally not detectable by LP diagnostic. Double electron populations are easily identifiable In I-V curves by looking at different different slopes in the of the curve logarithm as shown in figure 4.3.6.

Electron Energy Distribution function

Druyvesteyn [79] has shown that the Electron Energy Distribution Function of an isotropic plasma is directly proportional to the second derivative of the characteristic curve of a cylindrical probe in the region of retarding potentials:

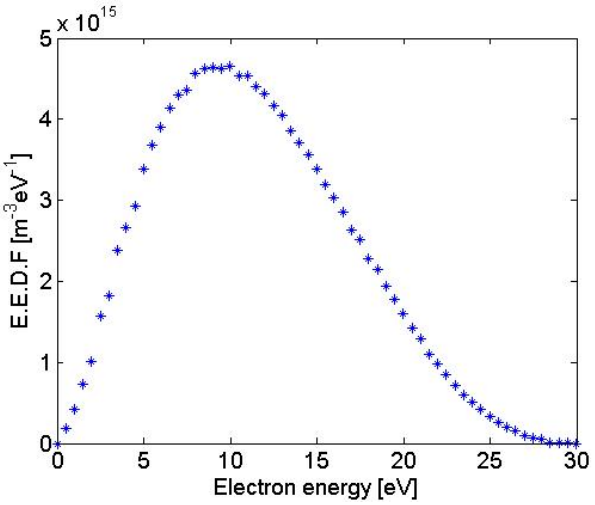

Figure 4.3.7: Electron energy Distribution fraction obtained by double differentiating the I-V curve in the retarding potential region

.

$$\frac{dn_e}{dE} = \frac{4}{A_p e^2}\sqrt{\frac{m(V_0 - V_p)}{2e}}\frac{d^2I}{dV^2} \tag{4.3.9}$$

where V_0 is here the plasma potential, V_p the probe potential and E is the electron energy in the energetic reference of the plasma, i.e $E = e(V_0 - V_p)$. The main limitation of this method is due to the double derivation of the I-V curve. In particular, small fluctuations in the curve slope, negligible for the calculation of parameters such as density or temperature, can be amplified by the double derivation. To avoid this inconvenience, it is therefore necessary to smooth the curve before performing the double derivation.

Electron density can be easily obtained from the previous equation:

$$n_e = \int_{V_0}^{\infty}\left(\frac{dn_e}{dE}\right)dE \tag{4.3.10}$$

An example of EEDF obtained by means of equation (4.3.10) is shown in figure 4.3.7.

4.3.3 X-ray diagnostics

High-energy plasmas represent a formidable emitting device of electromagnetic radiation, from the visible to UV up to the X-rays. MDIS are typically unable to produce electrons above 100-200 eV of energy, therefore their emitting spectrum is made essentially by optical and UV bands. However, the plasmas investigated in this thesis have been produced by an innovative mechanism whose heating efficiency is expected to produce hot electron tails well above 1 keV. The measurements of X emission will be therefore a fundamental operation to describe and characterize the plasma. The X-ray emission is due to the collision of energetic electrons with ions or with the chamber walls. The violent deceleration causes the electron to emit X radiation via bremsstrahlung . X rays spectrum contains all the information on the energetic distribution of the electrons which generated it. The differential bremsstrahlung cross section for an electron colliding with a nucleus of charge Z and emitting a photon of energy $\hbar\nu$, for non-relativistic energies (i.e. $T_e \ll 500keV$), is given by the following formula [80]:

$$\frac{d\sigma_k(\hbar\nu)}{d\hbar\nu} = \frac{16\pi}{3\sqrt{3}}\alpha^3 \left(\frac{\hbar}{m_e c}\right)^2 \left(\frac{c}{v_e}\right)^2 \frac{Z^2}{h\nu} \tag{4.3.11}$$

where v_e is the electron speed, α is the fine structure constant, c is the speed of light, and m_e is the electron mass. In an ECR plasma, bremsstrahlung cross section is measured from the emissivity density $J(h\nu) = h\nu N(h\nu)$, where $N(h\nu)$ is the plasma spectral function that represents the total number of photons of energy $h\nu$, emitted by the plasma per unit of time, volume, and energy. Both J and N are related to the bremsstrahlung cross section and to the ion and electron densities N_i and N_e by means of:

$$J(h\nu) = N_i N_e h\nu \int_{h\nu}^{\infty} \frac{d\sigma_k(\hbar\nu)}{d\hbar\nu} v_e(E) f(E) dE \tag{4.3.12}$$

Here $f(E)$ is the electron energy distribution and $v_e(E)$ the speed of an electron of energy E. For integrating equation (4.3.12) it is necessary to know the electron energy distribution. In ECRIS plasma, electron energy usually distribute following one or two Maxwellian distribution. In the case of the Maxwellian distribution without relativistic effects, by using Kramer's cross section, the integral in Equation (4.3.12) is elementary solved and gives out the theoretical value of $J(h\nu)$:

$$J_{theor}(h\nu) = N_i N_e (Z\hbar)^2 \left(\frac{4\alpha}{\sqrt{6m_e}}\right)^3 \left(\frac{\pi}{T_e}\right)^{\frac{1}{2}} e^{-\frac{h\nu}{T_e}} \tag{4.3.13}$$

Here, T_e is expressed in eV. $J(h\nu)$ is experimentally determined by measuring the spectra $N^{ch}(h\nu)$ corresponding to the number of counts per channel accumulated in an integration time t on detector intercepting a solid angle Ω [82]:

$$J_{exp}(h\nu) = h\nu \frac{N^{CH}(h\nu)}{\eta(h\nu)t} \frac{4\pi}{\Delta E \Omega} \tag{4.3.14}$$

where $\eta(h\nu)$ is the efficiency of the experimental apparatus for an x ray of energy $h\nu$, E is the energy interval corresponding to a channel, and V is the portion of the plasma volume seen by the detector. By setting $J_{exp}(h\nu) = J_{theor}(h\nu)$, if Ω, V and if the instrumental efficiency $\eta(h\nu)$ are known, it is then possible to obtain T_e and the product $N_i N_e$. In facts, by making the natural logarithm of equations (4.3.13) and (4.3.14) one finally obtains:

$$\ln[J_{exp}(h\nu)] = \ln\left(3.84 \cdot 10^{-29} \cdot \frac{N_i N_e Z^2}{t\eta(E)V\Omega(T_e)^{\frac{1}{2}}}\right) - \frac{E}{T_e} \tag{4.3.15}$$

By fitting the X ray spectra with equation (4.3.15), one first can calculate the electron temperature from the slope of the curve, and then, the angular coefficient of the fit gives $N_i N_e$. A second information which can by obtained by the X ray spectrum is the so-called *End point*. Accordingly to 4.3.8 it is intercept between the energy axis and the logarithmic fit of the spectrum. It represents the maximum energy which the system is able to generate. In our analysis, equation (4.3.15) has been used only for the calculation of spectral temperature T_e, while $N_i N_e$ was not calculated. In our device, in facts, we are not still sure about the correct X-ray emission volume V (needed to know density), which depends essentially on the correct knowledge of the region of EBW absorption. As soon as V will be known, X ray analysis will enable us to measure the mean electron density.

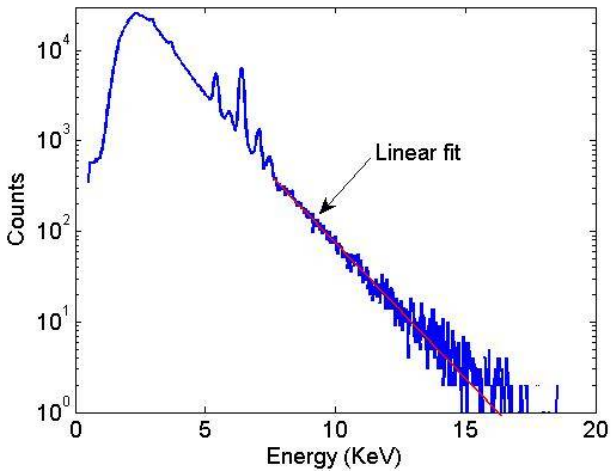

Figure 4.3.8: typical X ray spectrum in logarithmic scale obtained during the experimental measurements. From the slope of the numerical fit the hot electron temperature can be obtained.

4.3.4 X-radiation detectors and experimental setups

The X radiation emitted by the plasma has been detected by means of different devices:

- **A HPGE** (High Purity Germanium) semiconductor detector for the detection of x-rays;
- **A SDD** (Silicon Drift Detector) detector for the detection of x-rays (complementary to the first one);
- **An X-rays pin-hole camera coupled to a CCD** for X-rays imaging;

The HPGe

The HPGe semiconductor detector is produced by the company EURYSIS MEASURES (Mod. EGX.30). It is equipped with of a preamplifier EURYSIS type Pulse-Reset (model PSC854) and with a cryostat (model SBF00-PA3) having 2 days autonomy. The germanium crystal is inserted inside a cylindrical aluminum capsule (electrically isolated) having a diameter of 26 mm and a length of 100 mm. Its high resolution, $\sim 200eV$,

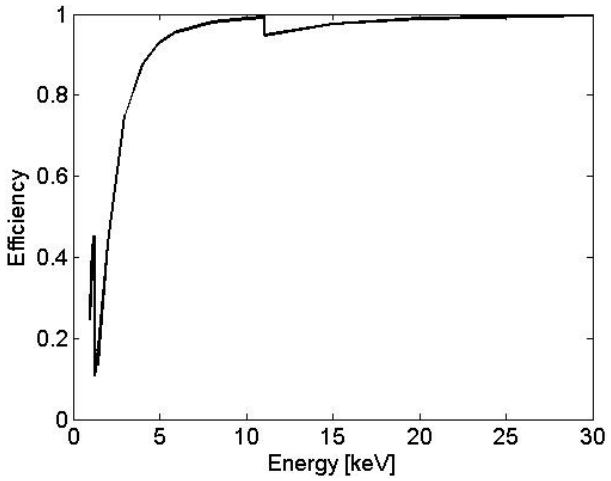

Figure 4.3.9: Efficiency of the HPGe detector used in the experimental campaign

enables to distinguish X sources very close in energy. The efficiency η can be calculated by means of the following formula:

$$\eta(E) = \frac{1}{e^{(\mu_{Be}\delta_{Be}+\mu_{Ge}S)}}\left(1 - \frac{1}{e^{\mu_{Ge}\delta_{Ge}}}\right) \tag{4.3.16}$$

where $\delta_{Be} = 8 \cdot 10^{-4}$ is the thickness of the beryllium window, $\delta_{Ge} = 4 \cdot 10^{-4}$ is the thickness of Germanium crystal, S=0.4 cm is the thickness of the dead layer and finally $\mu_{Be} = \mu_{Be}(E)$ and $\mu_{Ge} = \mu_{Ge}(E)$ are respectively the coefficients of massive absorption of Beryllium and Germanium, and they depends on the electron energy. In figure 4.3.9 the HPGe detector efficiency η is shown.

X radiation measurements have been carried out on external beam extracted from the plasma chamber through a Kapton window of $8\mu m$ thick. Furthermore, in order to reduce the rate of counts incidents on the detector, the X beam extracted from the chamber was further collimated by a bronze 1mm collimator, 5mm thick, as schematically shown in figure 4.3.10.

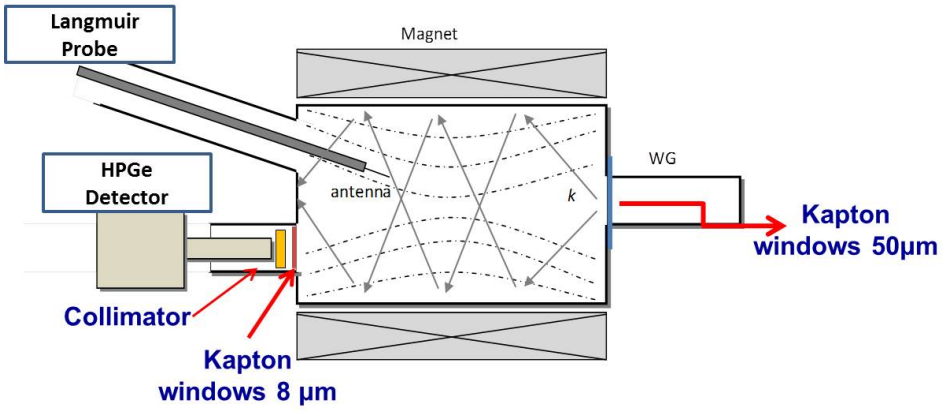

Figure 4.3.10: Experimental set-up of measures carried out with HPGe detector.

The SDD

Part of X radiation measurements has been carried out by means of a SDD detector (Silicon Drift Detector) produced by KETEK, able to reveal X radiation in the range 2-30 keV. Furthermore it is possible to obtain high energy resolution (equal to 160 eV at the reference line of 5.9 keV) and at the same time operate with a high counting rates (up to 500 kcps). Its efficiency curve is shown in figure 4.3.11: it reaches the maximum between 4 and 10 keV.

The detector SDD was assembled similarly to the HPGe along the flange (DN63) in the front part of the Plasma Reactor as shown in figure 4.3.12. A schematic representation of the experimental set-up is shown in Figure 4.3.13; also in these measurements a $8\mu m$ thick Kapton window and a bronze 1mm collimator (5mm thick) where used.

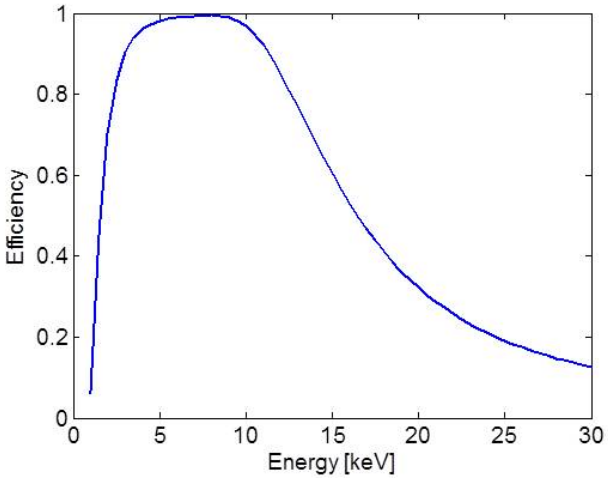

Figure 4.3.11: Efficiency of the SDD detector.

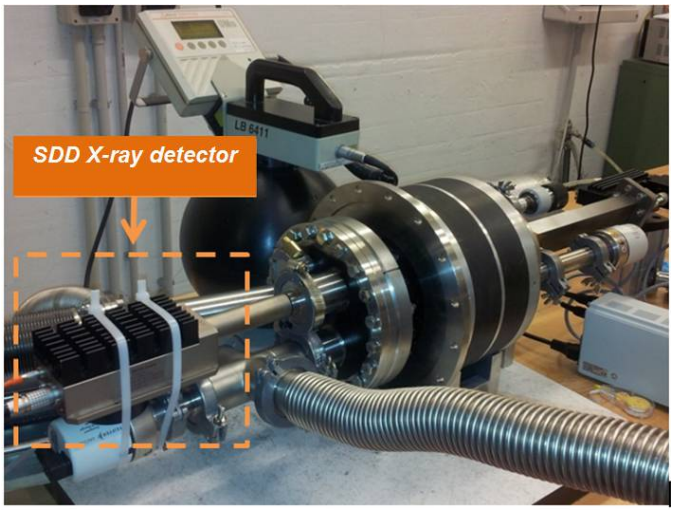

Figure 4.3.12: Experimental set-up of measures carried out with SDD detector.

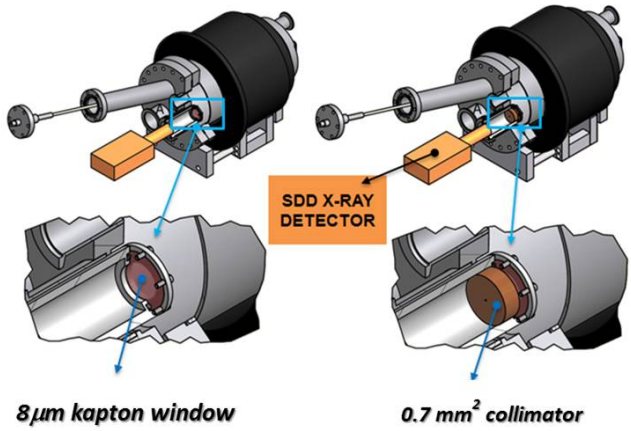

Figure 4.3.13: Focus on the kapton sheet and 1mm collimation positioning during experimental measurements carried out with SDD detector.

The CCD and the pin-hole camera

A X-rays pin-hole camera allows the formation of images through the use of a small circular aperture (pin-hole) having the function of lens for E.M radiation with wavelength smaller than 20 nm (about 60 eV). Figure 4.3.14 illustrates the typical geometry of a pinhole camera, the image of a point object is a disc on the image plane, which dimensions depend on the geometry of the pinhole camera and in particular on the distance pinhole-object (p), on the distance from the pinhole-image (q) and on the pinhole diameter and thickness.

Pin-hole camera is coupled with a CCD camera, which constitutes the main element and represents the sensitive part of the device. It allows to detect X-rays emitted from the plasma in energy domain 1-30 keV. It is produced by the company ANDOR, IKON Model DO934-M BR-DD (Fig. 3 7) [81]. It consists of a chip of active surface of $13.3 \times 13.3\ mm^2$, divided into 1024×1024 pixels of epitaxial silicon, each of the lateral dimension of $13.3\ \mu m$. The CCD is cooled by a Peltier thermoelectric device which allows to operate down to -100°C, when working with activated water recirculation. The quantum efficiency (QE) has fundamental importance because it allows to deduce the probability that the incident radiation is absorbed. In figure 4.3.15 is represented (dashed red), the QE curve of the detector used in these measurements. Finally in figure 4.3.16 the entire experimental set

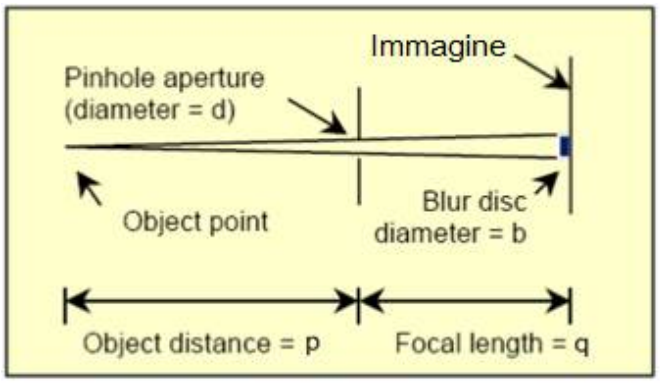

Figure 4.3.14: Generic pinhole camera Diagram.

up is shown: the CCD and pin-holes are placed in the LP flange (LP was removed), the distance between the object (i.e. the plasma X rays) and the pin-hole, P is larger than distance between pin-hole and CCD, Q, consequently the magnification M=Q/P, is smaller than 1 (imagine is smaller than object).

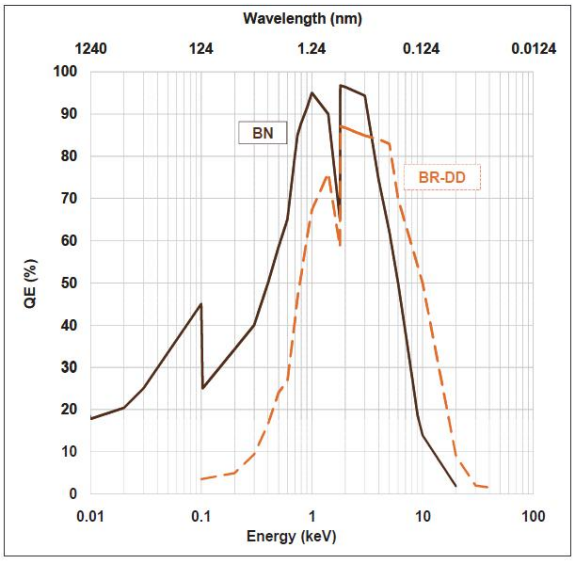

Figure 4.3.15: Quantum efficiency curve (in red).

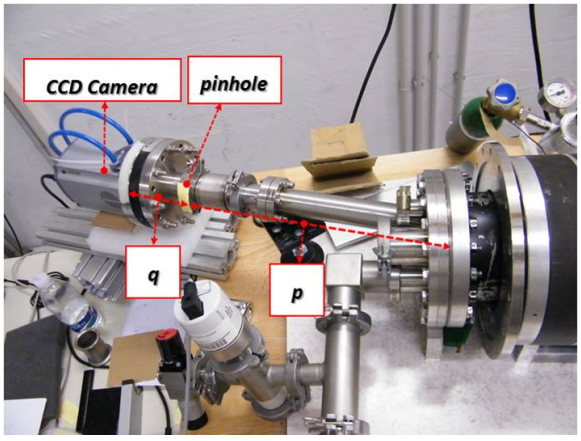

Figure 4.3.16: Pin-hole camera experimental set up. The CCD and pin-holes are placed in the LP flange. P and Q represent respectively the distance object-pin-hole and pin-hole-imagine. In our case Q¡P, so the magnification is negative.

Chapter 5

Plasma heating in higher harmomics

The fundamental purpose of the next pages is to highlight the effects implementation of a new method of plasma heating featuring a strong non-linear behaviour. Experimental evidences are basically consistent with a plasma heating mechanism driven by electron Bernstein waves formation via inner-plasma E.M to E.S mode conversion process. The studies on the modal conversion from Extraordinary to Bernstein wave, and the successive absorption at cyclotron harmonics were carried out on Plasma Reactor (PR) by means of a series of experimental measurements performed in different years. In particular, two magnetic profiles were detailed studied and the effectiveness of EBW heating will be basically demonstrated by find the fingerprints of the EBW heating:

1. *Appearance in the E.M. spectrum of sidebands of the pumping electromagnetic waves in the range of GHz and of ion waves in the range of MHz*;

2. *Generation of high energy electrons*;

3. *Achievement of densities much higher than the density cutoff*;

To avoid the different heating mechanism could operate at the same moment, a large part of the measurements were performed in under-resonance conditions ($B < B_{ECR}$) in order to prevent ECR heating, enabling only EBW absorption at cyclotron harmonics. Further measurements allow to analyze the plasma behaviour when either EBW heating and ECR heating

were present. In one of the studied magnetic configuration, LP measurements makes possible the direct detection of the UHR and the study of its influence on the E.M wave. In second profile, in facts, UHR is not placed along the LP penetration axis, but X ray diagnostic and a ray tracing simulation demonstrate that UHR is placed on the lateral surface of the plasmoid[1]. The measurements of power of E.M field within the plasma chamber in presence of the plasma will enable to describe the modal cavity behaviour of the field in different plasma conditions, and to relate it to plasma parameters. In the second part of this chapter the know-how acquired with PR have been applied on the VIS source. It has been demonstrated that the presence of the UHR in the source causes suprathermal electrons to appear and an increase of the beam emittance is contemporaneously obtained. Finally, measurements carried out on a helium plasma have shown how the plasma energy content is influenced by the generation and absorption of EBW.

5.1 Measurements set-ups

The PR is a really versatile experimental apparatus that allow to prepare different experimental configurations. The permanent magnets are movable with respect to the plasma chamber, while the injected microwave frequency can be varied from 2.45 GHz (when using the magnetron generator) up to 5 GHz (TWT generator). Two main magnetic configuration have been analyzed: the **flat-B field configuration** (figure 5.1.1 (a)), (typical in MDIS), and the **magnetic beach configuration** 5.1.1 (b), In the first configuration, the permanent magnets are symmetrically placed around the plasma chamber. The corresponding flat magnetic field ($\sim 0.1T$) reaches its maximum value in the central regions of chamber 5.1.1 (c); two different groups of resonances (ECR and its harmonics) are placed in the region where magnetic field falls down.

In the second configuration, permanent magnets are shifted towards the injection flange magnetic. in this way, microwave injection occurs in a high B region, while the magnetic field decreases rapidly in the center of plasma chamber. A group of cyclotron harmonics are thereby localized in the central region of plasma chamber. The two chosen field configurations allow the study of EBW heating in opposing and complementary conditions, crucial to determine the best operating conditions for conversion and absorption of electrostatic waves. In each configuration, different microwave frequen-

[1]Since now the plasmoid will be the region of the plasma chamber characterized by the largest characterized by the largest energy content (defined as $n_e t_e$) of the plasma

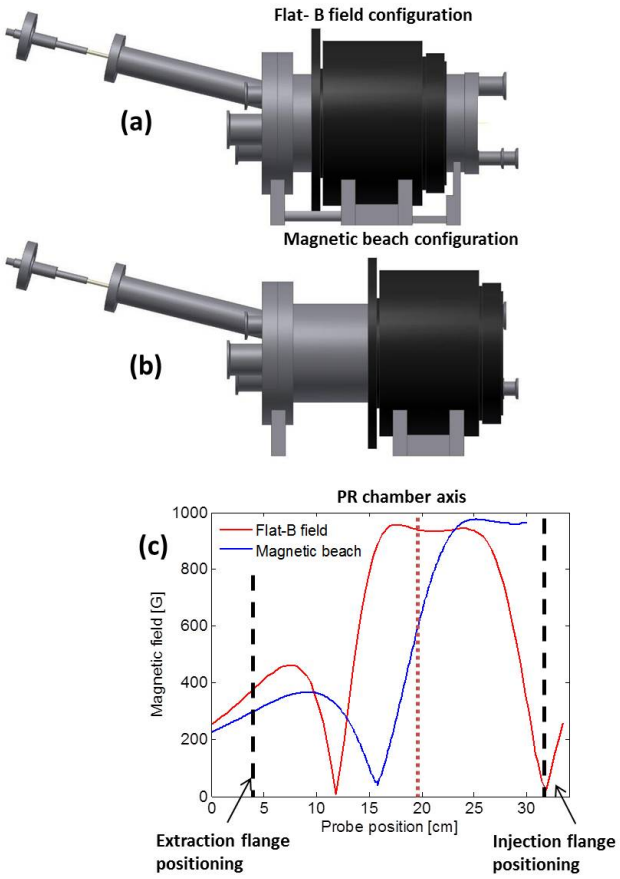

Figure 5.1.1: During measurements, two main magnetic configurations have been tested: the flat-B field configuration, (typical in MDIS) (a), and the magnetic beach configuration (b). In the former the permanent magnets are symmetrically placed around the plasma chamber. The corresponding flat magnetic field ($\sim$ 0.1 T) reaches its maximum value in the central regions of chamber; In the latter permanent magnets are shifted toward the injection flange. Microwave injection occurs in a high B region, while the Magnetic field decreases quickly in the center of plasma chamber (c).

cies have been injected in the plasma chamber. The operating frequencies have been chosen in order to minimize the reflected power to the microwave generator. In particular, in magnetic beach configuration we tested the following frequencies: 3.37 GHz, 3.76 GHz and 4.253 GHz. The best results have been obtained at 3.76 GHz, probably due to a better coupling between the plasma, the cavity, and the microwaves. These results leaded us to perform experimental measurements in flat-B field configuration at the same frequency of 3.76 GHz, after we verified that, even in such magnetic configuration, the microwave power reflected to the amplifier was minimized as well.

5.1.1 Results obtained when using the magnetic beach configuration

As it was explained in the previous section, the operative microwave frequencies used for experimental measurements do not have any ECR resonance within the PR plasma chamber. In figure 5.1.2 a plot of the PR magnetic field together with the field needed to have ECR resonance ($B_{ECR} = m\omega_{RF}/e$) is shown. We are not able the define, "a priori ", before the experimental measurements, where Upper Hybrid Resonance is placed. UHR, in facts, depend either on the operative frequency and on the plasma density (see equation 2.1.29); it would therefore be necessary a self-consistent treatment of electron heating, which takes into account, step by step, how the plasma distributes at different modal configuration within the plasma chamber, and how this in turn affects the plasma distribution. This treatment does not currently exist, so you UHR can be studied exclusively "a posteriori" from the analysis of the electron density distribution. On the contrary, we expect that EBW, if correctly generated by modal conversion at UHR, be absorbed at the cyclotron harmonics, listed in table 5.1. A large part of the energy would be absorbed at the first harmonic, while the portion of EBW able to tunnel this first resonance will be then absorbed at the subsequential harmonics. by virtue of this approach, we expect that the absorption region is enclosed inside the layers corresponding to $\sim 16cm$ and $\sim 21cm$ in the Langmuir Probe reference. Since the LP tip dimension is 4 mm, it is impossible to evaluate the plasma parameters on shorter scale-length.

Measurements have been carried out with a nitrogen plasma at a pressure of $1 \cdot 10^{-3}$ mbar and a fixed microwave power of 30 W. Three different operative frequencies: 3.37, 3.76 .4.254 Ghz has been tested. The first im-

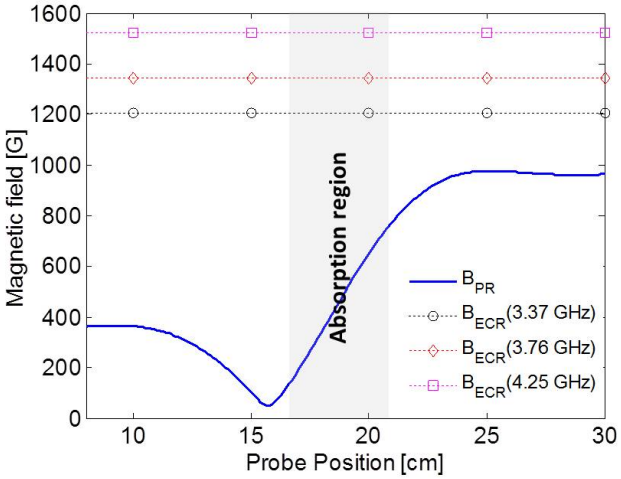

Figure 5.1.2: PR magnetic field together with. The expected absorption region is also shown.

Freq. [GHz]	3.37	3.76	4.253
B_{ECR} [G]	1205	1345	1521
$B_{ECR}/2$ [G]	603	672	760
$B_{ECR}/3$ [G]	401	448	507
$B_{ECR}/4$ [G]	300	336	380
$B_{ECR}/5$ [G]	241	269	304

Table 5.1: Main cyclotron harmonics of the microwave frequencies used in measurements

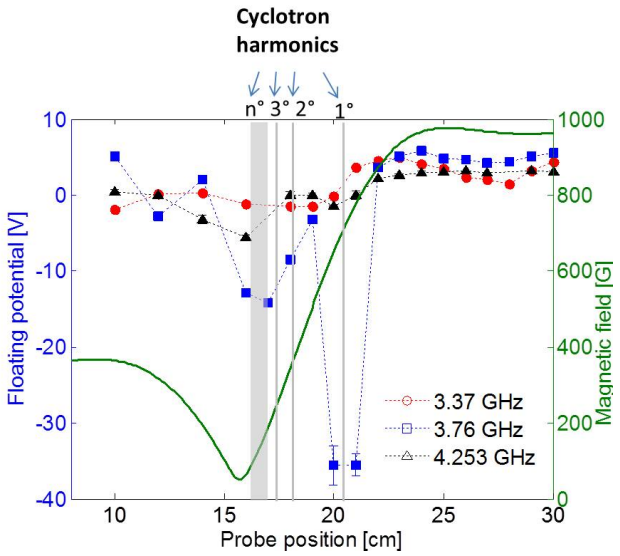

Figure 5.1.3: Trend of floating potential along the LP direction of motion: at 3.76 GHz two deep minima are present in correspondence of the 3.76 GHz cyclotron harmonics (shown in grey).

portant result is given by the plot of the floating potential v_f against the probe position, shown in figure 5.1.3. The Floating potential corresponds to the potential that would be observed by a floating electrode immersed into the plasma. In other words, it corresponds to the potential needed to cancel out the net current of particle arriving on the probe i.e. at floating potential ion current to the probe equals the electron one, i.e $J_i = J_e$. The lower is the floating potential, the higher is the energy of the electron flux, being the probe potential needed for electron reflection more negative with respect to plasma potential. In general, the minima of the floating potential can be related to the presence of energetic electrons and hence, of a resonance. At the frequency of 3.37 GHz and 4.253 GHz, floating potential does not show any evident dependence on the probe position. On the contrary, at 3.76 GHz, v_f has a deep minimum at the probe position of 20 cm and 21 cm (where the first harmonics is placed), and a second minimum is around position 16 and 17, on corresponding to the higher order cyclotron harmonics which, being so close each other, are seen by for the waves a quasi-continuum layer which can not be overcome if absorption occurs.

The plot of electron temperature, shown in figure (5.1.4) confirms what

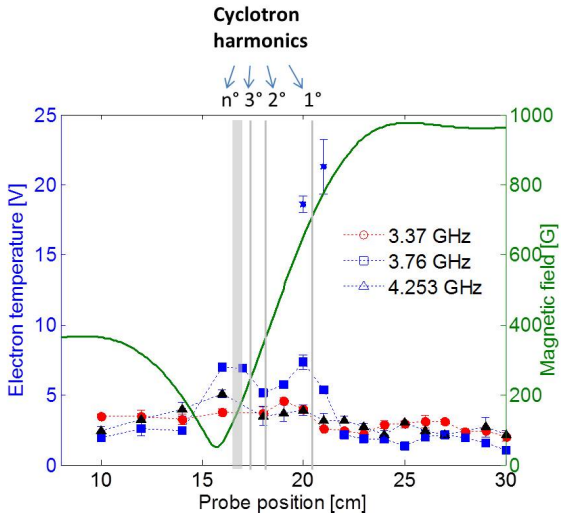

Figure 5.1.4: Trend of electron temperature along the LP direction of motion: better values have been obtained at 3.76 GHz with maxima in correspondence of the 3.76 GHz cyclotron harmonics (shown in grey) and presence of hot electrons ($t_e \sim 20eV$) at an LP position corresponding to the first harmonic.

we said about floating potential: at 3.37 GHz and 4.253 electron temperature varies slightly in the range 2-5 eV with LP position, and no evidences of localized plasma heating appear. At 3.76 GHz two maxima ($t_e \sim 8eV$) are present, in the same positions where the minima of floating potential were placed. In particular at the LP position of 20 and 21 cm, a hotter electron population appears in EEDF, with temperatures which reach $\sim 20eV$. The double electron temperature is a clear evidence that an strong heating mechanism is acting at the first harmonics, consistent with the absorption of EBW.

In figure 5.1.5, the ion density measured for the three microwave frequencies is shown. Higher density values are obtained at 3.76 GHz, however, when the normalized density X=ω_p^2/ω^2 is calculated[2] (figure 5.1.6), it comes out that the best experimental results are obtained at 3.37 GHz, with an ion density exceeding the density cutoff in large part of the plasma chamber. In particular, at the LP position of 26 cm, (where no cyclotron harmonics are present), the value of parametric density X exceeds 2. Interesting

[2]The normalized density measures how much electron density overcomes the density cut-off.

results are obtained also at the frequency 3.76 GHz; larger density values are placed where magnetic fields falls down in the absorption region placed at LP position of around 20 cm. At 4.253 GHz the ion density is lower with respect to the other two frequencies and only for LP positions between 20 and 24 cm parametric density plasma is slightly overdense. These measures highlight one of the main limitations of the diagnostics with Langmuir Probe. The axis of the Langmuir probe crosses only some regions of the source, and one can not determine what happens in the remaining regions. In our specific case, it is not possible to determine if, at a frequency of 3.37 GHz, resonance regions are placed in regions where our LP ca not arrive. Experimental evidences, however, reveal that, at the frequency 3.76 GHz, the LP moves through the resonances, consistently with those that would be expected in the case of EBW heating. For this reason it is extremely interesting to study in more details the results obtained at 3.76 GHz. At this frequency the ion density shows, in coincidence with the first harmonic, at the LP position of 21 cm, a relative minimum of ion density, surrounded by two regions of high density; a similar behaviour can be observed also at the position of 24 cm. Variations of ion densities of similar strength are not found with the other used frequencies.

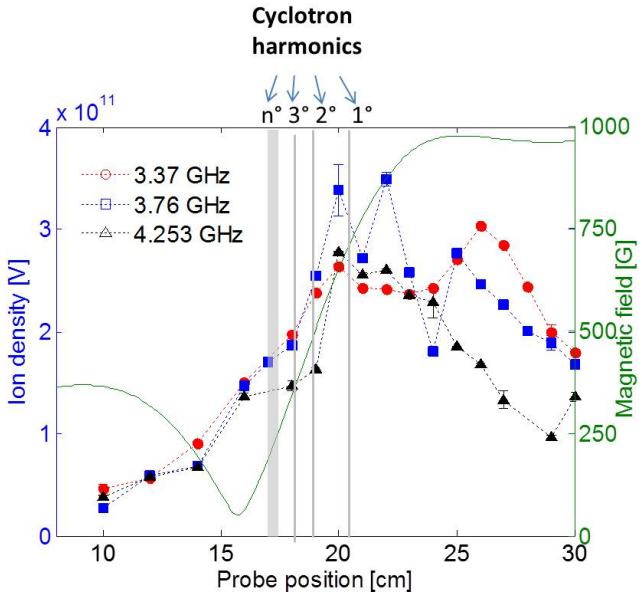

Figure 5.1.5: Trend of ion density along the LP penetration length: ion density up to $3 \cdot 10^{11} cm^3$ has been obtained in all configurations.

In order to clarify this phenomenon, in figure 5.1.7, the ion density calculated from the electron part of the I-V resistivity curve (here normalized w.r.t. the maximum values of ion densities) is shown. We know from section 4.3.1 that the electron region of the resistivity curve is strongly affected by the magnetic field and does not give reliable results. However, even if its absolute value is not realistic, it is interesting to observe its behaviour at different LP positions at 3.76 GHz. In this case the density minima are much deeper compared to the analysis obtained in the ion density plot (figure 5.1.5). Electrons, in facts, enable to observe a finer structure with respect to ions, being their Larmor radius ($\sim 100 - 200\ \mu m$) much smaller than the ion one ($\sim$ 5-10 mm). Therefore ion density average on the scale-length on the Larmor radius, and it is difficult to measure any density gradient acting on distances smaller than 1 cm. Figure 5.1.7 show unequivocally that, in coincidence with the cyclotron harmonics (either the first one and the harmonic wall placed around the LP position 17), plasma is strongly depleted. A third region where the same depletion seems evident is placed at 24 cm, but apparently it has not any physical meaning. In order to clarify the meaning of this plasma density configuration, we calculated from magnetic

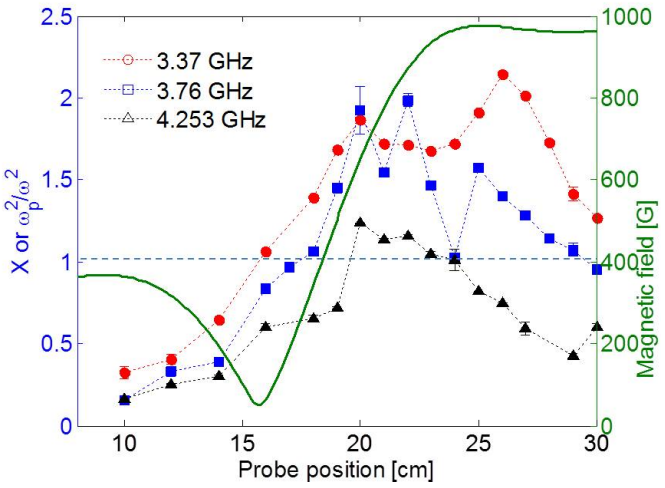

Figure 5.1.6: Trend of parametric ion density (ω_p^2/ω^2) along the LP direction of motion: at 3.76 Ghz end 3.76 Ghz ion density exceeds the cutoff density. The dashed line corresponds to the cutoff density.

field and density profile, the values of the main wave cutoffs and resonances. The results, displayed in figure 5.1.8 show that at position 16, 21 and 24 is possible the Upper Hybrid Resonance; in all the three cases the UHR is embedded between two L cutoffs.

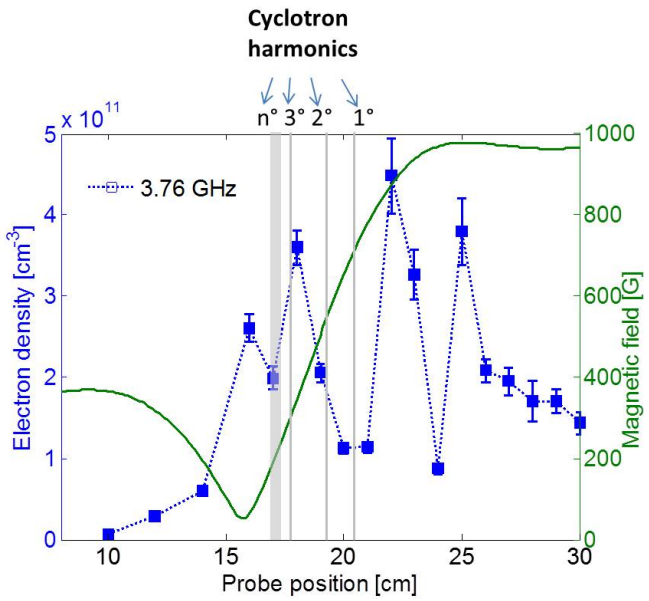

Figure 5.1.7: Trend of electron density along the LP direction of motion at the frequency of 3.76 GHz, normalized w.r.t. the ion density: the figure shows unequivocally that, in coincidence with the cyclotron harmonics, plasma is strongly depleted. A third region where plasma depletion is evident is placed at 24 cm; this region correspond to the Upper hybrid Resonance

.

This result is consistent with the hypothesis that the extraordinary wave can tunnel through one of them, and be reflected back and forth passing through the UHR. This is the best condition for the establishment of the Budden-type conversion scenario introduced in section 2.6.1. However, only two of the resonances are detected in an optimal position for the generation of electrostatic. The electrostatic waves generated at 20 cm can be immediately absorbed at the first harmonic, as well as the electrostatic waves eventually produced at the position of 16 cm, while electrostatic waves generated at the position of 24 cm can not be absorbed by the plasma, because the value of the magnetic field in that position is not optimal (B=1000 G, while $B_{ECR/2}$= 672 G). We can conclude that an optimum condition for generation and absorption of electrostatic waves is that UHR and cyclotron harmonics be placed very close each other along the axial direction as observed in the measurements. This hypothesis can be reinforced other

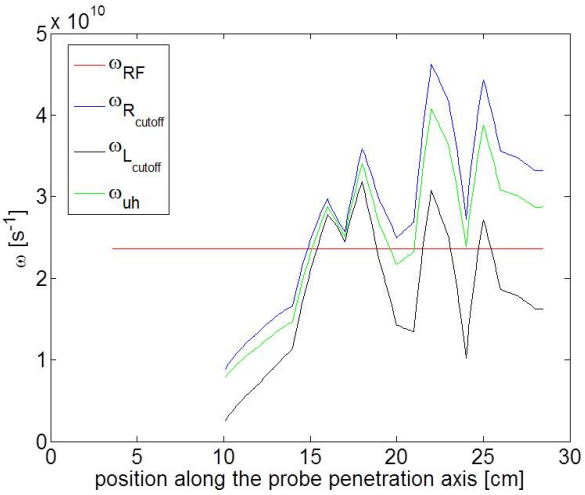

Figure 5.1.8: Refraction index for ordinary and extraordinary modes propagating at different angles.

experimental observations.

The strong fluctuations of ion density have probably some physical reason to exist: only this critical condition can allow the presence of UHR. Let us examine the stability of the conversion scenario: if ion density becomes overdense also in this region, UHR would not exist at all (UHR exist only if $n_e < n_{cutoff}$); furthermore, a so steep density gradient is the optimal condition for X-B conversion. We can make some attempt to evaluate the conversion efficiency. Looking at section 2.6.1, we remember that the conversion coefficient C_{XB} depends on the value of $L_n = n_e/(n_e/x)$ and magnetic field B at UHR. From figure 5.1.7 we can estimate that at the 24 cm UHR, $L_n \sim 1$ cm while B=0.1 T. The from equation (2.6.6) we calculate η:

$$\eta = \approx 294 \left| BL_n \right|_{UHR} = 0.3 \tag{5.1.1}$$

finally from equation (5.1.2):

$$C_{XB} = 4e^{-\pi\eta}\left(1 - e^{-\pi\eta}\right) \cong 0.95 \tag{5.1.2}$$

this means the in this condition X wave have 0.95% probability to tunnel L cutoff and be converted into Bernstein wave, a value exceptionally high. Aniway, in previous equation we neglected the term $\cos^2\left(\frac{\phi}{2} + \theta\right)$ because we

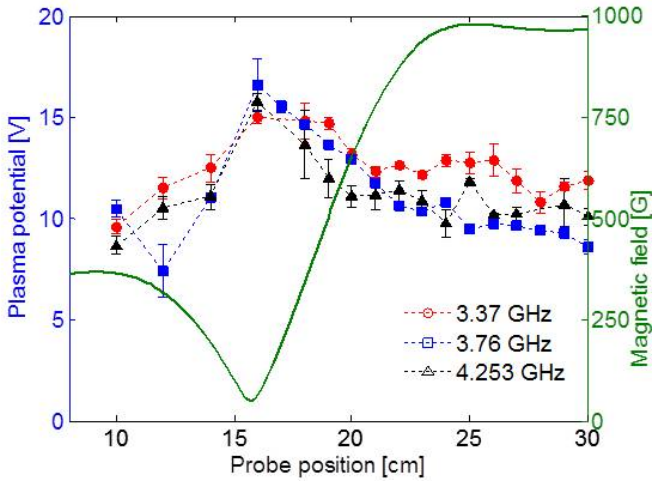

Figure 5.1.9: Trend of plasma potential along the penetration axis og the LP. The maximum visible around position 16 corresponds with the zero of the magnetic field.

are not able at the moment to determine the influence of the phase factors appearing on the global conversion efficiency, and the precise calculations require a more detailed study, which was not in the frame work of the current work.

Figure 5.1.9, illustrates the plasma potential V_p trend against probe position. No significant fluctuations were found, close to the UHR depleted zones. On the other hand, the V_p measurements revealed an expected increase of the potential when approaching regions of low magnetic field, where the escaping electron flux is not mitigated by the Lorentz force. In facts, the maximum visible around position 16 is due to the zero of the magnetic field. In this region, in facts, the conditioning due to the magnetic field vanishes and electrons tends to escape from the plasma. For the quasi-neutrality principle a larger positive plasma potential attracts back the escaping electrons.

5.1.2 The flat-B field configuration

Again in this magnetic configuration the operative frequency has been tuned by searching at the minima of the reflected power to the TWT amplifier. The best performance was found at 3.7476 GHz (in the following we will write 3.75 GHz for sake of simplicity). This frequency corresponds to a B_{ECR} field of 1340 G meaning that the ECR heating is once again forbidden. The magnetic configuration is shown in figure 5.1.10. In this configuration the first harmonic occurs at the position of 14.5 cm and 28 cm. The values corresponding to the cyclotron harmonics are practically the same of the ones calculated at the 3.76 GHz configuration studied in the previous section. Also in this case the EBW absorption is expected to occur at cyclotron harmonics, uncertainty remains for evaluating UHR displacement. Due to the long time required, plasma parameter measurements have been carried out at steps of 2 cm, this implies that the smallest spatial resolution can not exceed 2 cm. This time an insulator was used to protect the TWT from bursts of reflected power. Another improvement in the operative apparatus consisted in a powered pumping system which allowed allowed us to decrease the operating pressure to values of $1 \cdot 10^{-5}$. This enabled to work with a practically pure nitrogen gas at a pressure of $1.5 \cdot 10^{-4}$. Three different microwave power values were studied: 20, 70 and 100 W. Figure 5.1.11 shows the floating potential measured at different positions of LP. As expected, the minima of the floating potential are placed in coincidence of the cyclotron harmonics, according to the hypothesis that heating takes place in such a region. In particular, the first minimum is revealed at 13 cm while the second ranges between 27 cm (20 W), 28 (70 W) and 30 cm (100 W).

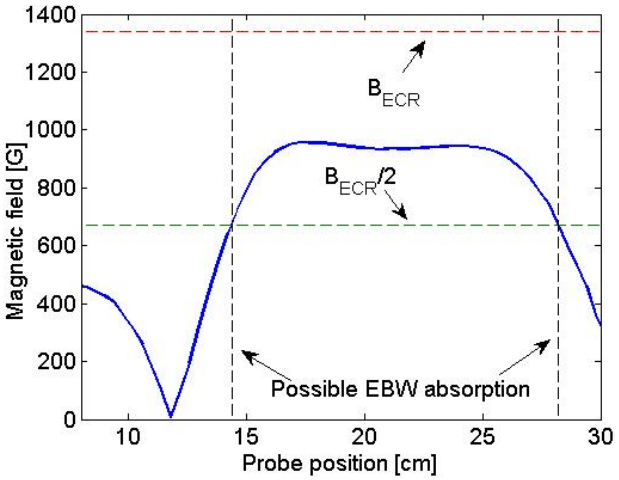

Figure 5.1.10: Magnetic configuration in the plasma chamber of plasma reactor. Only the cyclotron harmonics exist in the chamber.

In figure 5.1.12 the electron temperature is shown. Temperature maxima are again placed in proximity of the resonances of EBW. At the power of 20 W the temperature exceeds the value of 5 eV only at the resonances. Whereas at the powers of 70 and 100 W two electron populations have been revealed in different positions. the colder one has a mean temperature of the order of 10 eV, while the temperature of the warmer population, in proximity of the two first harmonics layers, reaches values higher than 20 eV, meaning that in these positions heating by Bernstein waves has been very effective. At 100 W, in particular, the double electron population has been revealed over the entire Lp penetration path, i.e. even in these positions where EBW absorption is not expected.
In figure 5.1.13 the values of electron density at 3.75 GHz for the three different values of RF power are shown. At 20 W the plasma is underdense GHz ($n_{cutoff} = 1.75 \cdot^{11} cm^{11}$) everywhere in the plasma chamber. At higher power, however, electron density increases beyond the cutoff value and, at 100 W, it reaches $8 \cdot 10^{11} cm^{-3}$, a value five times larger than the cutoff density. To better put in evidence the formation of the overdense plasma in figure 5.1.14 the normalized density has been plotted. In particular at 70 and 100 W, plasma is overdense everywhere along the LP penetration axis. Furthermore, at 100 W the mean value of electron density along LP axis overcomes $5 \cdot 10^{11} cm^{-3}$, a value three times larger than cutoff den-

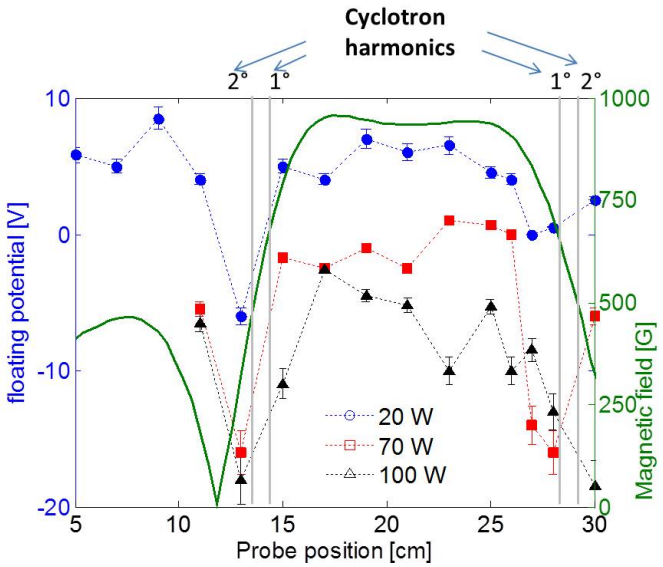

Figure 5.1.11: Floating potential and magnetic field profile at $1.5 \cdot 10^{-4}$ mbars, 3.75 GHz frequency. The minima of the floating potential are placed in coincidence of the cyclotron harmonics

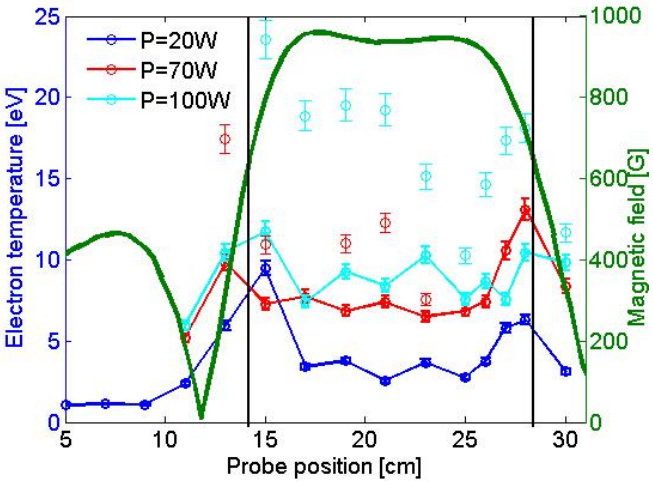

Figure 5.1.12: Electron temperature and magnetic field profile at $1.5 \cdot 10^{-4} mbars$, 3.75 GHz frequency. At 70 and 100 W double electron population is present.

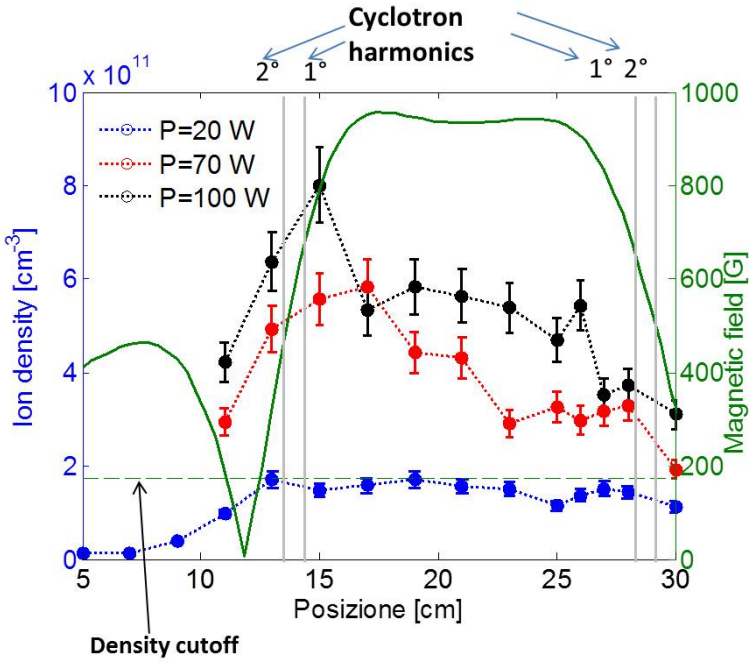

Figure 5.1.13: Electron density and magnetic field profile at $1.5 \cdot 10^{-4}$ mbar, 3.75 GHz frequency.

sity. Electron density is picked at the cyclotron harmonic placed at 15 cm. A question arises: can extraordinary wave propagate inside a plasma of so large density? This issue is relevant, in facts, even if the plasma is generated by means of Bernstein waves; it is at least necessary that the extraordinary waves penetrate the plasma to be converted at UHR to EBW. The calculation of the refraction index for different incidence angles shows that the refraction index of ordinary and extraordinary wave is lower than zero, i.e. the entire region spanned by the probe is forbidden to the E.M waves propagation. In figure 5.1.15 the refraction index calculated at $\theta = 90^{\circ}$ is shown; similar results can be found for every incidence angle. The possible solution of this paradox will be found in section 5.2.1.

Another interesting information obtained by the LP diagnostic attains the Electron Energy Distribution Function (EEDF). In ECR plasmas EEDF has the shape which was shown in figure 4.3.7, i.e. energies usually follow a Maxwellian function. In some case the distribution plotted in logarith-

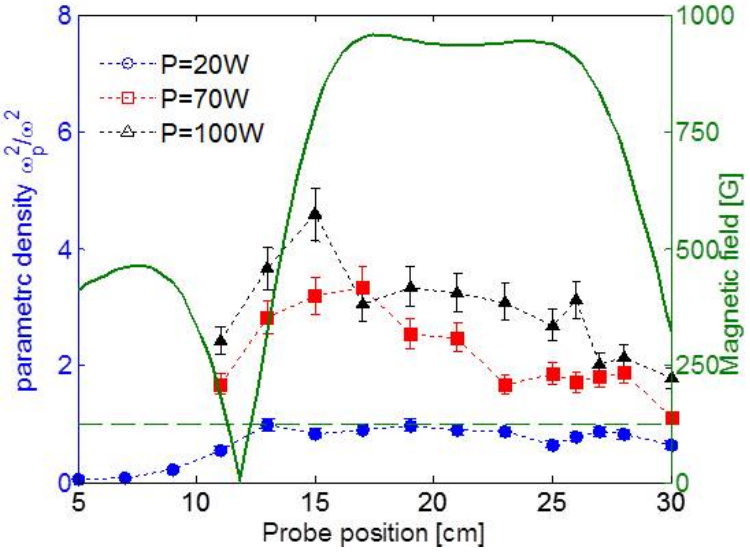

Figure 5.1.14: Normalized electron density (ω_p^2/ω^2) and magnetic field profile at $1.5 \cdot 10^{-4}$ mbar, 3.75 GHz frequency. Electron density is normalized with respect to the cutoff value.

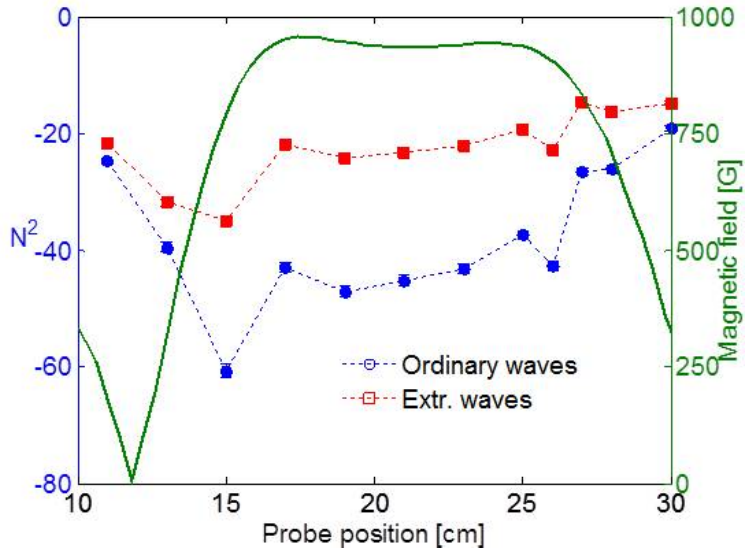

Figure 5.1.15: Squared refraction index for ordinary and extraordinary waves.

mic scale can show two or three different slopes, due unthermalized electron populations. At lower power level (20 W), EEDF shows a Maxwellian behaviour. However, for microwave power larger than 70 W, in regions where cyclotron harmonics are placed, the EEDF is made by the superposition of two different Maxwellian distributions. The most significative case, shown in figure 5.1.16, was obtained at the power level of 100 W, at the probe position of 13 cm (near the first ECR harmonic). The energy distribution is evidently formed by two peaks separated by several eV. The peak at higher energy is still maxwellian and seems to be inherent to an electron population whose center of mass is in relative motion with respect to the LP reference [85]. A fit of the double maxwellian population can be done by means of the following formula

$$F(v) = A_1(t_{e1}, v_{e1})e^{-\frac{mv^2}{kt_{e1}}} + A_2(t_{e2}, v_{e2})e^{-\frac{m(v-v_0^2)}{kt_{e1}}} \tag{5.1.3}$$

Only by adding the term v_0 in previous equation, (i.e. the center of mass velocity of the rotating plasma w.r.t the probe), it is possible to fit the experimental data. The best agreement between the experimental data and the theoretical (solid line in the figure) has been obtained by considering a relative velocity $v_0 = 1 \cdot 10^5 m/s$. Since the probe is placed parallel to the B lines, the drifting electrons can be argued to move across B, according to figure 5.1.17 *a*). Considering the B axial symmetry, we can suppose that the electrons are moving along azimuthal paths which enclose the chamber axis as it is shown in figure *b*).

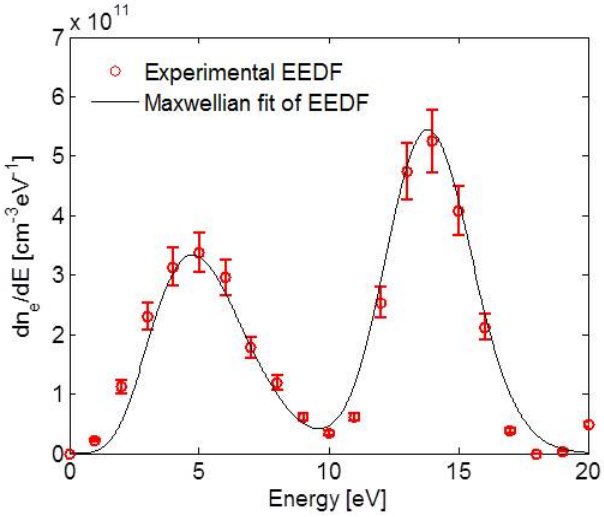

Figure 5.1.16: Electron Energy Distribution Function calculated at the probe position of 13 cm, in proximity of the first ECR harmonic at 3.65 GHz. Two different electron populations are present.

w

5.2 Plasma heating at 2.45 GHz in plasma reactor

In another phase of the experiment, we changed the operative frequency in the plasma reactor, in order to verify how the different working frequencies could affect to plasma parameter. A plasma was created inside the PR by means of a standard 2.45 GHz magnetron. Measurements have been performed by using an nitrogen gas at a pressure of $1.5 \cdot 10^{-4}$ mbar. At 2.45 GHz, as it is shown in figure 5.2.1, there exist either ECR resonance and its harmonics. This means that also in this configuration ES eaves can be excited. This configuration enables either the Electron cyclotron resonance and eventual ES heating. According to figure 5.2.1, B_{ECR} is placed at probe positions of 15.5 cm and 26.5 cm, while the first cyclotron harmonic are placed at 13.5 and 29.5 cm.

In figure 5.2.2 the results of the electron density measurements are shown. The measures have been carried out at different microwaves powers, from 20 W to 200 W. The measured electron density is larger than the cutoff one for every probe position. This is not surprising because, as ex-

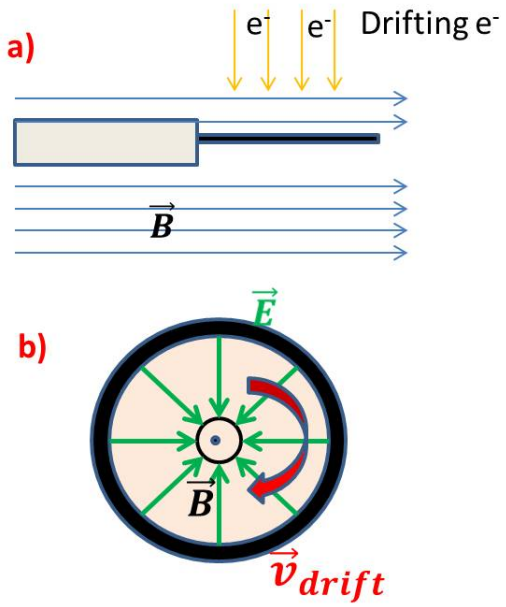

Figure 5.1.17: Electron Energy Distribution Function calculated at the probe position of 13 cm, in proximity of the first ECR harmonic at 3.65 GHz. Two different electron populations are present.

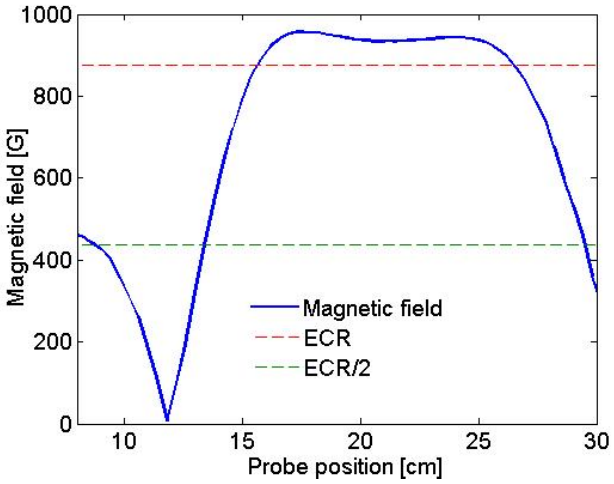

Figure 5.2.1: Magnetic configuration in the plasma chamber of plasma reactor. Both B_{ECR} and $B_{ECR}/2$ coexist in the chamber.

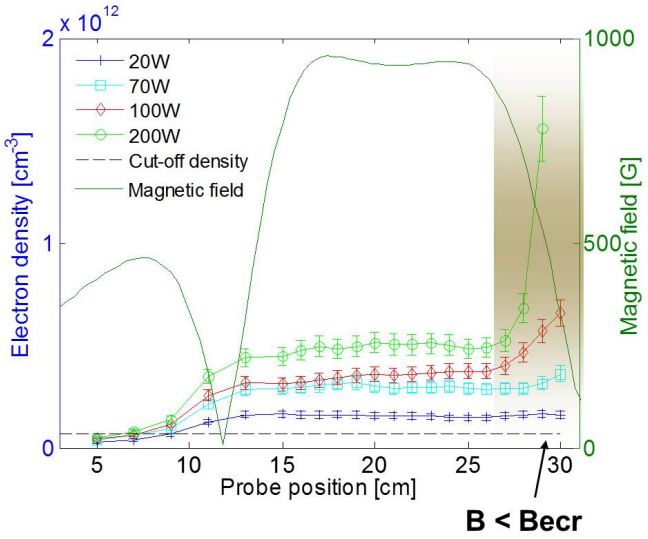

Figure 5.2.2: Electron density and magnetic field profile at $1.5 \cdot 10^{-4} mbars$, 2.45 GHz frequency at different microwave powers. Microwave injection occurs at the right-hand side of the figure.

plained in chapter 3, non-resonant absorption characterizing MDIS allows to reach density 2-3 times larger the cut-off density. Even for microwave power of 20 W, we measure a density slightly overdense. Electron density increases strongly when probe is positioned beyond 26 cm. This position corresponds to B_{ECR} and, from this position, density increase well beyond the cutoff density. How it is shown in figure 5.2.3, for all the different values of microwave power, beyond the probe position of $\sim 26cm$, ω_p^2/ω^2 becomes larger and larger. In particular at the power of 200 W, at position of 29 cm, electron density reaches the value of $\sim 1.5 \cdot 10^{12} cm^{-3}$ i.e. 20 times the cutoff density ($7.5 \cdot 10^{16} m^{-3}$ at 2.45 GHz). In such position the tungsten tip was heated up to the melting temperature so that it was impossible to make the measurement at 30 cm, similarly to that happened at the LP position corresponding to the first harmonic in the magnetic beach configuration (see in section).

The results about electron temperature are shown in figure 5.2.4. Electron temperature ranges between ~ 5 to ~ 15 eV. Larger temperatures were found in proximity of the two ECR resonances and, depending weakly on the input microwave power. At RF power of 20 W, for example, temperature

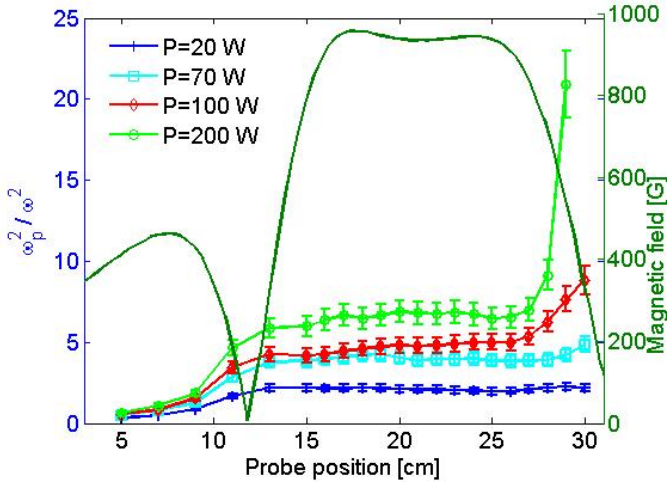

Figure 5.2.3: Electron density and magnetic field profile at $1.5 \cdot 10^{-4} mbars$, 2.45 GHz frequency. Electron density is normalized with respect to the cutoff value.

values are larger than at 100 W. However, the plasma energy content given by $(n_e T_e)$, increases when power level is increased. It is then evident that the increase in power level affects much more the electron density than the temperature.

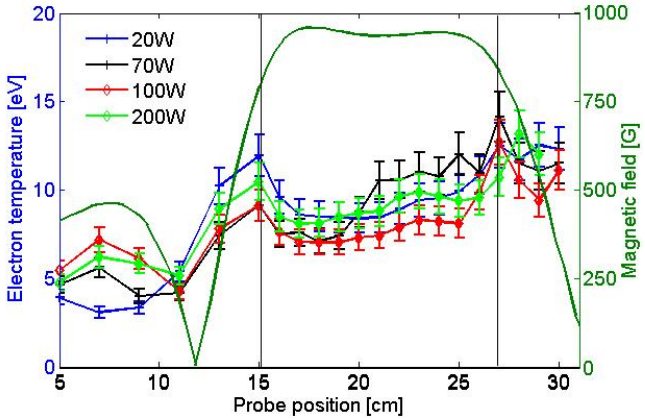

Figure 5.2.4: Electron temperature and magnetic field profile at $1.5 \cdot 10^{-4} mbars$, 2.45 GHz frequency higher temperature are obtained at ECR resonances.

5.2.1 Ray Tracing modelling

In previous sections it has been demonstrated that in many experimental configurations our plasma exceeds density cutoff. Measurements of E.M power within the plasma chamber have further confirmed that in configurations like the flat B field one, only a very low E.M power is measured within the plasma cavity at higher densities. This result is consistent with the theory, since no E.M energy can propagate in an overdense plasma core. The calculation of the refraction index, shown in figure 5.1.15, had confirmed that no E.M field can propagate in the plasma region covered by LP. The presence of a largely overdense plasma without E.M field is contradictory: somewhere inside the chamber an underdense region must be situated, thus allowing the mode conversion, so that it reinforced the hypothesis that the energy is carried into the plasma core by waves of different nature (e.g. EBW) that however must be generated in an under-dense region (UHR is required). In order to clarify were E.M waves can be converted into EBW, a simplified 2D ray tracing calculation has been implemented to follow EM-waves path in the non-isotropic and non-homogeneous plasma. The basic idea is to follow, step by step, a single microwave ray, characterized by a varying amplitude in space and time. The ray enters the chamber from the waveguide in presence of an anisotropic plasma. The general behaviour of E.M field in a point will be given by the sum of the squared amplitudes which have crossed that point. In such a way, each wave front point is let

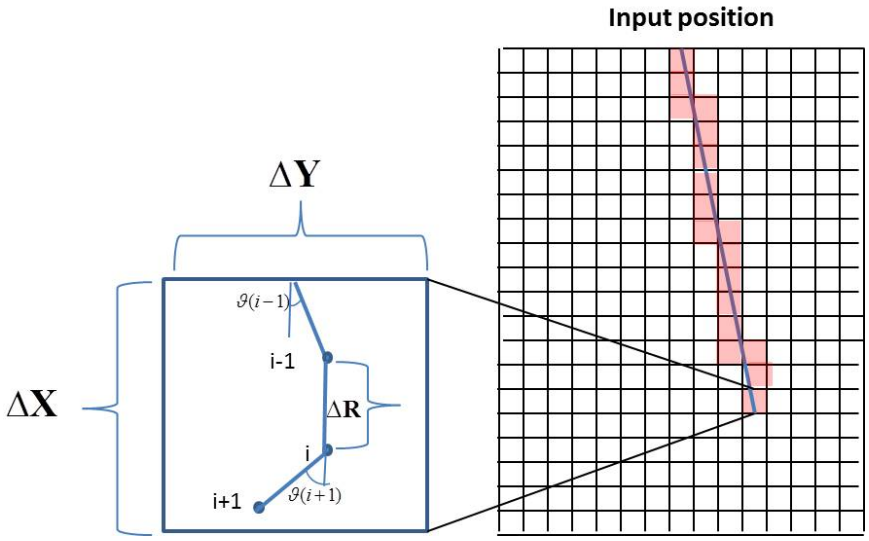

Figure 5.2.5: the ray propagates step by step following equations (5.2.1) through the chamber reference system.

to advance in the non-homogeneous medium, like a particle which is moving subjected to certain conditions (the local refractive index)
We define two reference systems: the frame of a ray moving from the input position to the plasma chamber and the frame of the chamber itself. As first approximation, all rays can start from the same input position without loss of generality. The wave propagation angle can be chosen randomly from $-\pi/2$ to $\pi/2$. In the frame of the free ray, position depends on the position and the propagation angle at iteration i-1:

$$\begin{cases} R_x(i) = R_x(i-1) + \Delta R \cos\left(\theta(i-1)\right) \\ R_y(i) = R_y(i-1) + \Delta R \cos\left(\theta(i-1)\right) \end{cases} \tag{5.2.1}$$

Where ΔR is the propagation step.
The frame of the resonator is divided in square cells, larger than ΔR. Both reference systems are shown in figure 5.2.5. By knowing the ray position, is possible to find its position in the chamber frame.

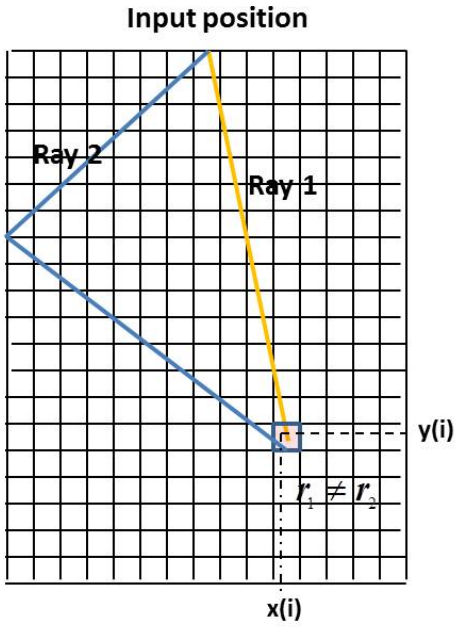

Figure 5.2.6: The total amplitude of the field in a cell is given by the sum of the amplitudes of wave crossing that cell. Because the rays cover different paths, in general their amplitude in a cell is different. If interference is constructive, amplitude sum each other, if destructive they must be subtracted.

Wave amplitude associated to the ray is given by a complex number and depends on the total path of each ray, as:

$$A(r) = Ce^{i\omega t} = Ce^{-2\pi i\nu \frac{r}{c}} \tag{5.2.2}$$

where C is an arbitrary constant, ν is the wave frequency and r the total path covered by the ray. If two rays reach the same cell after covering different distances, it follows that the total amplitude is given by the sum of the amplitudes of the two rays crossing the same cell, as shown in figure 5.2.6. In particular if a ray labeled as k_1 reaches a cell of coordinate (x(i), y(i)), we have:

$$E_{k_1}(x(i), y(i)) = Ce^{-2\pi i\nu \frac{r_{k_1}}{c}} \tag{5.2.3}$$

We then calculate the squared amplitude, which represents the real physical quantity:

$$|E_{k_1}(x(i), y(i))|^2 = |Ce^{-2\pi i\nu \frac{r_{k_1}}{c}}|^2 \tag{5.2.4}$$

If a second ray k_2 reaches the same cell after a path r_{k_2}, its amplitude sums to the previous one:

$$E_{k_2}\left(x(i), y(i)\right) = |E_{k_1}\left(x(i), y(i)\right) + Ce^{-2\pi i\nu\frac{r_{k_2}}{c}}|^2 \tag{5.2.5}$$

So after n rays we have that the squared electric field module is:

$$|E\left(x(i), y(i)\right)|^2 = |\sum_k Ce^{-2\pi i\nu\frac{r_{rays}}{c}}|^2 \tag{5.2.6}$$

Because the amplitude depends on the covered path, the different rays provide construstive/destructive interference in each cell of the simulated domain. Provided that a sufficient large number of rays are simulated, the averall E.M energy distribution into the chamber can be obtained. The angle at iteration i depends on the angle at iteration i-1 by means of the Snell laws:

$$\sin\theta(i)N(i) = \sin\theta(i-1)N(i-1) \tag{5.2.7}$$

where N is the refraction index of the the plasma in the cell of coordinate X(i), Y(i). In empty resonators N=1 everywhere, so $\theta(i) = \theta(i-1)$. In magnetized plasmas it is given by the Appleton formula (2.1.24). As it was demonstrated in chapter 2, the refraction index depends on the normalized electron density X and on the normalized magnetic field Y and it is different for ordinary and extraordinary waves. X and Y depend on the electron density of the plasma at position i and on magnetic field on position i, therefore preformed electron density and magnetic field maps are needed. According with experimental measurements, a simplified model of plasma density distribution and magnetic field can be argued. We introduce in the model the density and magnetic maps shown in figure 5.2.7. Density is overdense in the central region of the chamber and goes to zero near the wall (this assumption is physically required by boundary conditions). The magnetic field map is similar to the plasma reactor one.

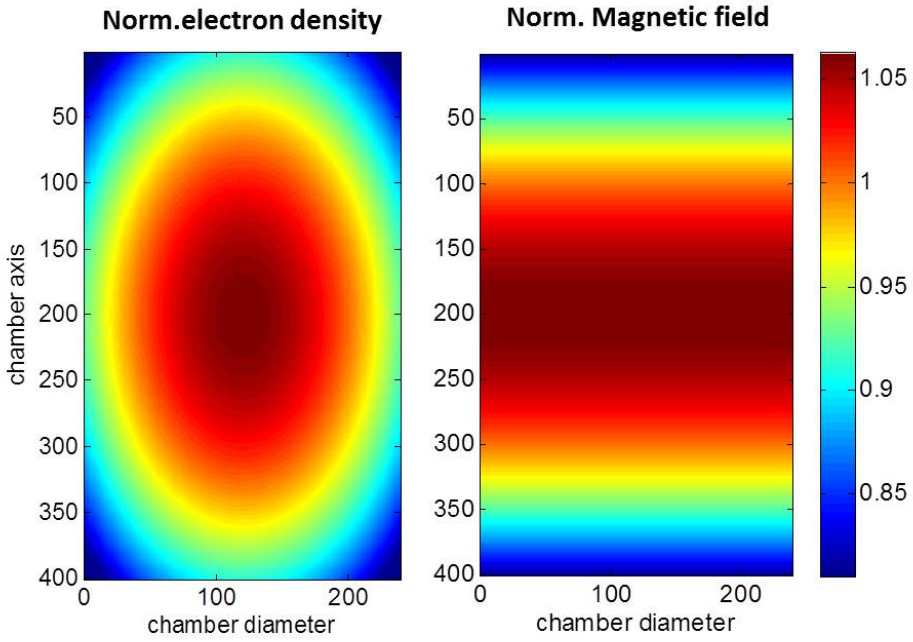

Figure 5.2.7: Example of the density and magnetic maps used in simulations.

Since for ask of simplicity we are considering the "D case, the E.M waves propagating in a bi-dimensional cavity with perfectly conducting walls. The validity of the numerical approach has been formally tested with an empty cavity, with the aim to reproduce the well known pattern characterizing resonant modes in closed metallic cavity. In a rectangular shaped 2D cavity the propagation modes are a simplified case of the modes in a 3D rectangular cavities: [3]

$$\begin{aligned} E_x &= \cos(q\pi\frac{x}{b})\cos(p\pi\frac{y}{a}) \\ E_y &= \cos(q\pi\frac{x}{b})\cos(p\pi\frac{y}{a}) \end{aligned} \tag{5.2.8}$$

while the resonance frequencies can be found by means of the following

relation:

$$\nu = \frac{c}{2}\sqrt{\frac{p^2}{a^2} + \frac{q^2}{b^2}} \tag{5.2.9}$$

where a and b are the chamber dimensions, and $p, q = 1, 2, ..., N$.
Ray tracing has been tested for several combinations of p, q in a . Some of the results (p=2, q=0 ν=1.1992 GHz, p=4, q=2 1 ν=3.1219 GHz) have been summarized in figure 5.2.8. 2D ray tracing reasonably reproduces the modal behaviour of E.M field in 2D resonators. Moreover it show that E.M field increase near the microwave injection, which is out of the possibilities of equations (5.2.8). In particular, this approach demonstrates that resonant modes having p index cannot exist in real resonators. In facts, an odd p index implies that the modal configuration has a minimum at the input. Because this condition can not be satisfied in real resonators, these modes can not exist.

Now we introduce the magnetized plasma described by figure 5.2.7 in the resonator. In figure 5.2.9 the first steps of ray propagation in presence of a magnetized plasma have been shown. It is evident that the high density plasma distorts significantly the rays paths. The high density plasma core is arduously reachable by the wave.

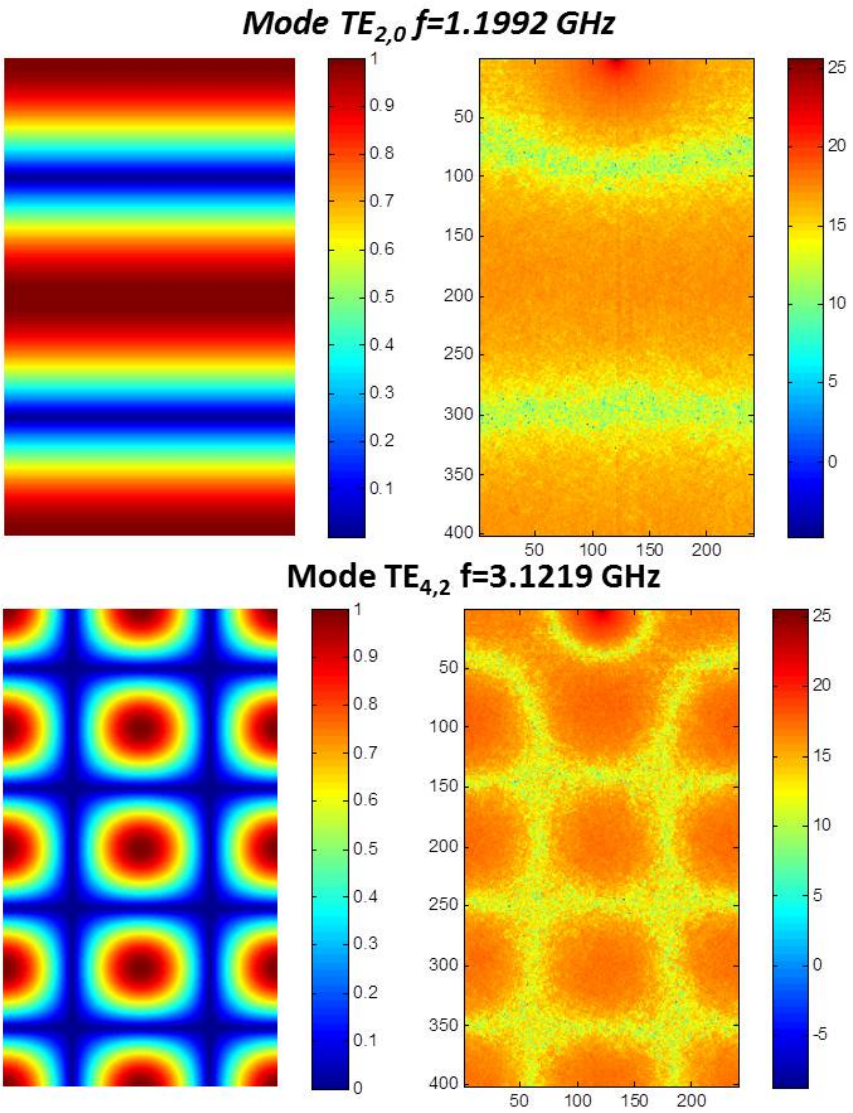

Figure 5.2.8: Comparison between numerical simulation and analytical solution for the $TE_{2,0}$ (f=1.1992 GHz) and $TE_{4,2}$: (f=3.1219 GHz) modes. Ray tracing reproduces the modal behaviour and moreover predicts the E.M power maximum in proximity of the waveguide input.

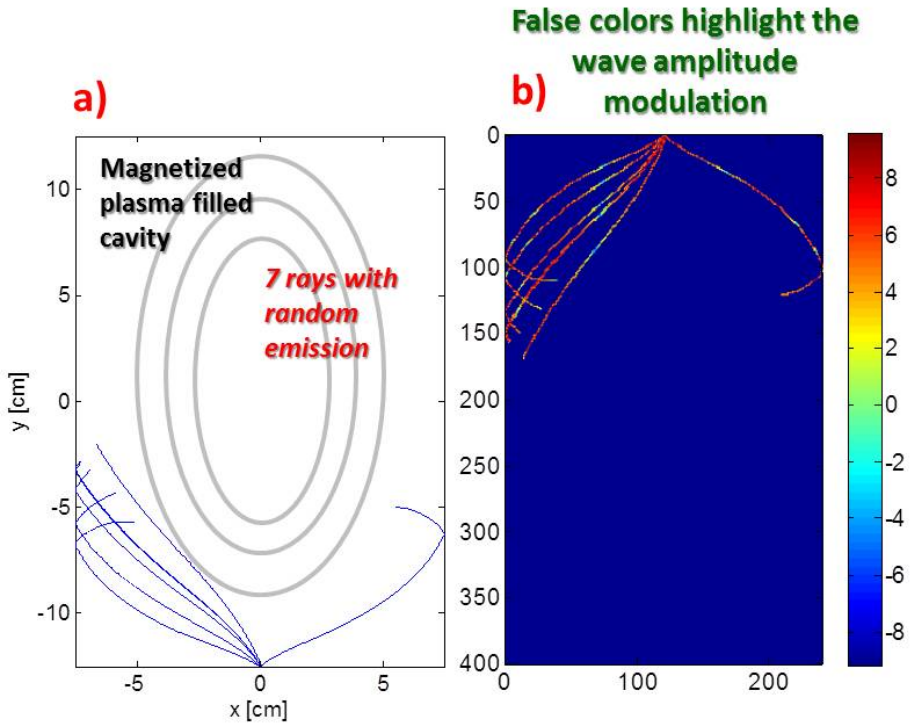

Figure 5.2.9: Microwave rays departing from an input (point-like) source, and propagating into a non-uniform magnetized plasma: *A*) it is evident that the high density plasma is arduously reachable and it distorts significantly the rays paths. *B*) The false colors puts in evidence the modulation of the wave amplitude; where amplitudes will sum constructively we shall find a maximum.

As it is known, in plasma filled cavities the microwaves are absorbed at the resonances and reflected at cut-off surfaces, depending on the value of electron density and magnetic field. We can check if in a certain cell i having coordinates x(i),y(i) a resonance can occur by verifying if the normalized density X(x(i),y(i)) and magnetic field Y(x(i),y(i)) in that cell satisfy the resonance condition:

$$\cos\left(\frac{X+Y^2-1}{XY^2}\right)^{\frac{1}{2}}=0 \tag{5.2.10}$$

on the contrary the wave is reflected when:

$$N(x, y) \leq 0 \tag{5.2.11}$$

Unfortunately it's not simple to solve the problem for reflection. It's necessary to evaluate the plasma reflection surfaces. Since the structure of the reflecting surfaces could be a very complex, in principle, we stopped our calculations of a single ray path when it encountered a cut-off or a resonance. The numerical method allows to find regions in which the resonances and cutoffs can occur. In figure 5.2.10 the results for extraordinary wave's ray tracing are shown. Red dots corresponds to regions where the wave propagation is prohibited (beyond the cutoff), while green bullets indicate the points where UHR could be situated. While the plasma core seems totally unaccessible to E.M radiation, The UHR can occur near the wall of the plasma chamber, along a ring surrounding the chamber axis. There the EM-ES mode conversion can take place and finally ES waves can propagate until they are absorbed at the cyclotron harmonics. The results fit totally with the experimental observation.

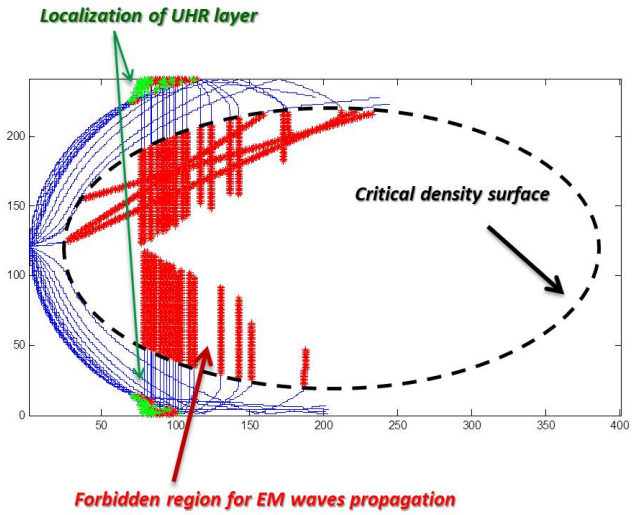

Figure 5.2.10: The Extraordinary waves cannot penetrate the overdense plasma, however in peripheral regions UHR can occur. ES waves eventually generated, can propagate orthogonally to the Magnetic field and sustain the overdense plasma core.

The E.M field does not penetrate the overdense plasma core, but can flow all around it, being absorbed at the UHR resonances, if present. E.S waves, and in particular EBW, can be produced by means of modal conversion, and then sustain the overdense plasma core. In figure 5.2.11 the UHR layers in a 3D view at 2.45 GHz and 3.75 GHz after 100.000 rays are displayed along with the plasma images in the optical domain. These figures have been obtained by a π rotation of the 2D figure. At 2.45 GHz, Upper Hybrid resonance can occur exclusively in two different ring placed near injection and extraction flanges. The images in the visible confirm in facts the presence of two little rings when plasma is fed with 2.45 GHz microwaves. At 3.75 GHz, UHR is possible along an anular region enclosing the entire core. Also in this case the plasma images put in evidence the presence of a resonance surface near the chamber walls. These images have been taken at low E.M power condition, when UHR is visible because the only collisional heating at resonances acts and the core is not so bright. As it will be shown in next section, beyond a power threshold, plasma shape will change, and only the brighter highly overdense region will be visible.

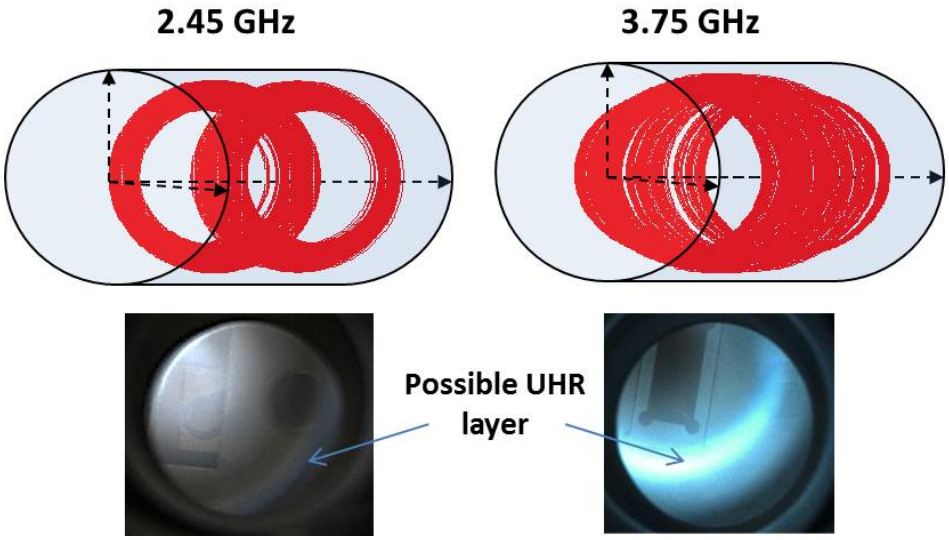

Figure 5.2.11: UHR layers at 2.45 GHz and 3.75 GHz after 100.000 rays. At 2.45 GHz upper hybrid resonance can occur exclusively in two different ring placed near injection and extraction flanges. The images confirm the presence of two little ring when plasma is feeded with 2.45 GHz microwaves. At 3.75 GHz, UHR is possible all around the overdense plasma region as confirmed by the related image.

5.3 Spectral emission analysis

In section 2.6.3 we found that the generation of EBW should be also accompanied by an ancillary phenomenon, namely the formation of plasma waves in the MHz range (ion waves). In order to detect such ancillary phenomena, we used the tip of the Langmuir probe as a local electromagnetic antenna, which was connected to a Spectrum Analyzer for the plasma spectral emission analysis. In figure 5.3.1 the electromagnetic spectrum in the range of GHz, for different RF powers, is shown. At the power of 50 W, as expected, we reveal only the presence of waves with frequency of 3.7476 GHz, i.e. only the microwaves injected by means of TWT propagate in the source. When the power in increased, however, sidebands of the pumping wave appear. The threshold RF power is found to be 70 W. Together with sidebands also a considerable enlargement of the signal spectrum can be noted. Increasing the microwave power up to 100 W this effect increases further: sidebands

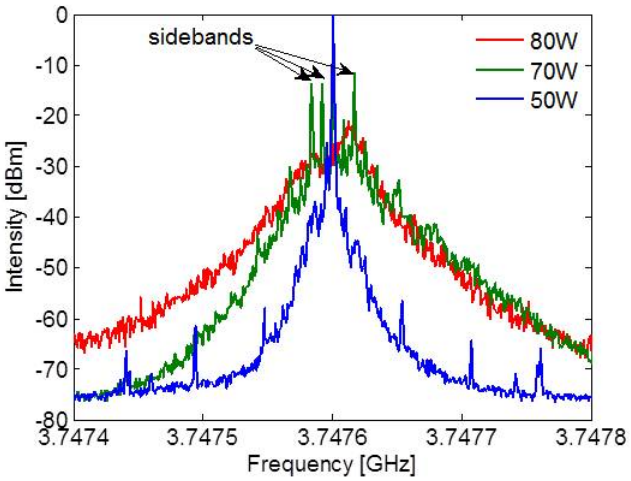

Figure 5.3.1: Electromagnetic spectrum in the range of GHz for different microwaves powers. At larger power sidebands and broadening of the pumping wave appear.

vanish, but the spectrum further enlarges leading the complete broadening of the the signal.

Together with the measurements in the range of GHz, a series of measurements of spectral emission in the range of MHz was performed, in order to detect the presence ion waves. How it is shown in figure 5.3.2, **ion waves are revealed only above the threshold of 80 W, simultaneously with the appearance of sidebands in range of GHz**. And this is a clear evidence that the modal conversion occurs once crossed a critical power threshold. To confirm this we acquired the ion spectrum above threshold, in particular at 90 W, but at 2 different operating pressures (figure 5.3.3). The attempt at high pressure was carried out to exclude that the ion signal was the result of an electromagnetic noise of the microwave generator. On the contrary, the ion waves were revealed only at the pressure for which we measured simultaneously the overdense plasma, the broadening of the spectrum at high frequency, as well as the emission of X radiation (see next section). It is therefore evident that the threshold which we found in different experimental result is the instability threshold required to have modal conversion and then EBW propagation into the plasma (see also section 2.6.3 for reference). Furthermore the reproducibility of these phenomena is encouraging in view of the applications aiming to the generation of overdense plasmas

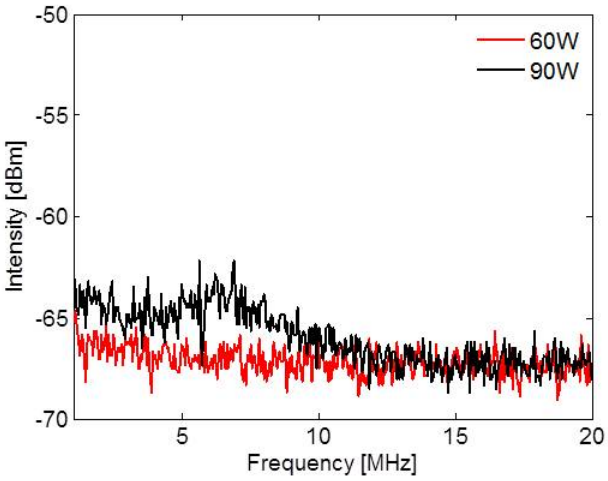

Figure 5.3.2: Electromagnetic spectrum in the range of MHz for different microwaves powers and same pressure. Intensity increases at 90 W, showing the presence of plasma generated ion waves

for high intensity ion sources.

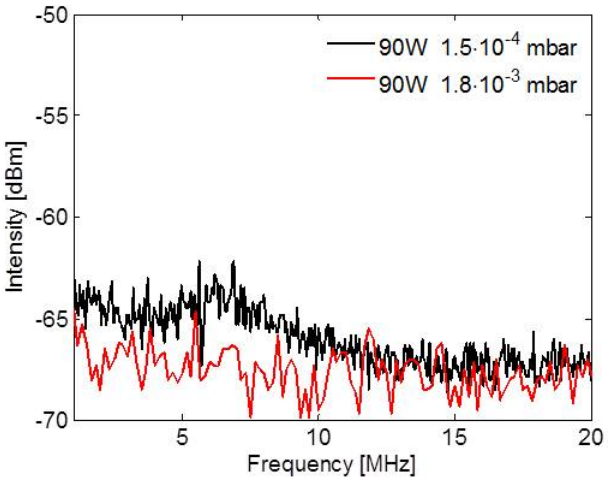

Figure 5.3.3: Electromagnetic spectrum in the range of MHz for different pressures and microwave power of 90 W. At higher pressure ion waves vanish, therefore their existence can not depend on the microwave generator, but only by intrinsic phenomena occurring into the plasma.

5.4 X ray spectroscopy

When the EBW generation has been introduced (section 2.6.1), we found that the X-ray emission from the plasma represents one of the fingerprint and about the generation of EBW. Their presence is in facts consistent with the mechanism of "plasma heating" through the generation and absorption of electrostatic waves. X-ray emission is indicative of the fact that the absorption of the EBW generated a hot electron population, separated from the plasma bulk and for this takes the name of "suprathermal". The generation of such a tail is predicted by the Segdeev and Shapiro damping theory, as the energy absorption rate is proportional to the energy itself: $\frac{dW}{dT} \propto W$. X ray emission represents a valuable tool for plasma diagnostics. Electrons having energies of several keV can not be detected by the L.P. diagnostic, several several kV on the probe would be necessary.
Measurements have been carried out in flat-B field magnetic configuration either at 2.45 GHz (magnetron) and 3.75 GHz, by using HPGe detector (according to section 4.3.4). The data have been analyzed according to the equation (4.3.15). In figure 5.4.1 we plotted respectively the spectral tem-

perature calculated from the original X ray spectra for a nitrogen plasma at $1.5 \cdot 10^{-4}$ mbar. At 3.75 GHz, electron temperature is lower than 1 keV up to 40 W, and it increases up to 1.5 keV at 70 W. Beyond this threshold value however, consistently with previous evidences, the electron temperature suddenly increased up to $\sim$ 3.7 keV. At 2.45 GHz a similar behaviour can be observed, even more evident: no spectral emission was detected up to 70 W; then the X ray emission starts, having a temperature of about 1.3 keV. Such behavior is clearly typical of the triggering of nonlinear. Once exceeded the critical threshold, the temperature remains approximately constant for higher power values. The end point energy represents the second important information which can be obtained by spectrum analysis, according to section 4.3.3. As shown in figure 5.4.2 its value is about ten times the value of the spectral temperature. The end point energy represents the maximum energy achievable by the electrons in that particular configuration. From end-point energy, according to equation (2.7.6), it is possible to estimate the value of EBW electric field:

$$E = B\sqrt{\frac{2E_{end-point}}{m_e}} \tag{5.4.1}$$

This formula gives electron fields reaching $1.2 \cdot 10^7$ V/m at higher electron energies.

The measurements performed with the SDD detector revealed a strong capability of the plasma to emit large amounts of X-rays in the energy range extending from a few hundred eV to a few keV. Such a feature has potential practical applications, especially in the field of material analysis [90]. In particular, these plasmas may represent the test-bench for the design of innovative high emissivity X-ray sources. For this reason, systematic studies have been started in order to identify the plasma conditions which maximize the X-rays emission rate. In particular, various gases (argon, nitrogen, hydrogen), fluxed inside the reactor at different pressures, have been studied. Figure 5.4.3 shows the emission spectra of a hydrogen plasma at a pressure of $7.7 \cdot 10^{-4}$ and at the power of 75 and 130 W. Counts are not defined in the lower energy domain of the incident radiation [0.1-2 keV], because in this region the detector efficiency is very low and suffers considerable fluctuations: the efficiency in facts spans from 0.05% for energies of 1keV to 0.6% at 2 keV (as shown by the efficiency curve shown in figure 4.3.11). The counts in the domain energy from 2-14 keV were acquired with detector efficiency greater than 0.8 up to a maximum of 0.98.

The fits of figure 4.3.11 has been calculated by means of equation (4.3.15);

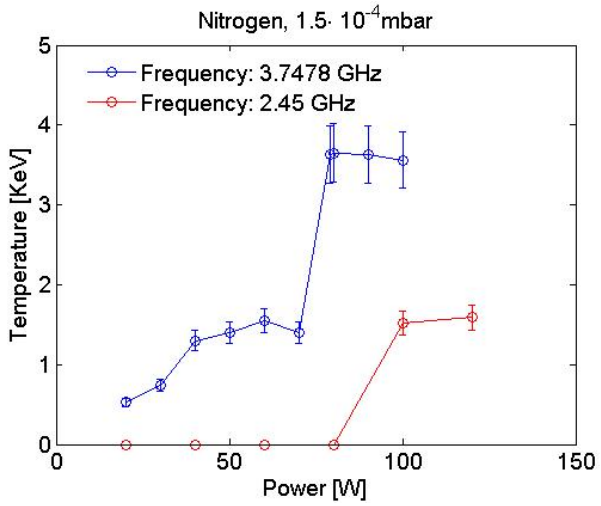

Figure 5.4.1: Spectral temperatures. At frequency of 2.45 GHz, ECR heating and EBW heating coexist; at 3.75 GHz, EBW heating is dominant.

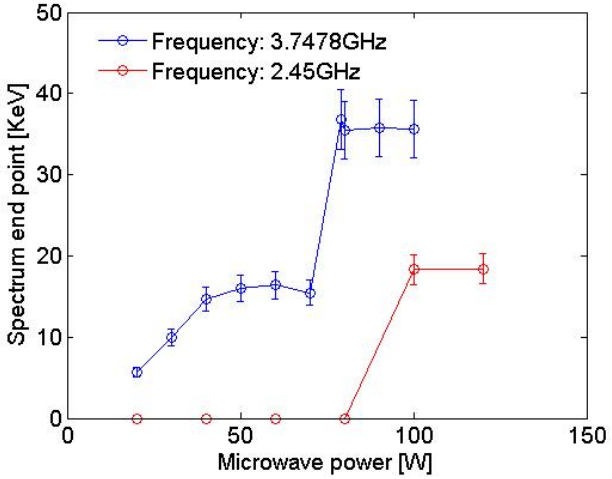

Figure 5.4.2: End-point energy at 2.45 GHz and 3.75 GHz this value represent the maximum energy electrons reach in plasma for that value of pressures and microwave power.

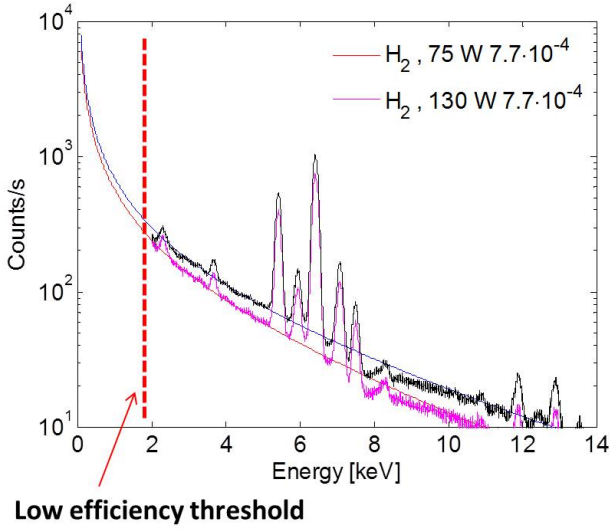

Figure 5.4.3: The X rays emission spectra and theoretical fit in the region of low efficiency.

they enable to extrapolate the X ray emission in regions where detector efficiency is too low. This information in particular, allow to evaluate the total emissivity of suprathermals employing also the emission occurring at lower energy. By performing the integration of experimental curves, the measured counts per second (2-14 keV) correspond to $7 \cdot 10^5$, $3 \cdot 10^5$ in the energy interval 2-5 keV. In order to estimate the total counts for the entire suprathermal plasma component, we add the contribution of the region of low detection efficiency. This was done by extrapolating the counts in the range 0.1-2 keV on the basis of the theoretical fit; the result was $3 \cdot 10^6$ counts per second, a value about four time larger than than previous one, which means that the largest part of X ray emission takes place in the low energy range [0.1-2 keV]. We show a further result, highlighting that X ray emission depends on the operating plasma conditions and in particular on the gas type, the microwave frequency and the working pressure. In figure 5.4.4 the X rays emission rate as a function of the microwave power at different operational parameters; like gas, frequency and pressure is reported. it can be observed that emission is sensitive to the changes in operating parameters; however for all the different plasmas, the most significant increase in the radiation emission occurs around 70-80 W. The gas (among the tested ones) for which

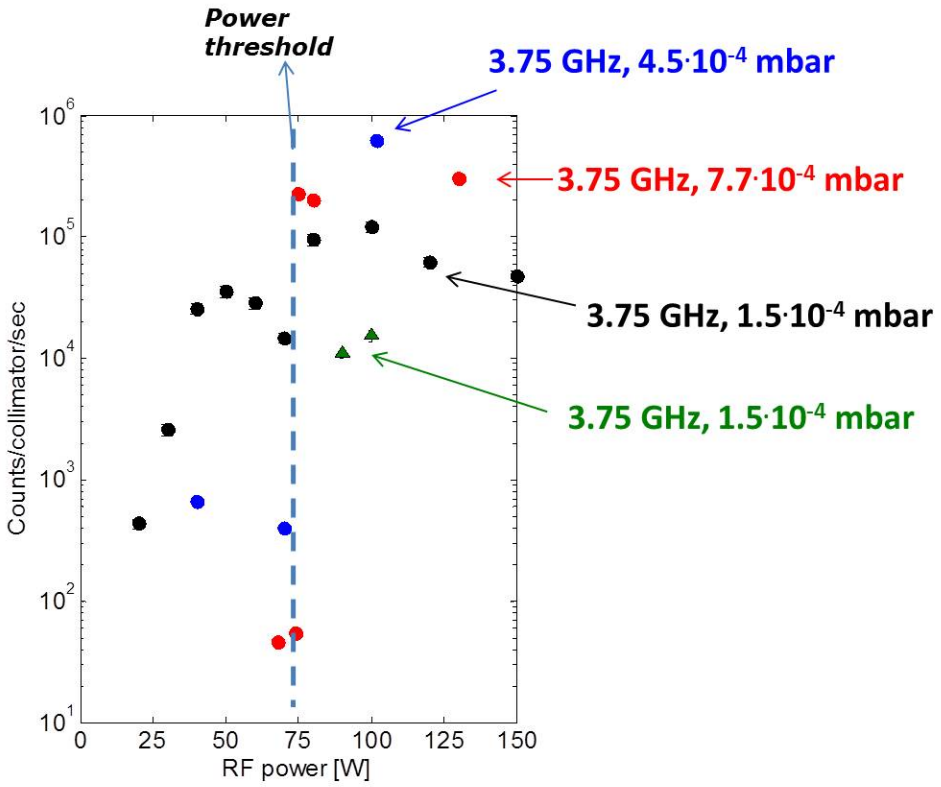

Figure 5.4.4: X rays emission Rate in function of the power at different the operating plasma parameters: gas, pressure, frequency.

the maximum emission is obtained is the Hydrogen. The optimum pressure is placed around the $4 - 5 \cdot 10^{-4}$ mbar, while there is a strong dependence of the emission from the operating frequency. The attempt made at a lower frequency (2.45 GHz) compared to that obtained at 3.76 GHz show a net decrease in the emission rate.

5.5 Plasma imaging in optical and X rays domain

To verify the different hypothesis introduced in last sections, we have acquired images by means of the pin-hole camera introduced in section 4.3.4. The X ray images will be then compared with the images in optical domain obtained by means of a second CCD camera placed in the same position of the X ray pin-hole camera. The experimental set-up is shown in figure 4.3.12. We first discuss first the imagines in the optical domain, which will allow to better recognize in the following the correlations with the images in the X-rays domain. The captured images shown in figure 5.5.1 put in evidence that the plasma structure depends on the frequency and on the power level. The images was captured either at 2.45 GHz and 3.75 GHz at increasing power levels. At the frequency of 2.45 GHz the plasma shows a bright "core" surrounded by a darker halo. This type of structure is quite common in plasmas wherein absorption of electromagnetic energy occurs mainly at ECR resonance. At low power, in both configurations a ring is visible. Different experimental evidences shown in the last sections, and in particular the ray tracing simulations (section 5.2.1) have suggested that this layer may correspond to the UHR layer. The ring disappear in both configurations when microwave power is increased over 80 W. This threshold value compared again as in large part of in the previous sections measurements. At 3.75 GHz, as soon as the lateral ring disappears at power larger than 80 W, the plasma assumes the circular structure containing an hole in the center. This structure are usually named as "**plasma hole**".

The pin-hole camera has been used for the X imaging of an argon plasma generated at the microwave frequency of 3.7475 GHz, at different power values and at a pressure of $3 \cdot 10^{-4}$ mbar. The results are shown in figure 5.5.2. At 20 W no X rays radiation is revealed, and only at 40 W a slight X radiation emission appears. Only beyond 60 W a well defined "plasma hole-like" structure appears, practically identical to the plasma hole structure revealed in the visible domain.

Although the origin of the real structure of the plasma hole is still not perfectly clear, the experimental data put in evidence that plasma hole in the X rays domain is generated together with the other experimental evidences of EBW heating (E.M spectra broadening, X-rays generation, overdense regime transition). The structure of the plasma hole visible also in the X-rays dominium leads to the conclusion that it is related to the spatial configuration of the suprathermals electron population, in facts they are the only ones able to emit radiation in the in the keV range. The layer surrounding can be thereby named **Hot Electron Layer (HEL)**. This

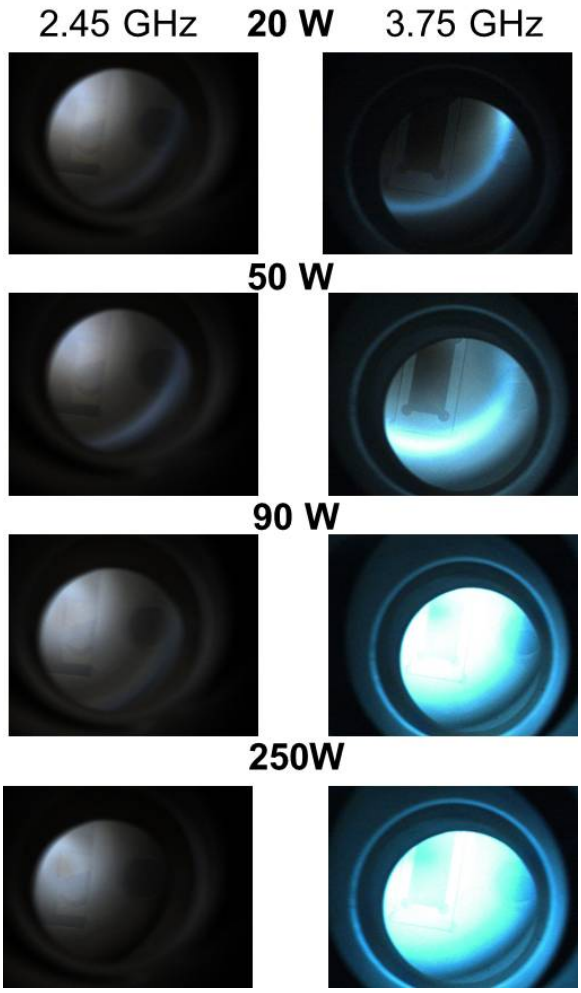

Figure 5.5.1: Images of the plasma at f = 2.45 GHz (on the left) and f= 3.75 GHz (on the right) at different microwaves power and Pressure=$1.5 \cdot 10^{-4}$ mbars.

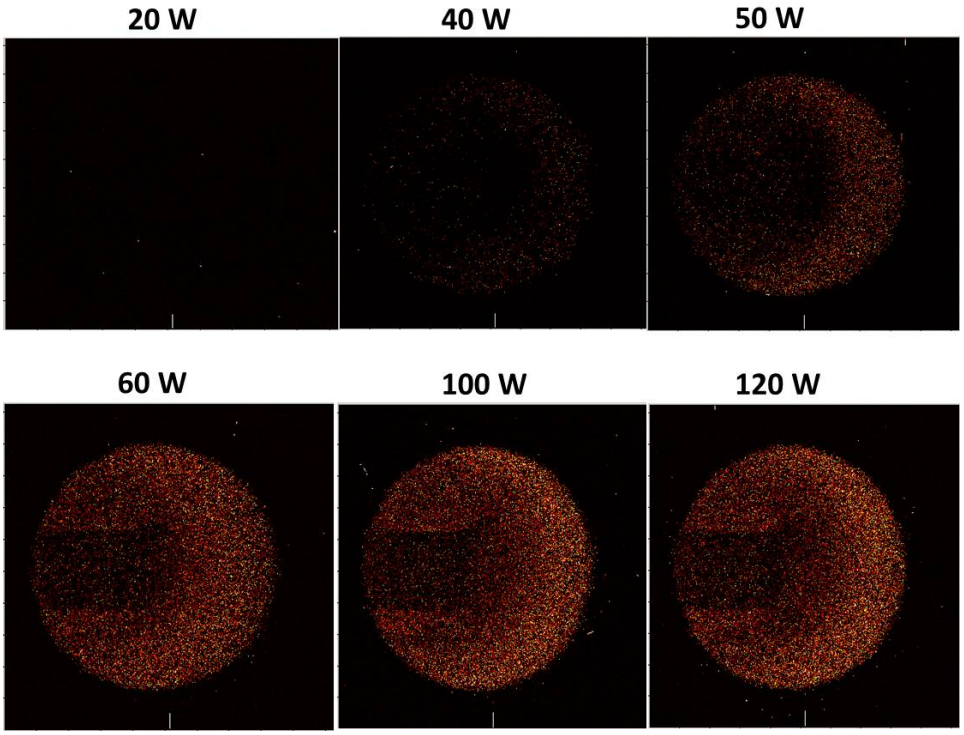

Figure 5.5.2: Pin-hole camera imagine of X rays at increasing power level. over the threshold power level, the X ray emission put in evidence the strong correlations with the images in optical domain.

result is in perfect agreement with the Golovanivsky's theory introduced in section 2.7.2. A detailed treatment of the x ray imaging can be found in reference [91]

5.6 Influence of the magnetic field configuration on hot electrons population

In order to understand the correlation existing between the magnetic field configuration and the presence of X rays, a series of measurements on the VIS source were carried out. As introduced in section 4.2, VIS enables us to remove any under-resonance region within the plasma chamber. When $B > B_{ECR}$ everywhere within the source, the upper hybrid resonance there

not exist (we here remind that UHR exists if $n_e < n_{UHR}$ and $B < B_{ECR}$). In previous sections we have further supposed that, when UHR is present, EBW are generated above a threshold power. One of the signature of EBW presence is represented by X ray emission, that was shown in previous sections to appear together with the other EBW signatures. The VIS magnetic field allows us to further test this model. We expect that if magnetic field is everywhere larger than B_{ECR}, no X emission occurs because EBW cannot exist. If part of the VIS plasma chamber, on the contrary, is under-resonance, then X ray emission could be detected. In order to allow the X-rays detection in the energetic range 1-30 keV, VIS source was used as a test-bench (disconnected from the extraction column) on work table and a HPGe detector has been connected to the source. In the first part of the experiment, we modified the magnetic field position w.r.t. the VIS plasma chamber as shown in figure 5.6.1). In such a way, microwave injection takes place at different values of magnetic field. we chose 4 configurations, shown in figure 5.6.1) which are different for the field in the injection region. A measurement of X-ray emission has been done by means of HPGe X detector in each magnetic configuration. In figure 5.6.2, the results are shown. We use as reference B_{ECR}. X rays were detected particularly in position D, where $B_{inj}/B_{ECR} = 0.92$. In this configuration, X-rays emission having spectral temperatures of the order of 1 keV. When the injection approaches B_{ECR}, X rays tend to disappear and finally, at position A ($B_{inj}/B_{ECR} > 1$), no X rays were detected. These results show that the production of high energy X rays ($T > 1keV$) takes place only in case of under-resonance discharge, that is the required condition to have UHR placed somewhere in the injection region of VIS plasma chamber. For $B_{inj}/B_{ECR} < 0.95$, the UHR takes place at quite high plasma densities, thus sustaining the production of a large number of warm electrons. These measurements can further be related with the emittance measurement carried out in a previous experiment [70]. The emittance measurements carried out in configurations A and D have shown a larger emittance in configuration D ($\epsilon = 0.207\ \pi$ mm mrad) than in configuration A (only $0.125\ \pi$ mm mrad). The emittance ϵ, as introduced in section 3.5.1 depends linearly on the magnetic field at extraction B_{ext} and on the root square of ion temperature (see equation 3.5.4).

Since B_{ext} does not change significantly between configuration A and D, and r and M/Q are constant, it follows the the ion temperature increases in configuration D. This effect is clearly due to the Landau damping of the ion waves generated at UHR as effect of the modal conversion (see section 2.6.2). The ancillary presence of ion waves, therefore confirms the

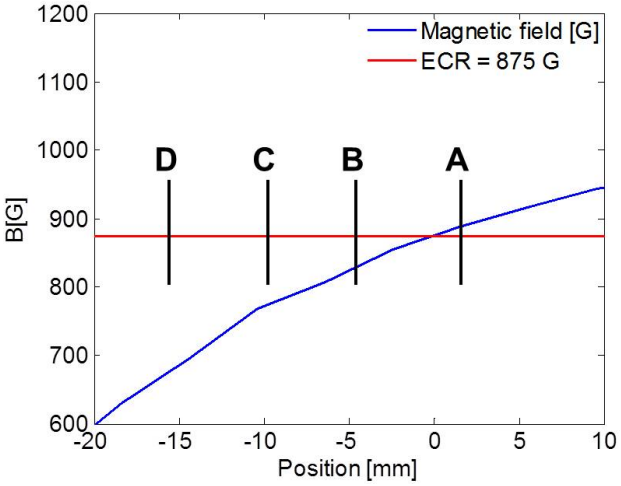

Figure 5.6.1: Position of Microwave injection with respect to the magnetic field. In configuration A, the injection occurs off-resonance; in configuration B, C, and D, the injection occurs under-resonance.

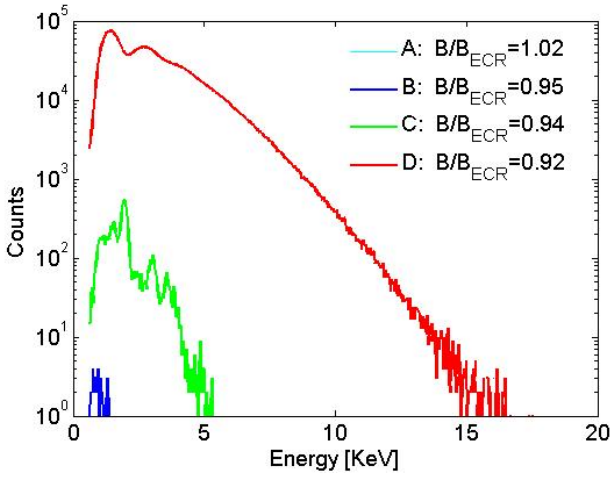

Figure 5.6.2: X ray detected at different positions of magnetic field. At position A, no X rays have been detected.

EBW generation when the $B_{inj} < B_{ECR}$. In conclusion, these measurement allow to relate univocally the presence of high energy X-rays in MDIS to

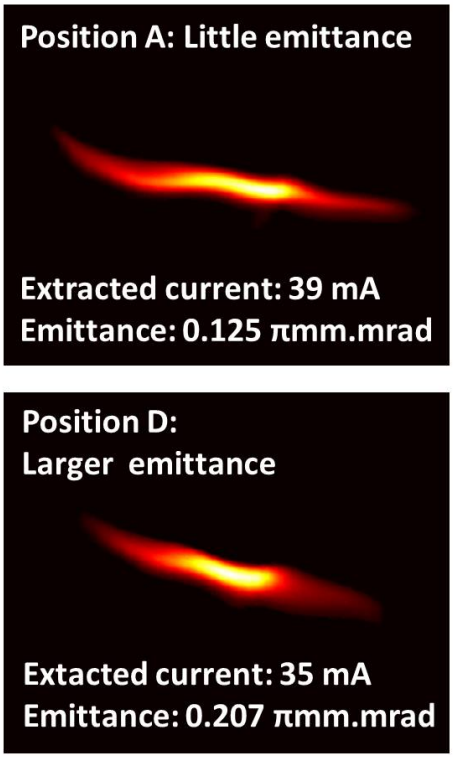

Figure 5.6.3: The emittance is smaller when injection occurs off-resonance (position A). When injections take place under-resonance, emittance increases (position D).

phenomena occurring exclusively in under-resonance condition, when the modal conversion can occur.

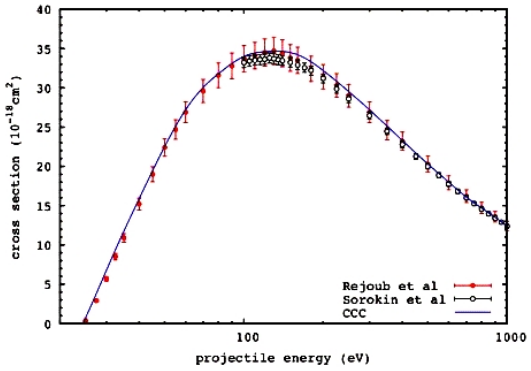

Figure 5.7.1: Cross section [89] of the reaction: $He^+ + 2e^-$.

5.7 Influence of under-resonance plasma heating on the electron energy content

Up to now MDIS are usually used to generate high intensity mono-charged current of light ions. The low confinement time and the low energy content $n_e t_e$ does not typically enable to generate multi-charged ions. The use of EBW heating in plasma reactor, as we have described in the previous sections, allows to generate a plasmas with larger energy contents. However, we are not able to make a measurement of extracted current by using the plasma reactor, because it has not an extraction system. In section 5.6 we have shown that EBW generation can be triggered in VIS source by only modifying the permanent magnets position. Even if the ECR heating still remains the main heating mechanism, the energy content is strongly influenced by the generation of EBWs at UHR. Although VIS is typically operated with hydrogen, we hereby present operations with helium [88]. As it is shown in figure 5.7.1, the cross section for first helium ionization is relatively high compared to hydrogen (it shows the maximum at $\sim 130eV$). This means that Helium ionization is favoured by an increase of the electron temperature of the plasma, i.e. increase with plasma energy content.

In a Helium plasma the processes with the largest cross section are:

$$\begin{cases} He + e^- & \rightarrow & He^+ + 2e^- \\ He^+ + e^- & \rightarrow & He^{2+} + 2e^- \end{cases} \tag{5.7.1}$$

The relative ratios of various neutral and ion species in the discharge chamber are determined by the dynamical balance between their generation and loss rates. The number of reaction N occurring in 1 m^3 per second in the plasma chamber depends on the electron density n_e, on the ion density and on the reaction rate coefficient Q:

$$N(He^+) = n_e n_{He} Q\left(He \rightarrow He^+\right) \tag{5.7.2}$$

$$N(He^{2+}) = n_e n_{He^+} Q\left(He^+ \rightarrow He^{2+}\right) \tag{5.7.3}$$

The reaction rate coefficient depends only on the temperature of electron distribution function. In facts it is obtained by integrating the product between the cross section σ (which depends on the reaction type) and the velocity distribution [84]:

$$Q\left(He \rightarrow He^+\right) = \int_0^\infty \sigma\left(He \rightarrow He^+\right) f(v) v dv \tag{5.7.4}$$

$$Q\left(He^+ \rightarrow He^{2+}\right) = \int_0^\infty \sigma\left(He^+ \rightarrow He^{2+}\right) f(v) v dv \tag{5.7.5}$$

The threshold energy for first ionization of helium is 24.6 eV, while the threshold for the second ionization is 54.5 eV. MDIS are characterized by electron temperatures of 20-30 eV, value too low to have the second ionization of the helium. During the entire duration of the tests the value of the extraction potential has been fixed at 60 kV, while the potential of the negative biased electrode has been fixed at 2.2 kV. The measurements have been carried out by using an extraction aperture of 10 mm. The focusing solenoid at the beginning of the LEBT has been designed for focusing H^+ or H^{2+} beams and it is able to focus only beams having a ratio between ion mass and charge $M_i/Q < 3$. This means that it was not possible to correctly focus the He+ beam ($M_i/Q = 4$) in the beam stop at the end of the LEBT and a large part of the beam was lost along the walls of the LEBT. The measure of the extracted current has been carried out by measuring the current delivered by the power supply of the extracting electrode. After the bending magnet in the LEBT, the He^{2+} beam ($M_i/Q = 2$) may be measured if produced (but no significant amounts were detected during the experiment). Three parameters of the source have been modified during the measurements: the position of the permanent magnets, the neutrals pressure and the RF power. The magnets system was moved by steps of 2 mm, from 0 to 6 mm, according to the sketch in figure 5.7.2. For each position the magnetic field profiles have been calculated by using the TOSCA code [92].

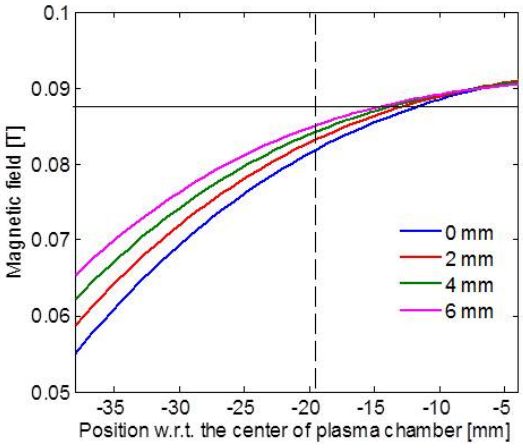

Figure 5.7.2: The emittance is slower when injection occurs off-resonance (position A). When injections take place under-resonance, emittance increases (position D).

For all the studied magnet position, as shown in figure 5.7.2, the injection takes place for $B < B_{ECR}$, i.e. the necessary condition to generate EBWs in plasmas is progressively fulfilled better and better.

In figure 5.7.3 we show the He^+ current measured as a function of the microwave power when the permanent magnets were at home position (0 mm) and at the different operative pressures. The better performance are obtained for the pressure values of $1 \cdot 10^{-5}$ mbar and $1.5 \cdot 10^{-5} mbar$. At higher pressure, the extracted current saturates at 700-800 W and decreases for microwave power greater than 1000 W. The dependence on microwave power and pressure is quite similar for all the positions of the permanent magnets: the best performance are ever obtained at the pressure of $1.5 \cdot 10^{-5}$ mbar, but the He^+ currents measured in each experimental point are lower with respect to the one obtained at the home position. In order to verify the influence of magnetic field on extracted current we compared the best performances obtained at the different position of the magnets, when fixing the neutrals pressure at $1.5 \cdot 10^{-5}$ mbar. The results are shown in figure 5.7.4.

The He^+ current increases with the position of the magnets. The current increases from the 39.3 mA measured at 1300 W for a shift of 6 mm to the value of 53 mA when the shift was 0 mm. The differences can be explained by taking into account the ionization rate of Helium. For the mono-charged He^+, relation (5.7.2) becomes:

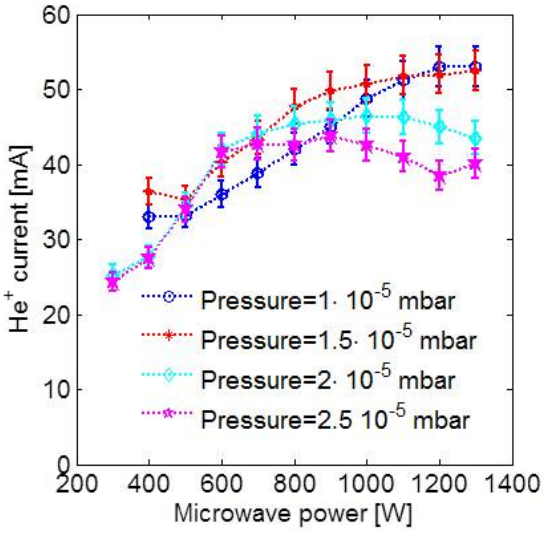

Figure 5.7.3: Comparison of He^+ current for different pressure at home position.

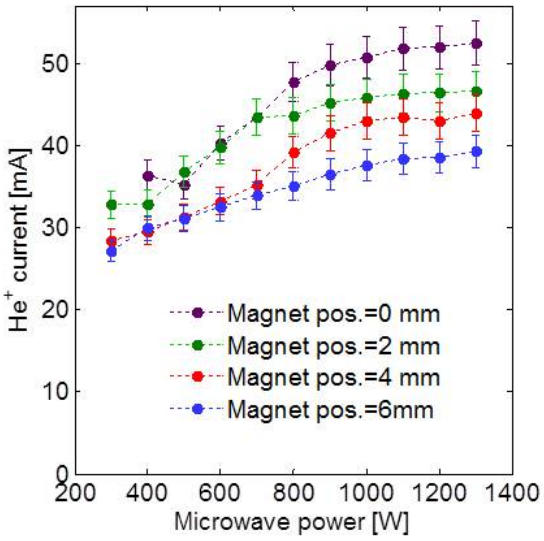

Figure 5.7.4: Comparison of He^+ current at the pressure of $1.5 \cdot 10^{-5}$ mbar for different position of the magnetic field.

$$N(He^+) = n_e^2 Q\left(He \rightarrow He^+\right) \tag{5.7.6}$$

The ionization rate increases when either the electron density or the reaction rate coefficient increase. However, similar measurements carried out with hydrogen gas suggest to neglect an increase of He^+ current due to an increase of electron density (or at least the electron density is not the main cause). In reference [92], measurements carried out with the same experimental set-up have shown that the highest proton current was obtained when permanent magnets were shifted of 4 mm. If the shifting of the magnets would affect the electron density, one should have the same dependence on the magnets position for both Helium and protons. On the contrary, the shifting of the permanent magnets affects reaction rate coefficient $Q(He \rightarrow He^+)$. As Q is basically a function of the electron temperature, $Q(He \rightarrow He^+)$ increases when the electron temperature is increased. The increase of the electron temperature is consistent with the generation of EBW for the smallest shifts of the magnets. In a few words, plasma energy content is positively affected by even a low efficiency EBW generation. These studies confirm the results obtained in section 5.6. Plasma generation mechanism is critically dependent on the applied magnetic field, much more than on the RF power or the background pressure. In the future it will be very interesting to repeat these experiment in devices where magnetic field is more easily tunable. It is not excluded, at the moment, the possibility to further enhance the electron temperature in order to provide multiply charged ions. The forthcoming "flexible plasma trap", to be installed at INFN-LNS in the next six months, will be the proper set-up to investigate such physical mechanisms.

Chapter 6

Conclusions and perspectives

The experiments conducted at the LNS has been based on the investigation of the innner-plasma modal conversion (from an EM to an ES wave) taking to overdense plasma formation. By an operative point of view, the research has been based on the detecting of peculiar signatures of the ES waves formation and following absorption: the overcoming density cut-off, the observation of non-linear heating, highlighted by the sudden appearance of X-ray emission above certain thresholds of RF power and finally, the broadening of electromagnetic spectrum, sign of interaction between the electromagnetic wave and the plasma waves. The three signatures have been simultaneously revealed for the first time in a compact device, the Plasma Reactor, in two different magnetic configurations. In magnetic beach configuration, working at 3.76 GHz, a density of $\sim 3.5 \cdot 10^{11} cm^{-3}$ was achieved close to cyclotron harmonics, a value two times larger than cutoff density. Double temperature electron population have been revealed correspondingly to the first harmonics. Flat-B configuration has been studied by using different frequencies, 2.45 and 3.75 GHz, and in both cases overdense plasmas have been generated. In terms of absolute density, the maximum value has been obtained at 2.45 GHz and 100 W RF power ($\sim 1.5 \cdot 10^{12} cm^{-3}$), while at 3.75 GHz was $\sim 8 \cdot 10^{17} m^{-3}$. The average value of the density in the two cases was $3.8 \cdot 10^{17} cm^{-3}$, at 2.45 GHz, and $5.1 \cdot 10^{17} cm^{-3}$ at 3.75 GHz (measured along the axis of penetration of electrostatic probe, while nothing can be said at the moment on the radial profile of the density). The experimental data suggest therefore the use of operating frequencies slightly higher than the standard 2.45 GHz. It should also be stressed that these density values were obtained despite the large size of the plasma chamber of our reactor, for which the volume is five times larger, for example, than

that of the source VIS: 4350 cm^3 against 864 cm^3. VIS requires a lower pressure, a minimum power of 400 W in order to support the plasma, while for the Plasma Reactor 20 W are enough to obtain a dense plasma but below the cut-off, and only 70-80 W to substantially exceed the critical density. These data show that the new heating method enables to reach very high densities by using very low nominal power without a complication of the technological apparatus. The data collected by means of X spectroscopy help to understand the non-linearity extent triggered by the RF power and able to convert the incident E.M wave in a plasma wave. Beyond the threshold microwave power, spectral temperature up to 4 keV has been obtained at 3.75GHz. This value need to be compared with the maximum energy obtainable by an electron from ECR heating, $\sim$ 200 eV. This further confirm that the heating mechanism is not the ECR. In this conditions plasma reactor has been demonstrated to be a very intense X-rays source. An X-ray radiation intensity up to 10^6 counts/sΩ over a detector intercepting just a factor 10^{-6} of the entire solid angle has been obtained with an hydrogen gas at the pressure of $4.5 \cdot 10^{-4}$ $mbar$. The measurements on the VIS source have definitively demonstrated that X ray radiation is emitted only when a under-resonance region in the source exists. When the magnetic field goes under-resonance, X-rays appear and the plasma energy content increases. This has been further demonstrated by measurements on a helium plasma. Larger values of helium current have been obtained when under-resonance region exist in plasma chamber, correspondingly with high energy X rays production. Along with the mentioned evidences, we also observed other phenomena (all of them correlated to the occurred conversion) like a plasma vortex formation: a double picked maxwellian distribution in resonance regions, together with a variation in the axial magnetic field, explainable only by means of the generation of an internal azimuthal current, have been contemporaneously detected with the other signs of wave-conversion. This drift motion accords totally with theoretical Golovanivsky predictions. The vortex structure has been detailed analyzed either in the optical and in the X domain, by means of a CCD and a pin-hole camera. The vortex corresponds to a well-know structure in the visible usually named "plasma hole". This structure exists also in X-ray domain. The structure can be explained taking into account an E×B drift, due to the contemporary presence of the magnetostatic field and of strong electric field (estimated in $1.5 \cdot 10^7$ V/m), the latter due to the propagation of plasma waves made by compression and rarefaction of electron density (and named Electron Bernstein Waves). Further experiment are therefore needed to investigate wheather the plasma ion

component participate to a collective plasma motion. From an interpretative point of view, the study objected of this thesis is not totally exhaustive and further investigations will be required in future to understand all the details of the conversion mechanism. According to literature data, the excitation of electrostatic waves should be optimized when the incident E.M wave is introduced inside the plasma in perpendicular direction with respect the force lines of the applied magnetic field. This should facilitate the generation of X wave which can be then converted at UHR resonance. On the contrary, our guiding system injects the electromagnetic wave parallel to the magnetostatic field. In our case the X wave generation is ensured by the plasma chamber properties, acting as a resonator for E.M waves. The establishment of stationary E.M waves, therefore, provides for the generation of non parallel wave vectors with respect to the magnetic field, and therefore allows the occurrence of UHR. The other advantage is ensured by the magnetic field that, in proximity of the two flanges of the cylindrical chamber, has a profile very steep and able to drop well below the corresponding value of ECR. The obtained results are therefore quite encouraging: a plasma overdense was supported at moderate values of RF power. The plasma energy content of the plasma (which can be roughly estimated as the product density for temperature, $N_e t_e$) increases considerably above the conversion threshold, and gradually increases with the RF power and especially with the operating frequency. The high electron temperatures obtained (several keV) suggests that such plasmas may allow the generation of multi-charged ions despite the very simple magnetic structure. In terms of future perspectives, this thesis has identified the main operating parameters on which the following studies on the new reactor (FPT - Flexible Plasma Trap) currently being assembled in the Laboratori Nazionali dek Sud (LNS), will be based. This is a very flexible magnetic trap (the layout and the magnetic system can be seen in Figure 6.0.1) and it can work up to 8-10 GHz , with a maximum magnetic field of 0.5 T.

The new reactor is also equipped with a radial waveguide which allow the launch of a direct X wave in the central region of the plasma.
We expect that the plasma density can grow further by identifying magnetic field profiles even more effective in enabling the modal conversion. The magnetic system consists, in fact, of three water-cooled copper solenoids allowing the tuning of the magnetic profile. The work done on the Plasma Reactor can still be seen as a phase of fundamental study on a new promising phenomenon, especially in view of the future challenges involving LNS, as the different international research projects in which high performance

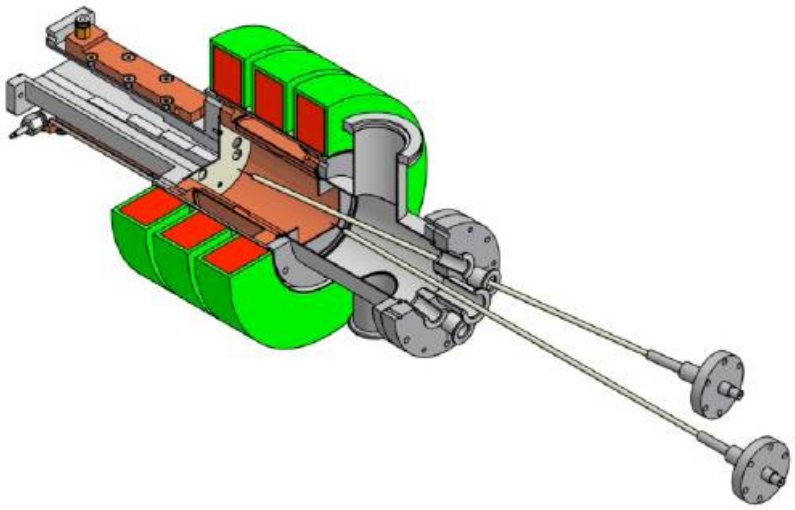

Figure 6.0.1: The new flexible plasma trap at INFN-LNS.

ion sources are required. For example, within of the European Spallation Source (ESS) project, for which the LNS leads the Work Package 6 (building of the source and of the "room temperature" LINAC), is being drafting a proposal in the "Technical Design Report", which involves the construction of a proton source of 80-100 mA based on the operating philosophy of VIS, but stressing, however, as the chosen magnetic system (characterized by a remarkable flexibility) can allow, in perspective, modal conversion mechanisms and then enable to obtain a considerable increase in electron density and extracted current. Other projects in the near future could take advantage of ion sources based on electrostatic heating, which in the medium term could accompanied, or even replace, the classical mechanism of plasma heating based on the direct absorption of electromagnetic waves at the Electron Cyclotron Resonance.

Bibliography

[1] F. F. Chen. Introduction to the Plasma Physics and Controlled Fusion: Plasma Physics. U.K.:London Press, London, 1986. Addison-Wesley, 1994.

[2] R. Geller. *Electron Cyclotron Resonance Ion Sources and ECR Plasmas.* PA: Inst. Phys., Philadelphia, 1996.

[3] S. Barbarino, *Appunti di campi elettromagnetici.*

[4] B. Wolf. *Handbook of Ion sources.* FL: CRC Press, Boca Raton, 1995.

[5] J. Brehm, W. Mullin *Introduction to the structure of matter.* J. Wiley and Sons (1989).

[6] A. Muller et al. Nucl. inst. meth., 140, 181 (1977)

[7] F. Di Bartolo, S. Gammino, D. Mascali, L. Celona, G. Castro, R. Miracoli, L. Neri, R. Di Giugno, C. Caliri, G. Torrisi, *Characterization of a H_2^+ source for the injector cyclotron of the Daeδalus project*, Messina, Phd day

[8] S. Bliman, R. Geller, W. Hess, B. Jaquot, and C. Jaquot. Int. Conf. on Heavy Ion Sources; IEEE Trans. Nucl. Sci., (1972). NS-23, 2, 200.

[9] M. S. Ioffe. *Mirror Traps.* Plasma Physics, (1965).

[10] D. Mascali. *Studio teorico e sperimentale dei processi di riscaldamento elettronico per la produzione di ioni ad alto stato di carica in sorgenti ioniche del tipo ECR.* Degree Thesis in Physics, Universitá degli studi di Catania, Italy. (2005)

[11] G.Shirkov, V.Alexandrov, and V. Preisendorf et. al. Physical and numerical basement of ECR plasma simulation with particle-in-cell model. Riken Accelerator Research Facility, August 2000.

[12] M.A. Lieberman, A.J. Lichtenberg *Principles of plasma discharges and material processing* J. Wiley and Sons, 1994

[13] A. Simon, *Ampipolar diffusion in a magnetic field*, Phys. Rev. 98, 317 (1955).

[14] A. G. Drentjea, U. Wolters, A. Nadzeyka, D. Meyer, and K. Wiesemann, *Simon short circuit effect in ECRIS*, Rev. Sci. Intrum. VOL. 73, N. 2 (2002)

[15] S. Gammino, J. Sijbring, and A. G. Drentje, Rev. Sci. Instrum. 63, 2872 (1992).

[16] G. Castro, R. Miracoli, D. Mascali, L. Celona, D. Lanaia, L. Allegra, F. Chines, S. Gammino and G. Ciavola, *enhancement of the ion current from the VIS source by menas of an alumina tube* LNS internal reporto (2012)

[17] Malferrari L, Odorici F, Veronese GP, Rizzoli R, Mascali D, Celona L, Gammino S, Castro G, Miracoli R, Serafino T. *Modification of anisotropic plasma diffusion via auxiliary electrons emitted by a carbon nanotubes-based electron gun in an electron cyclotron resonance ion source*. Rev Sci Instrum. 2012 Feb 83(2) 02A343.

[18] A. Piel, G. Oelerich and H. Thiemann*Principle of the resonant cones method, laboratory verification and application for the diagnostic of ionospheric plasma*, Adv. Space Res. vol. 8 n.8 (1988)

[19] G. Lisitano, M. Fontanesi, and E. Sindoni *Nonresonant absorption of electromagnetic waves in a high density plasma* Appl. Phys. Lett. 16, 122 (1970)

[20] A.W. Trivelpiece and R.W. Gould,Space charge waves in cylindrical plasma columns, J. Appl. Phys. 30, 1784 (1959)

[21] F. Jeager, A. J. Lichtenberg, and M. A. Lieberman. *Theory of electron cyclotron resonance heating I. Short time and adiabatic effects.* Plasma Phys., v. 14, n. 12, 1073-1100. (1972)

[22] F. Jeager, A. J. Lichtenberg, and M. A. Lieberman. Theory of electron cyclotron resonance heating II. Long time and stochastic effects. Plasma Phys., v. 15, n. 2, pp. 125-150 (1973)

[23] *Spectroscopic determination of the cold electron population in very low pressure ECR discharges in N^2/He mixtures.* Plasma Sources Sci. Technol. 14 (2005) 109 – 128

[24] C. Lyneis, P. Ferracin, S. Caspi, A. Hodgkinson, and G. L. Sabbi *Concept for a fourth generation electron cyclotron resonance ion source* Rev. Sci. Instrum. 83, 02A301 (2012)

[25] K. S. Golovanivsky. ECRIS plasmas: Stochasting heating or Langmuir caviton collapses? in Proc. 11th ECRIS Workshop, Groningen, The Netherlands, 1993. p. 78.

[26] H. P. Laqua. *Electron Bernstein wave heating and diagnostic.* Topical Review of Plasma Phys. Control. Fus., 2007. vol. 49, R1-42.

[27] K. T. McDonald *An Electrostatic Wave* arXiv:physics/0312025

[28] Ira B.Bernstein. Bernstein modes. Phys. Rev. Lett., (1958). 109, 10.

[29] T.A. Stix *Waves in plasmas* springer-verlag new York (1992).

[30] Crawford F W 1965 J. Appl. Phys. 36 2930

[31] F. Volpe. *Electron Bernstein emission diagnostic of electron temperature profile at $W7 - AS$ Stellarator.* PhD thesis, 2003. Ernst Moritz Amdt University, Greifswald.

[32] d. Mascali *A new approach to the study of the ECR heating and particle dynamics in the plasma of Electron Cyclotron Ion Sources* PhD thesis, 2008 UniversitÃ degli studi di Catania.

[33] Y. Y. Podoba, H. P. Laqua, G. B. Warr, M.Schubert, M. Otte, S. Marsen, F. Wagner, Physical Review Letters 98 (2007) 255003.

[34] J. Preinhaelter, et al., Plasma Physics and Controlled Fusion 51(2009).

[35] Hansen F. R. et al. 1985 Plasma Phys.Control. Fusion 27 1077

[36] A.K. Rams, A. Bers, C. N Lashmore-davies *Electron Bernstein waves in spherical torii* Proc. of 29th EPS conference on plasma physics and contr. fus. ECA vol. 26b $p - 5.075$ (2002)

[37] McDermott F S et al. 1982 Phys. Fluids 25 1488

[38] Wilhelm R., Erckmann V., Janzen G., Kasparek W., Mueller G. and Rauchle E., Schueller P. G., Schwoerer K. and Thumm M. Plasma Phys. Control Fusion 261433 – 44 (1984)

[39] Budden K. *The Propagation of Radio Waves* (Cambridge: Cambridge University Press) 596 – 602(1985)

[40] Jones B et al. 2003 Phys. Rev. Lett 90 165001

[41] Chattopadhyay P K, Anderson J K, Biewer TM, Craig D, Forest C B, Harvey RWand Smirnov A P 2002 Phys. Plasma 9 752-5

[42] Taylor G. et al. 2003 Phys. Plasmas 10 1395-400

[43] Preinhaelter J. and Kopecky V. 1973 J. Plasma Phys. 10 1

[44] I. G. Brown. *The Physics and Technology of Ion Sources*. NewYork: Wiley, 2004.

[45] M. P. Stockli. *Design of the extraction system of the superconducting ECR ion source VENUS*. Proceedings of the 2001 Particle Accelerator Conference, Chicago, June 2001.

[46] D. Mascali, S. Gammino, L. Celona, G. Ciavola *Towards a better comprehension of plasma formation and heating in high performance ECRIS* , Rev. Sci. Instrum. 83, 02A336 (2012)

[47] J. Kim, D.C. Davis, Appl. Phys. lett. 30 n.3, 130, (1977)

[48] http://www.lns.infn.it

[49] L. Celona, S. Gammino, G. Ciavola, F. Maimone, D. Mascali, *Microwave to plasma coupling in ECR and Microwave ion sources*, Rev. Sci. Instrum. 81, 02A333 (2010).

[50] S. Gammino and G. Ciavola. *The role of microwave frequency on the high charge states build-up in the ECR ion sources*. Plasma Source Sci. Technol, May 1996. 5, 19-27.

[51] G. Ciavola and S. Gammino. *A superconducting electron cyclotron resonance source for the L.N.S.* Rev. Sci. Instr. 63, 2881 (1992)

[52] A. G. Drentje et al., RSI, 73 N.2 (2002) 516

[53] T. A. Antaya and S. Gammino. *The superconducting electron cyclotron resonance 6.4 GHz high-B mode and frequency scaling in electron cyclotron resonance ion sources.* Rev. Sci. Instrum., May. 1994. vol. 65, no. 5, p. 1723.

[54] R.Geller et al. Proc. 1^{st} int. conf. Ion sources, Saclay, 537, (1969)

[55] D. Mascali, L. Neri, S. Gammino, L. Celona, G. Ciavola, N. Gambino, R. Miracoli, and S. Chikin *Plasma ion dynamics and beam formation in electron cyclotron resonance ion sources*, rev. sci, instrum. 81, 02A334 (2010)

[56] T. Taylor and J.S.C. Wills, *A high-current low-emittance dc ECR proton source* Nucl. Instrum. and Meth. A309 37-42 (1991)

[57] S. Gammino et al. Proceedings of the 14th Workshop on ECRIS, 1999. CERN, Geneva, p. 139.

[58] Ciavola G.; Gammino S.; Raia G.; Sura J. , **MIDAS, a high efficiency microwave discharge ion source for the EXCYT facility**, Rev. Sci. Instr. , 65, 4, (1994)

[59] L.Celona, S.Gammino, G. Ciavola, F. Chines, S. Marletta, and E. Messina. Ionization efficiency measurements with the Microwave Discharge Ion Source MIDAS. pages 1601-1603. Proceedings of EPAC 2000, Vienna, Austria, 2000.

[60] N. Sakudo. *Microwave ion sources for industrial applications (invited). Review of Scientific Instruments*, 71:1016-1022, (2000)

[61] G. Lisitano, R. Ellis, W. M. Hooke, and T. H. Stix. Rev. Sci. Instrum., 1968. vol.39, 295.

[62] G. Lisitano, M. Fontanesi, and E. S. Sindomi. Appl. Phys. Lett., 1970. 16 122.

[63] F. Carminati, R. Klapisch, J.P. Revol, C. Roche, J.A. Rubio, and C. Rubbia. An energy amplifier for cleaner and inexhaustible nuclear energy production driven by a particle beam accelerator. CERN-AT-93-47-ET, page 70, 1993.

[64] F. Maimone, S. Gammino, L. Celona, G. Ciavola, D. Mascali, N. Gambino, R. Miracoli, F. Chines, G. Gallo, S. Passarello, *Commissioning of*

the New Versatile Ion Source (VIS) for High Power Proton Accelerators Proc. of 23^{rd} Symposium on Plasma Physics and Technology,16-19 June 2008, Prague, Czech Republic

[65] N. Chauvin *Space charge effects* proc. of the first Cern Accelerator School on ion sources, 29 May - 8 June, 2012 Senec slovakia

[66] Gobin R., Beauvais P., Ferdinand R., Leroy P., Celona L., Ciavola G. and Gammino S. *Improvement of beam emittance of the CEA high intensity proton source SILHI* Review of ScientiVc Instruments, 70(6):2652-2654. (1999)

[67] R. Z. Sagdeev and V D. Shapiro, Pis'ma Zh. Eksp. Teor. Fiz. 17, 389 (1973) [JETP Lett. 17, 279 (1973)].

[68] K.S.Golovanivsky el al. *Proposed physical model for very hot electron shell structures in electron cyclotron resonance-driven plasmas* Physical Review E, vol.52, n.3 sept. 1995 .

[69] Rosalba Miracoli *characterization of microwave discharge ion source for high proton beam production in CW and pulsed mode* PhD. Thesis 2010 UniversitÃ degli studi di Catania.

[70] F. Maimone et al. Proceedings of 23rd Symposium on Plasma Physics and Technology, 16-19 June, Prague, Czech Republic, (2008).

[71] L. Celona, G. Ciavola, S. Gammino, R. Gobin, and R. Ferdinand. *TRIPS: The high intensity proton source for the TRASCO project.* Review of Scientific Instruments, $71 : 771 - 773$, (2000).

[72] S. Gammino, L. Celona, G. Ciavola, N. Gambino, F. Maimone, D. Mascali, R. Miracoli, L.Torrisi, F. Samperi *A plasma reactor for enviromental applications* LNS internal report (2008)

[73] B M Annaratone, M W Allen and J E Allen *Ion currents to cylindrical Langmuir probes in RF plasmas* J. Phys. D: Appl. Phys. 25 417 (1992)

[74] R. Godard and J. G. Lafambroise *total current to cylindrical collectors in collisionless plasma flow*

[75] M. Lampe, J. Plasma Phys. 65, 171 (2001).

[76] Francis F Chen *Langmuir probes in RF plasma: surprising validity of OML theory* Plasma Sources Sci. Technol. 18 (2009) 035012

[77] H. M. Mott-Smith and I. Langmuir, *THE THEORY OF COLLECTORS IN GASEOUS DISCHARGES* Phys. Rev. 28, 727 (1926)

J. E. Allen *Probe theory - the orbital motion approach* Physica Scripta. Vol. 45, 497-503, 1992.

[78] M. J. Druyvesteyn, Z. Phys. 64, 781 (1930).

[79] I. H. Hutchinson, *Principles of Plasma Diagnostics* Cambridge University Press, Cambridge, (1987).

[80] Andor iKon-M XRay Technology User Guide.

[81] A. Gumberidze, M. Trassinelli, N. Adrouche, C. I. Szabo, P. Indelicato, F. Haranger, J.-M. Isac, E. Lamour, E.-O. Le Bigot, J. MÃ©rot, C. Prigent, J.-P. Rozet, and D. Vernhet, *Electronic temperatures, densities, and plasma x-ray emission of a 14.5 GHz electron-cyclotron resonance ion source* REVIEW OF SCIENTIFIC INSTRUMENTS 81, 033303 (2010)

[82] G. Castro, R. Miracoli, D. Mascali, S. Gammino, L. Celona, D. Lanaia, L. Allegra and G. Ciavola *enhancement of the ion current from the VIS source by means of an alumina tube* LNS internal report (2012)

[83] H. Zhang *Ion Sources* Tokyo Springer (1999)

[84] K. Y. Vipin and D Bora. Journal of physics Vol. 63, No. 3 - September 2004

[85] K. Nagaoka, A. Okamoto, S. Yoshimura M. Kono and M. Y. Tanaka *Spontaneous Formation of a Plasma Hole in a Rotating Magnetized Plasma: A Giant Burgers Vortex in a Compressible Fluid* P.R.L. VOL. 89, N.7 (2002)

[86] S. Yoshimura, A. Okamoto and M.Y. Tanaka, *Measurement of Ion Flow Velocity Field Associated with Plasma Hole Using Laser Induced Fluorescence Spectroscopy* J. Plasma Fusion Res. SERIES, Vol. 8 (2009)

[87] G. Castro, D. Mascali, L. Celona, S. Gammino, M. Mazzaglia, R. Miracoli C. Caliri, R. F. Di Bartolo, Di Giugno, L. Allegra, F. Chines and G. Ciavola, *Production of high intensity He+ beams from the VIS source* LNS internal report (2012)

[88] Igor Bray et al. J. Phys. B: At. Mol. Opt. Phys. 44 (2011) 061001 (3pp)

[89] David Mascali, F.P. Romano, S. Gammino, G. Castro, C. Caliri, L. Celona, R. Di Giugno *Preliminary studies on the x-ray emission from an innovative plasma-trap based on the Bernstein waves heating mechanism* proc. of EXRS, Vienna (2012)

[90] Claudia Caliri, *Caratterizzazione di una pin-hole camera ed imaging di raggi-X emessi da un plasma generato da microonde a 3.75 GHz* Degree Thesis in Physics, Universitá degli studi di Catania, Italy. (2005)

[91] R. Miracoli et al., Rev.Sci.Intrum. 83, 02A305 (2012)